SAPIENZA
UNIVERSITÀ DI ROMA

# Time of flight measurements at the FOOT experiment: detector characterization and preliminary results


Facoltà di Scienze Matematiche, Fisiche e Naturali

Corso di Laurea Magistrale in Fisica

Candidate

Gaia Franciosini

ID number 1647212

Thesis Advisor

Prof. Riccardo Faccini

Co-Advisor

Prof. Alessio Sarti



Academic Year 2018/2019

**Time of flight measurements at the FOOT experiment: detector characterization and preliminary results**
Master thesis. Sapienza – University of Rome



This thesis has been typeset by LaTeX and the Sapthesis class.

Version: October 11, 2019

Author's email: franciosini.gaia@email.com

*"Nothing in life is to be feared,*
*it is only to be understood.*
*Now is the time to understand more,*
*so that we may fear less."*
*Marie Curie*

# Acknowledgments

*Prima di lasciar spazio alla trattazione del mio lavoro di tesi, vorrei ringraziare chi ha sostenuto il mio percorso di ricerca. In primo luogo è quindi necessario ringraziare il mio relatore, il professore Riccardo Faccini che con le sue lezioni mi ha avvicinato al campo della fisica medica. Grazie a lui ho scelto la tesi che qui vi propongo e che mi ha dato la possibilità di arrivare a via Antonio Scarpa 16, esattamente nei laboratori della palazzina E. Senza il sostegno e l'aiuto delle persone che lì ho incontrato questo lavoro di tesi non sarebbe così completo e, spero, valido. Ho lasciato, inizialmente a malincuore, l'edificio Marconi di Fisica che mi ha accolto questi cinque anni, ho attraversato l'assolatissima via Regina Elena e mi sono imbattuta nell'ufficio del mio controrelatore, il professore Alessio Sarti che non posso non ringraziare. I suoi insegnamenti sono stati per me fonte di grande crescita e un continuo stimolo, per migliorare e progredire nella strada che ho deciso di intraprendere. Ringrazio Vincenzo e Michela, che in quella tratta Roma-Milano sono stati di grande conforto, per il loro sostegno e i loro preziosi consigli di cui, con tutta sincerità, avevo grande bisogno. Devo ringraziare ovviamente anche Giacomo per le sue spiegazioni, sempre chiarissime, per il suo immancabile aiuto e per la sua infinita pazienza. Nei laboratori però gravitano molte più persone, devo ringraziare quindi anche Riccardo, Micol, Marta e Eliana che mi hanno sempre strappato un sorriso ma che soprattutto mi hanno sopportato e supportato ogni giorno. Chi mi conosce sa che l'ansia mi caratterizza: tutti coloro che ho incontrato lì sono stati in grado di rasserenarmi e contenere questa mia predisposizione, a volte esagerata. Anche se ho lasciato l'edificio di Fisica non posso dire lo stesso per le persone con cui ho condiviso la maggior parte delle lezioni ed esami, in particolare Renata, Angelica e Luca. Le cose per cui li dovrei ringraziare sono troppe, senza di loro questi anni di studio non sarebbero stati così divertenti ed emozionanti come invece sono stati. Il loro appoggio è stato di fondamentale importanza, e per questo gli sono molto grata. Difficilmente mi potrei scordare i laboratori, i pranzi da Livio e le pause caffè che abbiamo condiviso e che sono stati scenario di divertenti e spensierati momenti. Non posso non ringraziare anche chi mi ha sostenuto al di fuori delle mura del dipartimento di Fisica tra cui soprattutto Giorgia, sicuramente il mio punto di riferimento, che mi ha sempre spronato a fare di più e appoggiato in ogni mia scelta. I suoi consigli, di vitale importanza, sono stati per me fonte di grande incoraggiamento. Ringrazio poi Costanza che mi sopporta da ormai 10 anni e che ogni giorno condivide con me gioie, sacrifici e successi, senza voltarmi mai le spalle. Questo mio piccolo e primo traguardo lo devo però soprattutto alla mia famiglia, ai miei genitori Silvia e Luigi, a mia sorella Sofia e a mio fratello Giorgio. Senza il loro sostegno ed incoraggiamento non sarei dove sono ora, sono stati il mio principale supporto e, seppur costretti, la mia valvola di sfogo. A loro dedico tutto il mio lavoro. Ringrazio le mie nonne, Lucia e Gianna, per tutti gli "in bocca al lupo", sistematicamente ricevuti la sera prima di ogni esame, e per aver sempre creduto in me. Per ultimo, ma sicuramente non per ordine di importanza, ringrazio Francesco che ha festeggiato ogni mio successo sostenendomi in ogni esame, dal primo all'ultimo, e confortandomi quando ne avevo bisogno. L'affetto e il sostegno che mi ha dimostrato rendono questo traguardo ancora più unico.*

# Contents

# Introduction

Cancer diseases are one of the major widespread health problems. According to the last report of the World Health Organization (WHO), in 2018 there have been 18.1 million new cases diagnosed and 9.6 million cancer related deaths. Nowadays there are different techniques to treat neoplastic diseases as surgery, chemotheraphy, radiation therapy and, more recently, immunotherapy. Although surgery is the most widespread treatment approach for the cure of solid tumors, approximately 2/3 of all patients diagnosed with cancer receive curative or palliative radiation treatments. In the last decades the progress in technology has driven an exponential growth and diffusion of a tumor treatment technique alternative to the conventional radiotherapy. The advances to the acceleration techniques of heavy charged particles has sped up the diffusion of Particle Therapy (PT). PT exploits accelerated charged hadrons, such as protons and heavier ions for the treatment of both early and advanced solid tumors that are *radio-resistant* or located near vital or delicate organs. The PT strength lies in the unique physical and radiobiological properties of the particles used: the energy release and thus the induced cells apoptosis, is highly selective, targeting only cancer cells with little diffusion and preserving the surrounding healthy tissues. Another advantage derived from the use of charged particles is due to their enhanced relative biological effectiveness which results in a markedly increased cell killing efficiency for the same delivered dose. However, in order to minimize the impact of the safety factors currently implemented and fully exploit the PT potential, an improved knowledge of the dose deposition due to the incident particles (Z>1) and the target tissues fragmentation is eagerly needed. At the present time there is a lack of experimental nuclear reaction cross section measurements for fragments produced in the interaction with tissue nuclei (H, C, Ca, O and N) of 60-250 MeV protons and 100-350 MeV/u carbon ions, which are the typical energies adopted in PT treatments. These data are essential to improve the algorithms currently used in the Treatment Planning Systems (TPS) for proton and heavy ion therapy. The measurements of the protons nuclear reaction cross sections is of particular interest since it is know that the proton biological effectiveness assumed in the current TPS could be significantly over- or under-estimated as it does not account for the nuclear fragmentation processes.

The **FOOT** (FragmentatiOn Of Target) experiment, that is expected to begin the data taking in late 2020, has been designed and optimized for the measurement of the target and projectile fragmentation cross sections relevant for PT (at energy up to 400 MeV/u) and for radioprotection in space (at higher energies, up to few GeV/u). The FOOT experiment adopts an inverse kinematic approach to overcome

the difficulties related to the short fragments range ($\sim \mu$m) produced in case of target fragmentations: O, C, N, Ca ions with energies of interest for PT applications are accelerated and shot against fixed targets and the proton induced fragmentation of the target is obtained after applying a Lorentz transformation. The FOOT apparatus consists of a high precision tracking system in magnetic field, a time of flight measurement system and a calorimeter.
At low energies, i.e. in the PT energy range, a crucial role in minimizing the uncertainty on the isotope mass number determination is played by the Time Of Flight (TOF). The fragments production cross sections heavily rely on such measurement to properly identify the isotope and hence compute the fragment range.
In particular the fragments mass has a significant role since it influences their range. When incident proton beams undergo fragmentation, they produce hydrogen, carbon or helium isotopes which, for a given kinetic energy per nucleon, have different ranges and so they produce different biological damages. To properly account for the different fragments range and its impact on the radiation RBE it is essential to achieve a high accuracy on the isotopic identification and thus on the TOF, momentum and kinetic energy measurements.
In particular the measurement of the TOF, drives the resolution on $A$ and hence was the subject of several optimization studies concerning the technology to be adopted. Finally, in FOOT, the choice was to perform the measurement using two distinct detectors: the Start Counter (SC) placed upstream of the target, and the scintillator wall (TW) placed downstream. During my thesis project I took care of the detectors readout implementation, data taking operation and data analysis aiming to characterize their performance and ensure that the requirements set by the FOOT collaboration are met. The TOF measurement needs to be performed with an overall resolution of 100 ns or less. The SC detector needs hence to achieve a 70 ps resolution on the incoming ions (at all the different energies). The TW, in a similar way, needs to measure the fragments crossing time with resolution below 70 ps for all the different fragments at different energies. My thesis project is focused on the SC and TW operation and characterization. In particular, I contributed to develop the data acquisition algorithms and I implemented the software needed to decode and fit the acquired waveforms in order to compute the fragment TOF. I also concentrated my efforts to optimize the waveforms analysis to maximize the time resolution.

In chapter 1 the basics of radiation interaction with matter for the charged particles will be introduced, followed by a description of the relevant radiobiological parameters adopted in PT and the state of the art in hadrontherapy. Chapter 2 will show the strategy for measurements and the experimental setup adopted in the FOOT experiment. Chapter 3 will present the Monte Carlo (MC) FLUKA code adopted in the FOOT experiment to perform studies about the fragments produced. The general principles of operation and the details of the SC and the scintillator wall employed in the FOOT design are described in chapter 4. The results of the studies will be shown in chapter 5.

# Chapter 1

# Hadrontherapy

In the last decades, the progress in technology has lead to the establishment of an alternative technique with respect to conventional radiotherapy: the hadrontherapy. It consists on proton or heavy ion, such as carbon, beams used to irradiate the cancer cells in cases of radio-resistant tumors or tumors that are near vital or delicate organs. The hadrontherapy main advantage lies in proton and heavy ion physical and radiobiological properties: these particles can penetrate the tissues with little diffusion and deposit the maximum energy just before stopping, in the so-called Bragg Peak (BP) region. This provides a precise definition of the specific region to be irradiated thus allowing to preserve the healthy tissues.
The idea of using protons for cancer treatment was first proposed in 1946 by the physicist Robert Wilson (that later will become the founder and first director of the Fermi National Accelerator Laboratory). The first patients were treated in the 1950s. Initially, the clinical applications were limited to few parts of the body, as accelerator were not powerful enough to allow protons to penetrate deep in the tissues. In the late 1970s improvements in accelerator technology, coupled with advances in medical imaging and computing, made protontherapy a viable option for routine medical applications. However, it has only been since the beginning of the 1990s that proton facilities have been established in clinical settings, the first one being in Loma Linda, USA. Currently about 68 proton or heavy ion centers are in operation worldwide. Other 39 facilities are under construction.
In the following sections the proton and heavy ion physical and radiobiological properties will be presented compared to the ones of the X-rays to explain why adrontherapy is in some cases more effective than conventional radiotherapy.

In the next sections the physics relating to the particle interactions with matter will be introduced. In the central section of the chapter, the physical effects associated to the nuclear interaction will be discussed, and it will be presented the state of the art for the fragmentation effects in hadrontherapy. In the last section, the most relevant radiobiological parameters and effects will be presented, followed by an overview of the proton therapy biological effectiveness and the related open questions.

## 1.1 Physics for Hadrontherapy

The passage of charged particles through a material is mainly characterized by the energy loss, the angular deflection and the fragmentation nuclear interactions (described in details in sec.1.2). Some of these aspects and other physical principles of charged particles interaction with matter are discussed below.

### 1.1.1 Dose deposition

The dose deposited D in tissue is defined as the mean energy deposited by ionizing radiation in a mass element $dm$:

$$D = \frac{d\bar{\epsilon}}{dm} \tag{1.1}$$

where $d\bar{\epsilon}$ is the mean amount of energy absorbed by the elementary piece of matter. The dose unit is the Gray[1] (labeled Gy).
A comparison of depth-dose profiles for carbon ions, protons and $\gamma$ rays is shown in Fig.1.1 [1]. Compared to conventional radiotherapy, hadrontherapy presents two main advantages. Firstly, the heavy ion or proton physical characteristics, see Fig.1.1, are such as to release the dose with very high precision minimizing the damage to the surrounding healthy tissues. Only a small dose is released in the entrance channel (typically from 10% to 20% of the maximum) that is followed by a narrow region at the end of the path, the BP, where the maximum energy deposition is observed. The main drawback of the X-rays treatment is due to their ballistic: the maximum of the dose deposition is located at a small penetration depth, then the dose decreases slowly. In this case it is difficult to accurately target tumors deeply located in the body while preserving simultaneously the surrounding tissues.

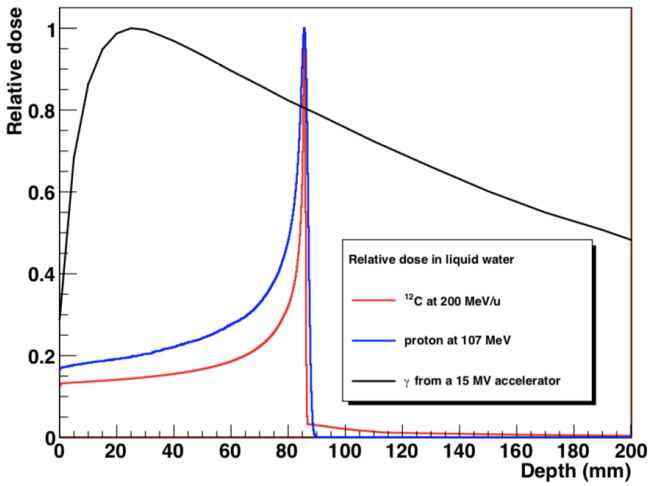


**Figure 1.1.** Evaluation of the relative dose with respect to the penetration depth in water for different particles.

As it will be seen later, the location of the BP only depends on the particle incident energy, allowing to sight accurately the tumor with a weak dose deposition

[1] One Gray is equal to an absorbed energy of one Joule in one kilogram of matter.

on the tissues located before and after the BP. Therefore, it is possible to adjust the BP location to the desired depth in tissues.
In the clinical practice, the width of the Bragg peak is too narrow to cover all the tumor volume. Thus a superimposition of different beams with different energies is necessary to obtain a broader irradiation profile. The result is an extended Bragg peak called Spread Out Bragg Peak (SOBP)[1] that can cover all the tumor volume (Fig.1.2)

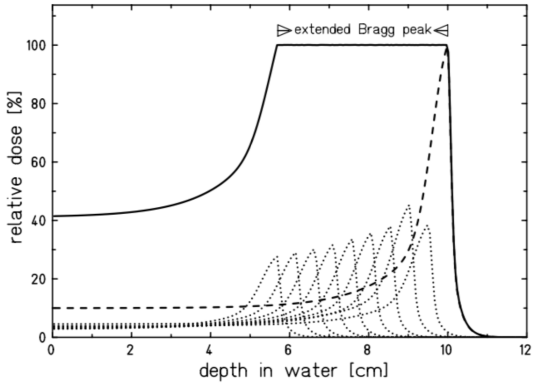


**Figure 1.2.** Spread Out Bragg Peak (SOBP) for protons.

The second hadrontherapy advantage, that here is briefly anticipated but it will be clarified in sec.1.3, lies in the biological effects induced by the charged particles: to kill the same amount of cells, lower doses are needed compared to the ones needed for X-rays.
To simplify the dose calculation a more operational dose definition is used:

$$D = \frac{N}{dS}\frac{\frac{dE}{dx}}{\rho} \tag{1.2}$$

where $\frac{N}{dS}$ is the beam fluence and $\frac{dE}{dx}$ is the particle *stopping power* in the matter with a $\rho$ density.

### 1.1.2 Stopping Power and Linear Energy Transfer (LET)

The *linear stopping power* S for charged particles in a given absorber is defined as the ratio of the differential energy loss for that particle within the material to the corresponding differential traversed thickness:

$$S = -\frac{dE}{dx} \tag{1.3}$$

When a beam at energy between 80 and 400 MeV crosses the tissue, the main physical process involved is the inelastic collision of nuclei on the electrons of atom present in the target. In that process, the projectile of kinetic energy $E_c$ looses an energy $\delta E$ equal to the sum of energy of the out coming electron $e_c$ and the ionization potential of that electron $I$. Most of the electrons are stopped near their emission point while some of them have sufficient energy to deposit their energy farther ($\delta$ rays). For this reason, the energy absorbed locally by the material is not

strictly equal to the stopping power. The Linear Energy Transfer (LET) which is the energy transfered by the beam to the material per unit length is defined as follows:

$$LET = \left(\frac{dE}{dx}\right) - \sum E_c(e_\delta) \tag{1.4}$$

where $\sum E_c(e_\delta)$ is the total kinetic energy of the $\delta$ electrons which have an energy above a given threshold.
However, in a first approximation the Stopping Power can be identified with the LET and with the absorbed energy in the elementary volume of thickness $dx$:

$$\frac{dE}{dx} \approx LET \approx \frac{E_{dep}}{dx} \tag{1.5}$$

### 1.1.3 The Bethe-Block formula

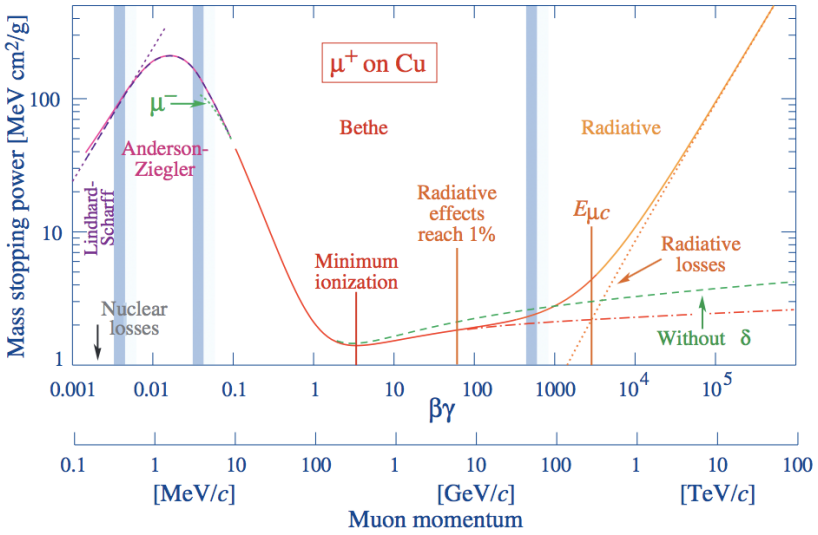


**Figure 1.3.** Stopping power distribution as a function of the energy. The dotted part on the right indicates the behavior of $-dE/dx$ for heavy charged particles, with or without density correction.

Radiotherapy of deep-seated tumors requires ion beam paths in tissues of up to 30 cm corresponding to a specific energies up to 220 MeV/u for protons and 430 MeV/u for carbon ions with particles velocity $\beta \sim 0.7$. At this velocity the Stopping Power is dominated by elastic collisions with the target electrons and can be well described by the Beta Block formula:

$$-\frac{dE}{dx} = 4\pi N_A r_e^2 m_e c^2 \rho \frac{Z}{A}\frac{z^2}{\beta^2}\left[\frac{1}{2}ln\left(\frac{2m_e c^2\beta^2\gamma^2 T_{max}}{I^2}\right) - \beta^2 - \frac{\delta}{2}\right] \tag{1.6}$$

with:

- $r_e$: classical electron radius;
- $m_e$: electron mass;

- $N_a$: Avogadro constant;
- $Z$: atomic number of absorbing material;
- $A$: atomic weight of absorbing material;
- $\rho$: density of absorbing material;
- $z$: charge of incident particle;
- $T_{max}$: maximum energy transfer in a single collision;
- $I$: mean excitation potential;
- $\delta$: density correction;
- $C$: shell correction;
- $\beta$: projectile velocity.

The equation 1.6 is valid for electrons and light ions with energies greater than 10 MeV/u, energy corresponding to the average velocity of the target electrons; below this threshold the process of electron capture becomes predominant, causing a change in the projectile's charge. To overcome this problem and therefore extend the range of validity of the equation, $Z_p$ is substituted by an effective charge $Z_{eff}$. This quantity takes into account the reduction of charge along the projectile path due to ionizations and recombinations, when the projectile velocity is comparable with the orbital velocity of the target electrons. $Z_{eff}$ can be described by the empirical formula (Berkas equation):

$$Z_{eff} = Z_p[1 - exp(-125\beta Z_p^{-2/3})] \tag{1.7}$$

The maximum energy-loss rate, corresponding to the Bragg peak, is reached at a projectile velocity of $v_p \simeq Z_p^{2/3} v_o$ where $v_o = e^2/\hbar$ is the Bohr velocity and the corresponding $\beta$ value is $e^2/\hbar c = 1/137$.

### 1.1.4 Range and angular straggling

The total path length of the particle trajectory in the absorber is given by:

$$R(E) = \int_0^E \left(\frac{dE'}{dx}\right)^{-1} dE' \tag{1.8}$$

which for heavy charged projectiles is nearly the same as the mean range $R$, i.e. the average traversed absorber thickness because heavy ions are very little scattered and travel almost on a straight line. Fig. 1.4 shows the range of different particle types with respect to their incident energy, obtained with the SRIM simulation[2]. For a given energy per nucleon, the range of a projectile is proportional to the ratio $A/Z^2$ where $A$ and $Z$ are the projectile mass and charge number respectively.

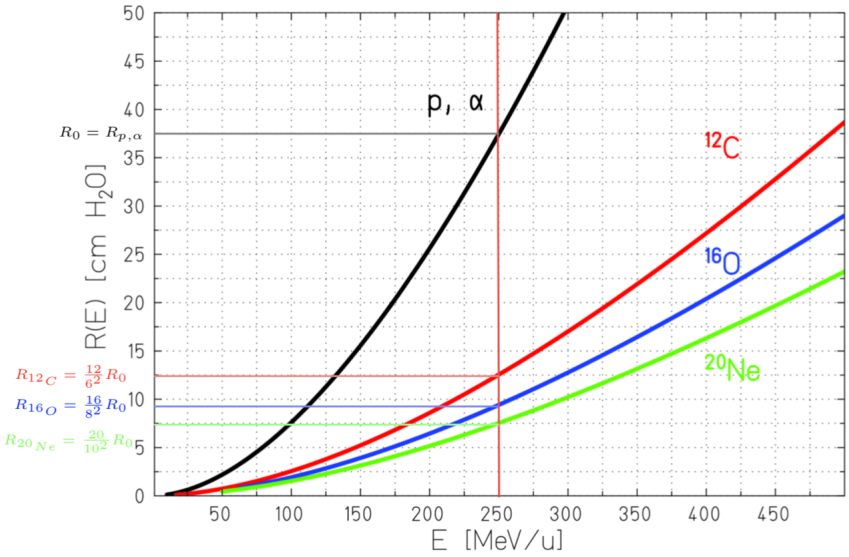


**Figure 1.4.** Mean range of different types of particles in liquid water.

According to the Bethe-Block formula (Eq.1.6), the energy loss of a single carbon ion plotted as a function of absorber depth would result in a very sharp peak near the stopping point. However, the statistical fluctuations of the energy loss in the large number of collisions of the slowing-down process result in a broadening of the BP for an ion beam. These fluctuations of charged particles crossing a thin layer of matter (energy-loss straggling), are described by the Vavilov distribution [3]. In the limit of many collisions the Vavilov distribution becomes a Gaussian:

$$f(\Delta E) = \frac{1}{\sqrt{2\pi}\sigma} e^{\frac{(\Delta E - \overline{\Delta E})^2}{2(\sigma_E)^2}} \qquad \sigma_E = 4\pi Z_{eff} Z_t e^4 N \Delta x \left[\frac{1-\beta^2/2}{1-\beta^2}\right] \tag{1.9}$$

The variances $\sigma_R^2$ and $\sigma_E^2$ of the range and energy-loss straggling respectively, are related by the following equation:

$$\sigma_R^2 = \int_0^{E_i} \left(\frac{d\sigma_E}{dx}\right)\left(\frac{dE}{dx}\right)^{-3} dE \tag{1.10}$$

The ratio between $\sigma_R$ and the mean range $R$ is nearly constant and can be described by:

$$\frac{\sigma_R}{R} = \frac{1}{\sqrt{M}} f\left(\frac{E}{Mc^2}\right) \tag{1.11}$$

where $M$ and $E$ are respectively the projectile mass and energy while $f$ is a function depending on the absorber. As a consequence the relative range straggling is smaller for heavier particles (see Fig. 1.5). In addition due to the $1/\sqrt{M}$ dependence, the range straggling of carbon ions is smaller than the one of protons by a factor of $\sim 3.5$.

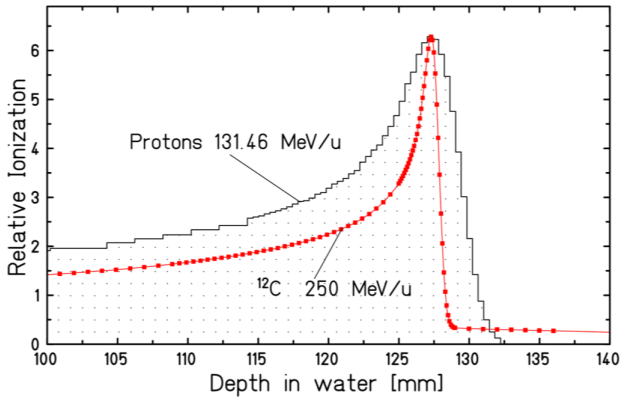


**Figure 1.5.** Bragg peaks of protons and carbon ions with the same range in water. For carbon ions, secondary particles produced in nuclear interactions cause the tail beyond the peak, while for protons the dose tail is absent. Extracted from [4].

In Fig.1.5 is also possible to observe for the carbon ions, a dose tail beyond the BP. As it will be explain in details in sec.1.2, the projectile fragmentation that occurs when a ion beam with $Z > 1$ interacts with matter, leads to an attenuation of the primary particles: due to nuclear inelastic processes, a monochromatic incoming beam turns in fact into a mixed beam containing neutrons and lower-Z fragments, which may have a broad energy distribution and increased penetration depth, according to Eq.1.6, that allow them to release energy beyond the BP.

The small lateral deflection of ions beam penetrating through an absorber, is manly caused by elastic Coulomb interactions with the target nuclei. The statistical distribution function $F(\theta, d)$ for the resulting scattering angle $\theta$ at penetration depth $d$ can be obtained from the integral equation given by Bethe. The analytical solution of this equation, given by Molière, can be approximated for small angles, by a Gaussian function:

$$F(\theta, d) = \frac{1}{\sqrt{2\pi\sigma_\theta}} exp(-\frac{\theta^2}{2\sigma_\theta^2}) \tag{1.12}$$

with a standard deviation equal to:

$$\sigma_\theta[rad] = \frac{14.1MeV}{\beta pc} Z_p \sqrt{\frac{d}{L_{rad}}} \left[1 + \frac{1}{9} log_{10}\left(\frac{d}{L_{rad}}\right)\right] \tag{1.13}$$

The absorber material is characterized by the thickness $d$ and the radiation length $L_{rad}$.
The angular spread for heavy charged particles is small, but increases significantly towards low energies due to the $\beta pc$ term in the denominator of Eq.1.13. In conclusion, two different contributions to the angular beam spreading have to be considered:

1. The scattering caused by materials in front of the patient;
2. The scattering in tissue between entrance point and stopping depth.

At low energies the first effect represents the dominant contribution because even a small angular spread translates in a significant broadening of the beam spot due to

the path typically $0.5 - 1.0$ m before entering the patient. At high energies while the first contribution becomes less important the second one increases due to the large penetration depths in tissue.
Fig.1.6 shows a comparison between the beam spread of $^{12}C$ ions and protons with respect to penetration depth[4].

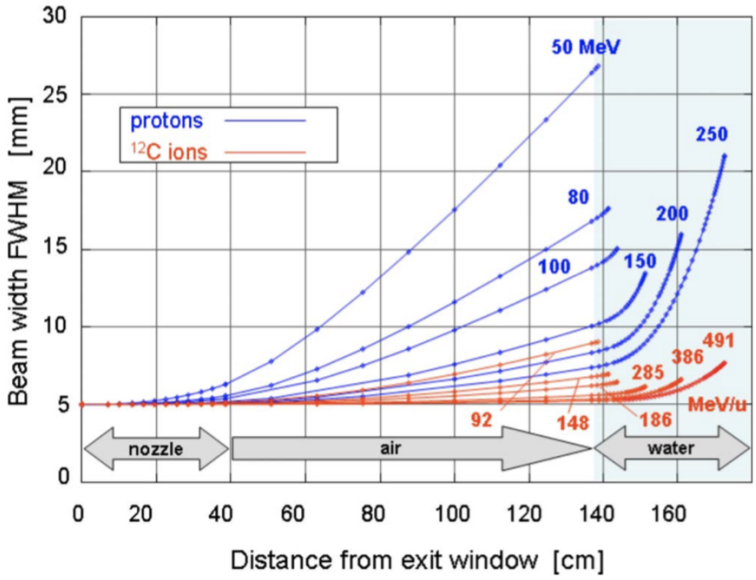


**Figure 1.6.** At small depth the width is mainly determined by scattering in the nozzle, while at higher energies the scattering in the water absorber dominates. Carbon ions show a much smaller spread than protons at the same penetration depth.

## 1.2 The rule of nucleus-nucleus interactions

The heavy ions path at high energy in a thick absorber is governed by collisions with atomic electrons. The probability of nuclear reactions is smaller but leads to significant effects at large penetration depths. At energies of several hundred MeV/u violent nuclear reactions may result in a complete or partial fragmentations of both projectile and target nuclei. The most frequent nuclear reactions are the peripheral collisions, which are characterized by a relatively small energy and momentum transfer, since not all the nucleus of the projectile and the target interacts effectively. Consequently only few fragments are produced. This process can be described by the *abrasion-ablation* model as a two step process [5]. In the first step both projectile and target nucleons that are in the overlapping reaction zone (the "fireball") interact with each other while the outer nucleons are only slightly affected. The remaining projectile and target fragments then de-excite by evaporation of nucleons in the second step.
The high-energy fragmentation reactions that occur along the beam path in the tissues lead to the primary beam attenuation and the accumulation of secondary low-charge fragments that give rise to the characteristic dose tail behind the BP. These effects become significant in the presence of a large initial energy and consequently of a great penetration depth of the primary beam.

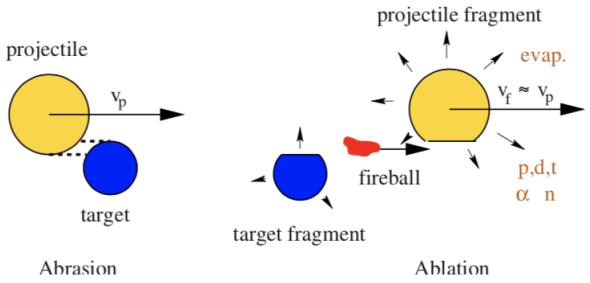


**Figure 1.7.** Schematic view of a nucleus-nucleus collision.

In general, nuclear reactions occur in two distinct cases, namely projectile and target fragmentation. In the case of proton beams, only the second process occurs, which can be described as follows:

$$p + x \rightarrow p + \sum_i x_i \tag{1.14}$$

where $p$ si the projectile, $x$ is the target and the $x_i$ are its fragments. In this case the kinetic energy of the secondary particles is lower than the one of the incident particle:

$$T_{x_i} << T_p \qquad \left(\frac{dE}{dx}\right)_x >> \left(\frac{dE}{dx}\right)_p \tag{1.15}$$

Fig.1.8 shows the projectile fraction and the LET for 150 MeV protons, comparing the ones that have undergone and not nuclear reactions within the tissue, as a function of the penetration depth in water. These figures results from GEANT4 simulations [1].

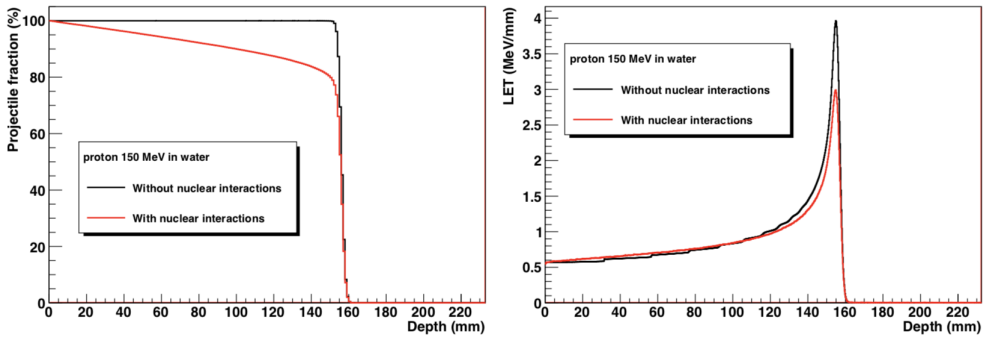


**Figure 1.8.** Evolution of the primary protons ratio (left panel) and the mean LET (right panel) for 150 MeV protons with the penetration depth that have (red curve) and do not have (black curve) undergone nuclear reactions inside the tissue.

On both panels, the black and red curves corresponds to simulations in which the nucleus-nucleus collision process has been deactivated ("EM" in the following) and activated ("NUC" in the following), respectively. Whereas all projectiles reach the BP for EM simulations, only 80% of them reach for NUC simulations. As a consequence, the energy deposition at the BP, whose position remains unchanged, is reduced by 20% for NUC collisions compared to EM collisions. The contribution of secondary fragments is not directly seen in Fig.1.8: their velocity is very small, their range do not exceeds few micrometers so they deposit their energy close to the

collision location. The presence of secondary fragments occurs indirectly in the total amount of energy deposited in the tissue. Since some energy is needed to produce fragments, each time a proton collides on a nucleus, one part of the total energy of the system is exhausted in the particle production. As a result, the integral $\int LET(x)dx$ of the Bragg curve for NUC simulations is only 97% of the projectile incident energy, whereas this integral is equal to the projectile incident energy for EM simulations.

The influence of the nucleus-nucleus reactions on the dose deposition for $^{12}C$ ions is very similar as it can be observed from Fig.1.9 which has been obtained for 290 MeV/n carbon ions using the GEANT4 simulation toolkit. In this case both projectile and target fragmentation processes occur. In the first case the produced fragments are fast, with a kinetic energy similar to the primary ion one and, since they have lower charge and mass, their range is longer compared to the beam particles one:

$$T_{x_i} \simeq T_c \qquad \left(\frac{dE}{dx}\right)_x \leq \left(\frac{dE}{dx}\right)_c \tag{1.16}$$

Therefore they generate a longitudinal tail in the dose deposition curve, delivering an unwanted dose beyond the BP, named *fragmentation tail*. Only 50% of projectiles reach the BP (left panel of Fig.1.9), leading to a reduction of 50% on the energy deposition per incident carbon ions at the BP (right panel of Fig.1.9).

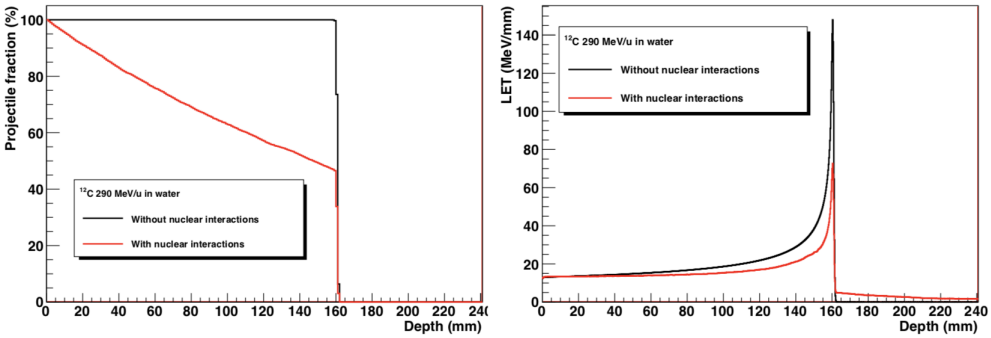


**Figure 1.9.** Evolution of the primary carbon ions ratio (left panel) and the mean LET (right panel) for 290 MeV $^{12}C$ ions with the penetration depth that have (red curve) and do not have (black curve) undergone nuclear reactions inside the tissue.

The ratio of $^{12}C$ ions which do not experience a nuclear interaction decreases exponentially with respect to the penetration depth. As for protons, the locations of the BP are equal for EM and NUC simulations.

### 1.2.1 Influence of the total reaction cross section

The occurrence of a nucleus-nucleus collision is driven by the total cross section $\sigma_R$. The number of interactions $N_{reactions}$ in which occur a nucleus-nucleus reaction when $N$ projectiles in a beam of surface $S$ crosses a material of thickness $dx$ is:

$$N_{reactions} = N\frac{N_t\sigma}{S} \tag{1.17}$$

$N_t$ is the number of target nuclei, equal to:

$$N_t = \frac{N_A\rho S dx}{M_{mol}} \tag{1.18}$$

where $N_A$ is the Avogadro's number, $\rho$ the material density and $M_{mol}$ the material molar mass (see Fig.1.10). The variation $dN$ of the number of projectiles which remain unchanged after a path length $dx$ is than:

$$dN = -N_{reactions} = -N\frac{N_A\rho\sigma}{M_{mol}}dx \tag{1.19}$$

and solving the differential equation:

$$N(x) = N_o e^{-\frac{x}{\lambda}} \tag{1.20}$$

with $\lambda$ that represents the mean free path, equal to:

$$\lambda = \frac{M_{mol}}{N_A\rho\sigma} \tag{1.21}$$

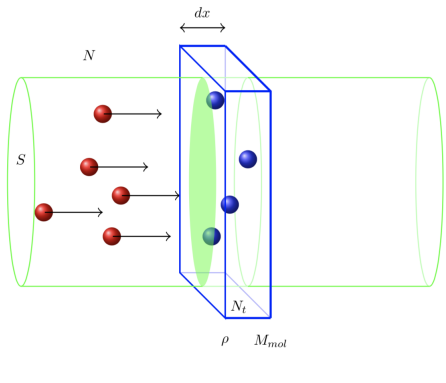


**Figure 1.10.** Schematic view of the interaction of a beam of ions crossing a piece of absorber .

Tab.1.1 shows typical values of cross section and mean free path in water for different incident particles.

| Ion | E [MeV/n] | $\sigma_R$ [mb] | $\lambda$ [cm] |
|---|---|---|---|
| Proton | 200 | 352 | 85.2 |
| $^{4}$He | 200 | 767 | 38.6 |
| $^{12}$C | 380 | 1424 | 20.8 |
| $^{20}$Ne | 530 | 1929 | 15.5 |

**Table 1.1.** Energy, total reaction cross section and mean free path in water of ions with about 25 cm range in water[6].

It is also useful to study the cross section behavior as a function of the incident beam energy. As an example, Fig.1.11 shows the trend, obtained from the "Experimental Nuclear Reaction Data (EXFOR)" database, for the following reaction:

$$ {}^{12}_{6}C + {}^{12}_{6}C \rightarrow \alpha + {}^{20}_{10}Ne \tag{1.22} $$

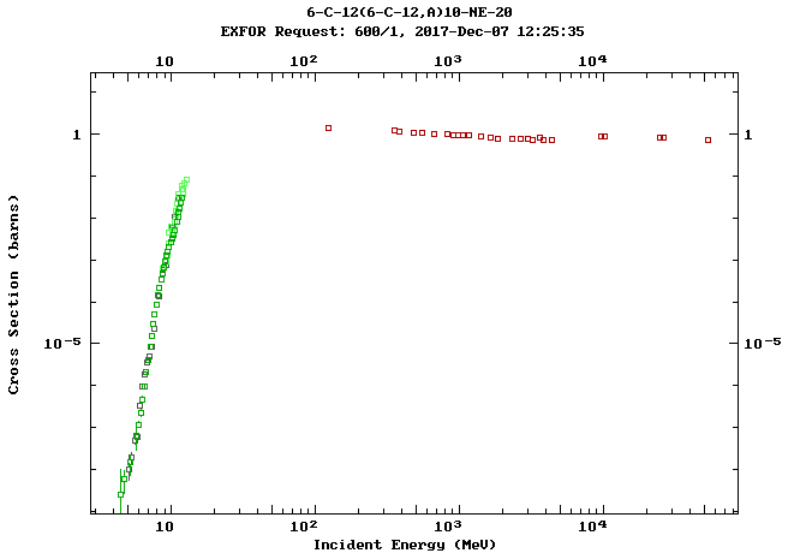


**Figure 1.11.** Cross section behavior with respect to the impinging energy. The green and black points are the data obtained from the reaction ${}^{12}_{6}C + {}^{12}_{6}C \rightarrow \alpha + {}^{20}_{10}Ne$ in different experiments, while the red ones represent the total cross section of the process.

The threshold energy is obtained as the $E$ value at half height of the cross section rising edge. Using this value, it is possible to calculate the residual path $R$ from the following formula:

$$ R = R^* \frac{A}{Z^2} \left( \frac{T_o}{c^2 M} \right)^{1.82} \tag{1.23} $$

where $R^*$ in water is equal to 425 cm, $T_o$ is the threshold energy equal to $9.80 \pm 0.01$ MeV corresponding to a cross section value equal to $0.0021 \pm 0.0002$ barn.
$R = 3.86 \pm 0.02 \mu$m is then obtained: the particle, after a "$R$ long" path stops and the ionization processes ends.

### 1.2.2 The secondary particles contribution

The secondary particles contribution is twofold. Firstly, a fraction of the incident particle kinetic energy is exhausted in the nuclear interaction to produce secondary fragments.
Assuming a projectile of mass $m(A_p, Z_p)$ with a kinetic energy $T_p$ that hits a target nuclei of mass $m(A_t, Z_t)$ and produces a set of fragments of mass $m(A_i Z_i)$ and kinetic energies $T_i$, the energy conservation leads to the following equation:

$$ m(A_p, Z_p)c^2 + T_p + m(A_t, Z_t)c^2 = \sum_i [m(A_i, Z_i)c^2 + T_i] \tag{1.24} $$

Introducing the $Q\text{-}value = m(A_p, Z_p)c^2 + m(A_t, Z_t)c^2 - \sum_i m(A_i, Z_i)c^2$, the Eq.1.24 becomes:

$$\sum_i T_i = T_p + Q \tag{1.25}$$

For small systems ($Z < 26$) the *Q-value* is negative and therefore the sum of the produced fragment kinetic energies is smaller than the projectile kinetic energy.
The second contribution given by the secondary particles to the dose map is the energy they deposit in the target material. Besides contributing to the *dose tail* beyond the BP, the fragments produced all along the projectile path, also deposit energy behind and at the BP. As a consequence, the mean LET at depth $x$ is given by the weighted sum of all particles mean LET present at $x$:

$$\overline{LET(x)} = \sum_i \nu_{A_i,Z_i}(x)\overline{LET_{A_i,Z_i}(x)} \tag{1.26}$$

where $\nu_{A_i,Z_i}$ is the multiplicity of fragments with charge number $Z_i$, mass number $A_i$ and $\overline{LET_{A_i,Z_i}}(x)$ is their mean LET at depth $x$.
Measured buildup curves for charged fragments of primary carbon ions with $Z$ between 1 and 5 are shown in Fig.1.12

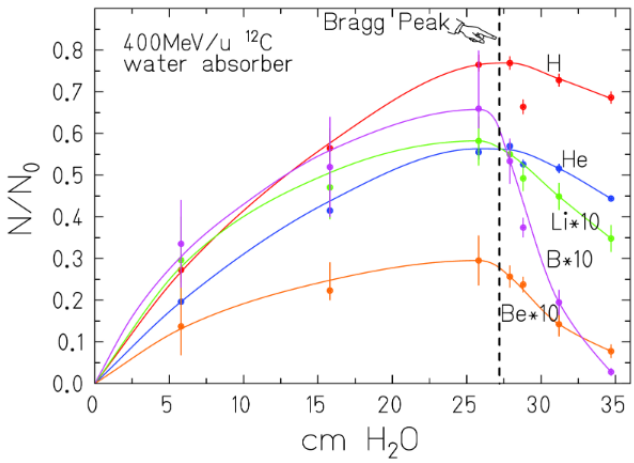


**Figure 1.12.** Buildup of secondary fragments produced by 400 MeV/n $^{12}C$ ions stopping in water. The lines are shown to guide the eyes. Extracted from [7].

Hydrogen and helium fragments, that are most abundantly produced, contribute significantly to the longitudinal tail in the dose deposition curve due to their longer range compared to the beam particles one.

In Fig.1.13 an estimation of the secondary particles contribution to the mean LET value is reported. The right panel is a magnification of the left panel. These figures show the mean LET value of all particles with respect to the penetration depth in water: the one of the secondary particles reaches at most $\sim 7\%$ of the mean LET value at the BP. The main contributors are the hydrogen, helium and boron isotopes behind the BP while before it are the hydrogen and helium isotopes.

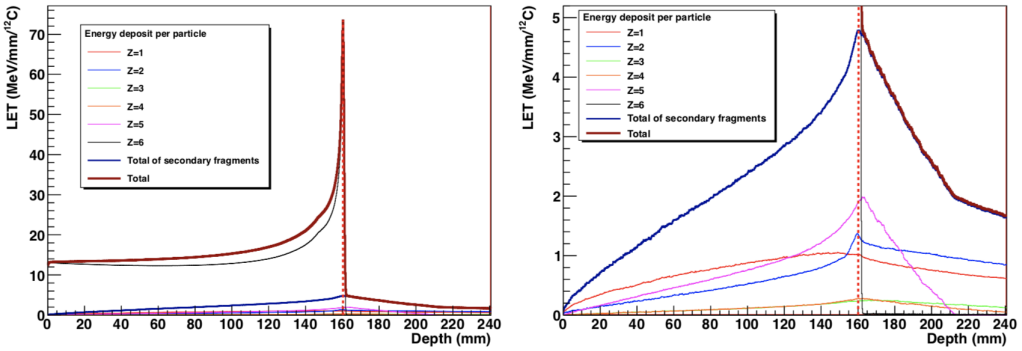


**Figure 1.13.** Mean LET value of secondary fragments for $^{12}C$ ions at 290 MeV/u (GEANT4 simulations). The right panel is a zoom on the right panel on low LET values.

## 1.3 Biological Effectiveness of Ion irradiation

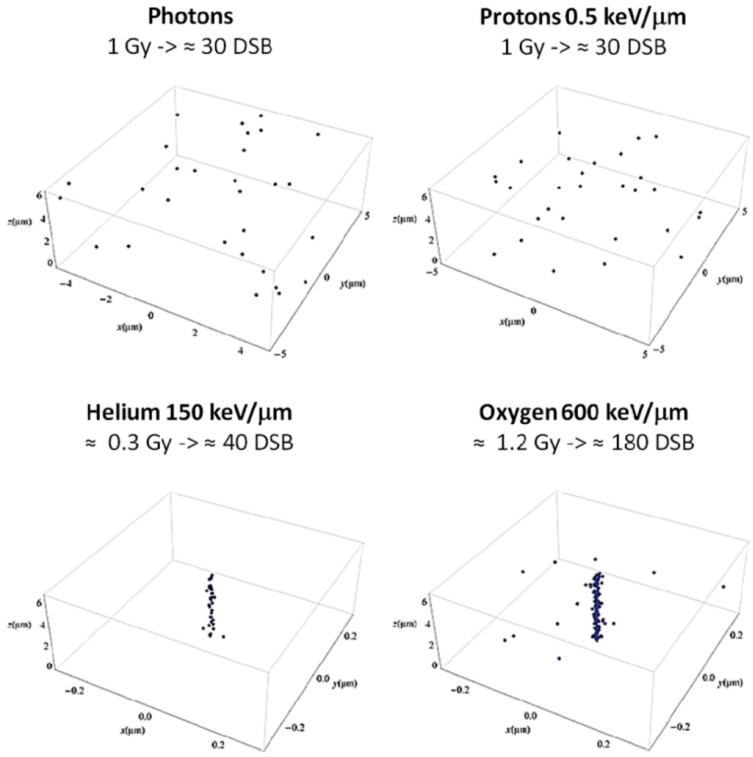


**Figure 1.14.** Simulated patterns of DSB distribution after photon and ion irradiation in a typical cell nucleus (radius $\sim 5$ $\mu$m). Protons show a photon-like distribution of lesions (*sparsely ionizing*) while alpha particles and oxygen ions show a typical target fragments produced in particle therapy. In the last case a considerable dose is released in the nucleus and a high dose is released close to the particle track (*densely ionizing*).

The radiotherapy purpose is to induce biological damage in cancer cells and avoid their proliferation. The principal radiation target is the DNA inside the cellular

nuclei.
The ionizing radiation acts on the DNA in direct or indirect ways: in the first case the DNA damages are induced by *direct* hits of the ion or its surrounding secondary electrons while in the second case they are generated by radiation-induced radicals. These biological effects are caused by double or single DNA filament damages. Since the filament has a thickness equal to $\sim 2$ nm, a LET of about 25 keV/$\mu m$ is required to break the filament twice.
The ionizing radiation effects depends mostly on the LET values: from Eq.1.6 a LET dependence from the particle charge is observed ($Z_p^2$). Depending on the incident beam energy, *direct* (high LET) and *indirect* (low LET) hits are observed. In general the ionization events generated by low LET radiations (particles with an energy value around $0.2 - 0.5$ keV/$\mu$m, i.e. photons emitted by $^{60}Co$ source) are quite separate from each other. For this reason, these particles are indicated as *sparsely ionizing*. Instead the high LET radiations (particles with energy value of the order of 100 keV/$\mu$m, i.e. carbon ions) are called *densely ionizing*.
Fig.1.14 shows a comparison of expected Double Strand Breaks (DSB) distributions after low and high LET irradiation [8].
Due to the LET dependence to the penetration depth, the dose release along the charged particle path is not uniform and the ionization density increases as the distance from the BP decreases. Assuming a 4800 MeV carbon ions beam, Fig.1.15 shows for different distance from the BP placed at 30 cm of penetration depth, the LET value and the distance $d$ between two consecutive ionizing events.

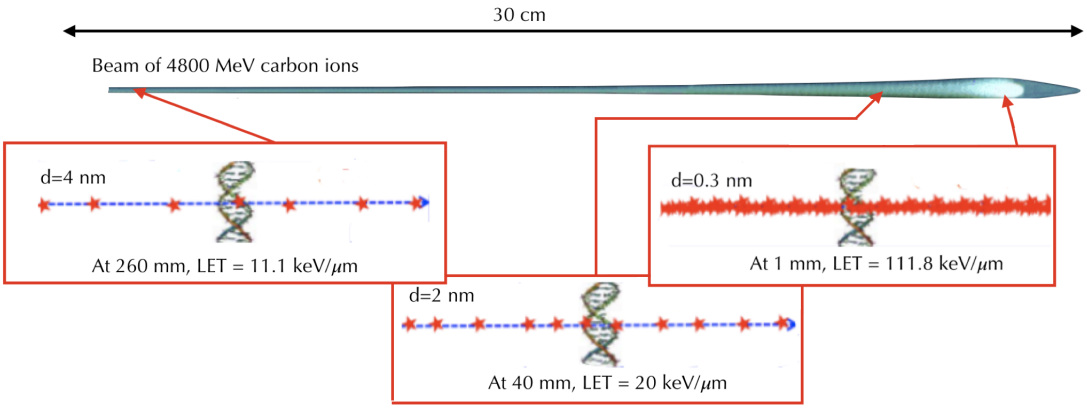


**Figure 1.15.** Ionization density for different distance from the Bragg Peak placed at 30 cm of penetration depth. The data are obtained considering a Carbon ion beam at 4800 MeV that crosses a water target. $d$ indicates the distance between two consecutive ionization events.

The energy absorbed locally by the medium increases, the ionization events become closer to each other: at the BP the number of interactions and thus the dose released is maximum. It is also observed that for LET values greater than 11.1 keV/$\mu$m, double breaks in the DNA filament occur.
In Fig.1.16 is reported the same case for a 200 MeV protons beam.

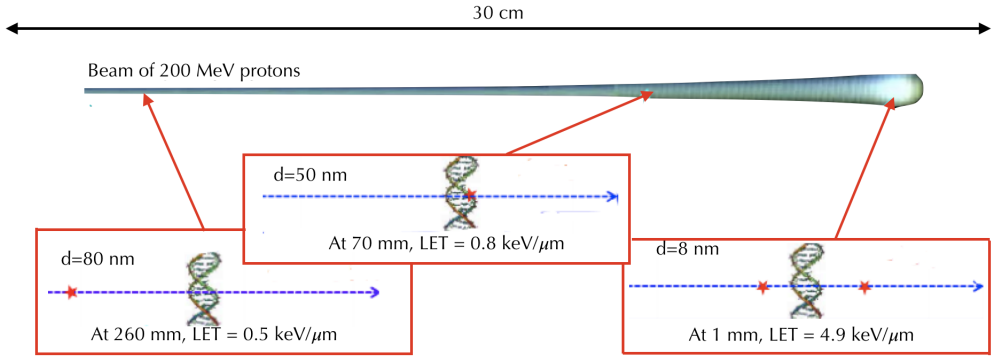


**Figure 1.16.** Ionization density for different distance from the Bragg Peak placed at 30 cm of penetration depth. The data are obtained considering a proton ion beam at 200 MeV that crosses a water target. $d$ indicates the distance between two consecutive ionization events.

In this case, as it can be also observed in Fig.1.14, the protons for LET values less than 4.9 keV/$\mu$m cause only a single DNA helix damage.
It can therefore be concluded that, due to the thickness of the double helix (2 nm) and to the small cell repair capacity for a more complex DNA damage, the high LET radiations have a probability of producing a DNA double break damage higher compared to those with low LET.

### 1.3.1 DNA damage and cell inactivation

A common way to analyze the different effects of photons and heavy ions is by means of cell survival curves. These experiments give insight into the potential of radiation in killing tumor cells. In the standard experimental protocol, cell proliferation is analyzed about $1-2$ weeks after irradiation and cells are counted as survivors, if they have formed a colony with more than 50 daughter cells. The surviving fraction is given by normalization to the number of seeded cells. The most common way to parametrize the cell survival $S$ uses the linear-quadratic model:

$$S(D) = exp(-\alpha D - \beta D^2) \tag{1.27}$$

where $D$ is the absorbed dose and $\alpha$ and $\beta$ are experimentally determined parameters. The ratio $R = \alpha/\beta$ determines the shoulder of the survival curve and it gives an indication of the cellular repair capacity. Low R ratio is associated with a prevalence of repairable damage, while high R value is related to a severe non repairable damage. Both cases are presented in Fig.1.17: the curve associated with X-ray radiation shows a clear shoulder, while the ones related to carbon ions irradiation shows a more linear tendency. In the same figure, is observed that distinct carbon ion energies result in different cell survival curves. Ions with high energies have also high velocity, so the LET is low ($dE/dx \sim 1/v^2$) and the ionization density is small.

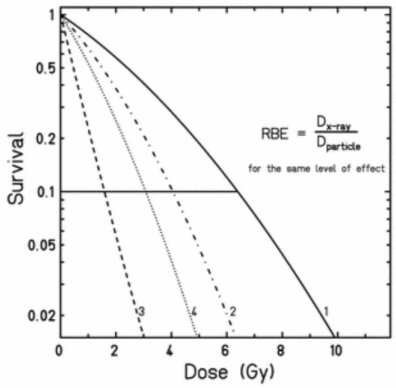


**Figure 1.17.** Survival curves for CHO-K1 cells irradiated with x-rays (1) and carbon ions of different energies: 266.4 MeV/n and LET= 13.7 keV/$\mu m$ (2), 11.0 MeV/n and LET = 153.0 keV/$\mu m$ (3), 2.4 MeV/n and LET= 482.7 keV/$\mu m$ (4)[9].

In this case the damage caused by the ions can be repaired more frequently and the survival curve (curve 2 in Fig.1.17) present a small shoulder. When the initial energy decreases, the LET increases. Therefore ions have a higher ionization density leading to a higher probability to produce unrepairable damages (curve 3). At very low energies (curve 4), the survival curve shows minor biological effects. This is the result, as will be explained in the next section, of two phenomena: a saturation effect ("overkill") occurs when a single particle releases an higher amount of energy than the amount required to kill the cell, so its energy is wasted. Furthermore the energy loss rate increases as the particle slows down, so at very low energies the fluence of particles required for a given quantity of dose is very small, thus a certain portion of cells may not be hit.
Biological effects depend on various factors, most of which are summarized in the *Relative Biological Efficiency* coefficient (RBE).

### 1.3.2 Relative Biological effectiveness

The RBE is defined as the ratio of the dose of a reference radiation (typically x rays or $\gamma$ rays) to the dose of the radiation in question, i. e. ions, to produce an identical biological effect (isoeffect).

$$RBE_{iso} = \frac{D_{ref}}{D_{ion}} \tag{1.28}$$

In Fig.1.18 the determination of the RBE by typically cell survival curves for X-rays and heavy ions is shown. The RBE values for cell inactivation are indicated for two effect levels, namely 10% and 1% cell survival. Depending on the survival rate, the RBE can range form 1.5 to 2.1. The average RBE is around 1.1 for protons while for carbons is around 3.

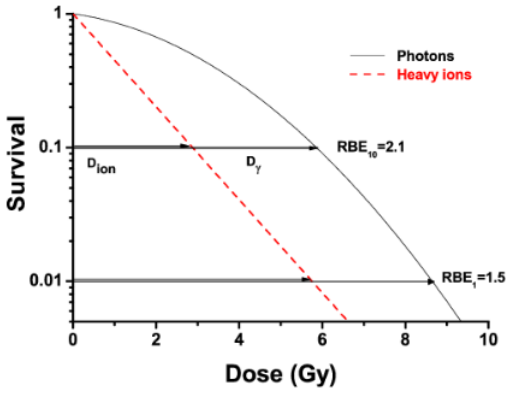


**Figure 1.18.** Determination of the RBE for cell inactivation for 10% and 1% cell survival.

In the experimental practice it is difficult to measure the released dose and evaluate the RBE through Eq.1.28. An alternative variant of RBE is the $RBE_\alpha = \alpha_{test}/\alpha$, where $\alpha_{test}$ and $\alpha$ are the linear part of the survival curve for photons and the tested particle respectively.
The main purpose of hadrontherapy is to overcome a good compromise between the damage to the cancer cells and the one to the surrounding healthy tissues. In particular it is necessary to reach high RBE values in the same range of SOBP and at the same time, to minimize the biological effects before and after the tumor region.
Fig.1.19 shows the RBE values for different ions as a function of the penetration depth inside a hypoxic tissue. As shown in the figure, carbon ions have high RBE close to the Bragg peak while in the entrance region the RBE is lower when compared to the other ions.

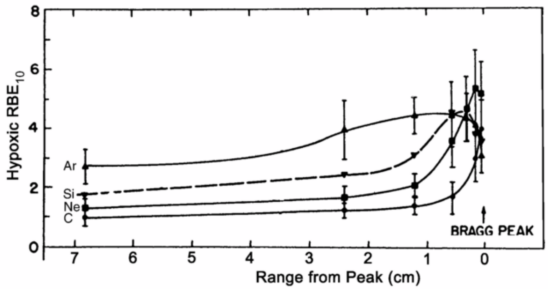


**Figure 1.19.** RBE for carbon (C), neon (Ne), silicon (Si) and argon (Ar) ions as function of the penetration depth inside a hypoxic tissue [10].

The RBE depends on different quantities, such as the dose level, the radiation quality and consequently the LET, the radiation type and the biological effect considered. In Fig.1.20 the dose level and particles LET dependence can be observed: the RBE value is higher for low dose levels and increases with the LET (ionization events increase and consequently improve the biological effects). As explained in the previous section, RBE increases with LET up to a maximum value and decreases for higher LET values regardless of the particle type.

In the same figure, the particle type influence on the maximum RBE position is reported. For heavier particles, the maximum is typically shifted to higher LET's. This is because, given a LET value, heavier ion are faster than lighter particles, leading to a lower ionization density and lower biological effectiveness.

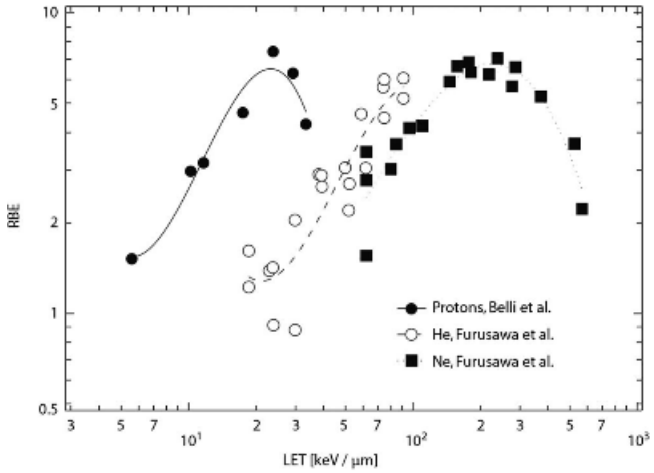


**Figure 1.20.** Dependence of the $RBE_\alpha = \alpha_{ion}/\alpha$ on LET and particle type, where $\alpha$ and $\alpha_{ion}$ are the linear part of the survival curve for photons and ions, respectively [11].

The RBE maximum depends also on the radiosensitivity of the target cells. Fig. 1.21 shows $RBE_\alpha$ dependence on LET and the survival curves for the three hamster cell lines with different radiosensitivities irradiated with carbon ions.

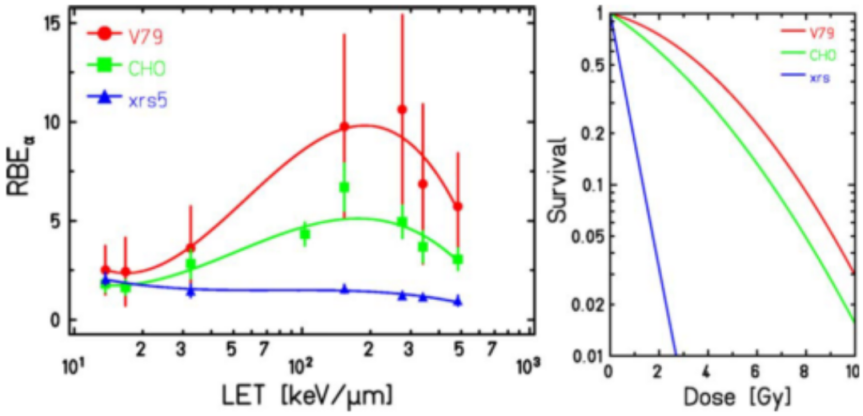


**Figure 1.21.** RBE dependence on the radiation sensitivity of cell lines. Left: Dependence of initial $RBE_\alpha$ on the three cell lines CHO, V79, and XRS after carbon irradiation. Right: Survival curves of the same cell lines demonstrate the different radiosensitivities after X-ray irradiation[12]. Experimental data are form [13].

As shown on the left panel, the V79 cell line shows the largest shoulder in the survival curve, implying it has a good repair capability and it is the most resistant to conventional irradiation. The XRS cells are the most sensitive to photon radiation, so they have a larger $\alpha/\beta$ ratio involving a poor repair capacity. The CHO cell line have intermediate biological characteristics. Therefore, as one can notice from

the left panel of Fig. 1.21, systems with high repair capacity have higher RBE maximum.

### 1.3.3 Proton radiation damage

To better understood the nuclear interactions contribution to the proton RBE, Fig.1.22 shows the survival data obtained with V79 cells after irradiation with $\gamma$ rays and with protons at 160 MeV [14]. The survival curves for Chinese hamster cells irradiated with $^{60}Co$ $\gamma$ rays and plateau- region 160 MeV protons are similar, indicating that, when the effects of the nuclear interactions are not considered, the behavior of high energy protons is like that of $\gamma$ rays. The proton data are also well fitted by the model on which the production of secondary fragments is being taken into account. The result obtained indicates that the low energy recoil particles contribution is significant. Thus in clinical context, due to the high RBE values expected for the secondary particles, the contribution arisen form the nuclear reactions might be especially relevant at the low dose deposited in the entrance region. However, very limited information is available in the literature in terms of biological experiments.

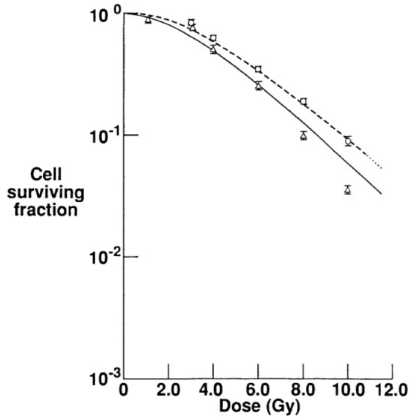


**Figure 1.22.** Experimental data of cell inactivation obtained with V79 cells after irradiation with 60Co $\gamma$ rays (circles) and with 160 MeV protons (triangles). The dashed line is the fit to the experimental $\gamma$ rays survival curve, the dotted one is the result for primary protons only while the solid line includes the effects of nuclear reactions.[8].

Fig. 1.23 shows different proton RBE values, extracted from Particle Irradiation Data Ensamble (PIDE) database [15], as a function of LET. Looking at Fig. 1.23 it is clear that, although the $\alpha/\beta$ ratio is not considered, there are big fluctuations and discrepancies observed in the results of different experiment. As a result of an incomplete understanding of the underlying processes, in the treatment planning the proton RBE is assumed to be 1.1 along all the range, independently of the tissues irradiated, dose per fraction, total dose and beam energy. This simplification could result in an under or overestimation of RBE in the entrance region.

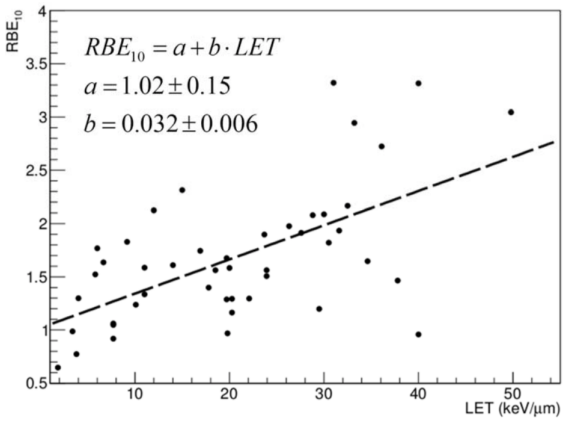


**Figure 1.23.** RBE values for 10% survival. Values extracted from PIDE. The dashed line shows the tendency to an increase RBE with LET (result of a linear fit). All values are polled together, independent of $\alpha/\beta$ ratio.

In addition to the physical uncertainties, biology can contribute with the so-called "biological range extension"[8]. At the distal fall-off of the SOBP, a parallel increase of LET and decrease of the dose occur, resulting in an increase of RBE. This result can lead to a relevant biological dose deposition beyond the tumor region, i.e. in healthy tissues.

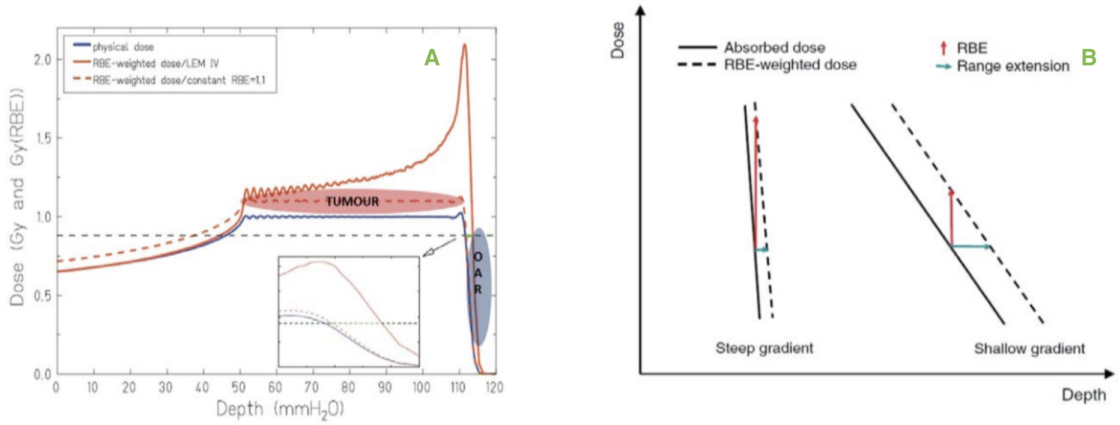


**Figure 1.24.** In panel (A) physical and RBE-weighted dose are shown, as obtained with a costant and with a variable RBE. In panel (B) the different impact in terms of range extension that can be expected when comparing steep and shallow dose gradients is show [16].

In Fig. 1.24 panel (A), is reported a comparison between the physical dose, the weighted dose with a variable RBE and the weighted dose with a constant RBE. In particular in the distal portion of the curves, where at-risk organs could be found, in the case of variable RBE the peak decreases at penetration depths slightly bigger than the ones for the constant RBE. According to the fixed RBE of 1.1, this extension, caused by a gradual increase in RBE, is not currently considered in treatment planning. Looking at Fig.1.24 panel (B), it can be observed that steep and shallow dose gradients correspond to short and large range extension, respectively. In addition, the dose gradient that can be associated with the

distal penumbra is also strongly dependent on the beam modulation techniques: active scanning will produce steeper dose gradients compared to passive modulation system for irradiation of the same target. However, very few data related to a clinical context can be found in the literature concerning the biological extension impact.

At the moment no clinical data reports the induction of serious side effects against the use of a fixed RBE for protons. However, as already said, a constant RBE value can lead to a possible inadequacy in the proton therapy application: the RBE increase can give rise to a biological range extension beyond the BP or to an increase of biological damage in the entrance region, i.e. in the region of healthy tissues. In Fig.1.24 is reported a schematic approach to give indications concerning the expected contributions of electromagnetic interaction and fragmentation along the BP in terms of biological effects. As can be seen in Fig.1.25, the target fragmentation in proton beam is more relevant in the entrance channel region where the impact of nuclear fragmentation as compared to ionization induced cell killing is less (the ratio between the cells damaged by the generated fragments and the ones damaged by the ionization process is 1/8 ) than in the peak region (the same ratio is equal to 1/40).

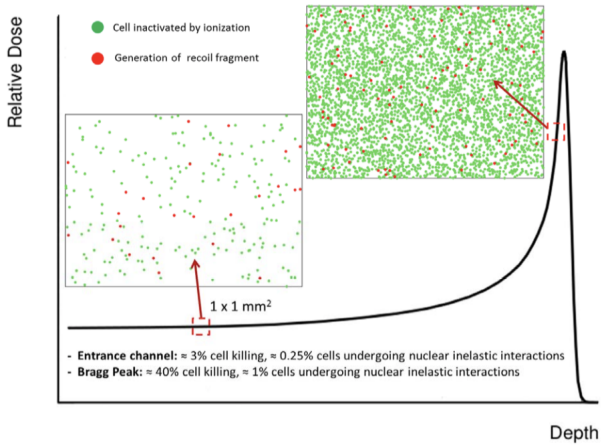


**Figure 1.25.** Illustrative image of the expected relative impact of the target fragments in the entrance channel region and in the BP region as compared to the effect of inactivation by ionization. The image is obtained using a 250 MeV/n protons beam impinging on $1mm^2$ water target. The green points represent the cells damaged by the ionizing contribution while the red ones represent the cell damaged by the fragmentation processes[8].

Therefore, it is essential to improve the knowledge about the role of nuclear fragmentation in proton therapy. To preserve the healthy tissues and improve the treatment planning a more complete proton RBE model, which include the fragmentations effects, must be obtained.

## 1.4 Experimental cross section

The FOOT experiment has been conceived in order to perform a set of measurements of nuclear fragmentation cross sections. These data are essential to improve the treatment plan accuracy and to develop a new Treatment Planning Systems (TPS) for both protons and heavy ions by providing an accurate description of nuclear

interactions that occur between the beam and the patient tissue. In addition FOOT is suitable to perform fragmentation study for Radio Protection in Space (RPS), in particular for spacecraft shielding optimization, collecting data with helium, carbon and oxygen beams at $150 - 450$ MeV/n impinging on different targets materials. Nowadays there is a lack of experimental measurements of the nuclear reaction cross sections for the fragments produced by protons with energies between 60 and 250 MeV (typical energies for hadrontherapy) and energies of interest for the RPS. This is why nuclear models are used when experimental data are not available. A review of the available interaction cross sections of protons on carbon, oxygen and calcium (the most important interactions that occur in the human body in medical applications) can be found in [17], where the authors compared experimental data drawn from the EXFOR [18] and Landot-Börnstein [19] databases. These data include measurements of reaction cross sections (see Fig.1.26) and isotopic production cross sections (see Fig.1.27-1.28).

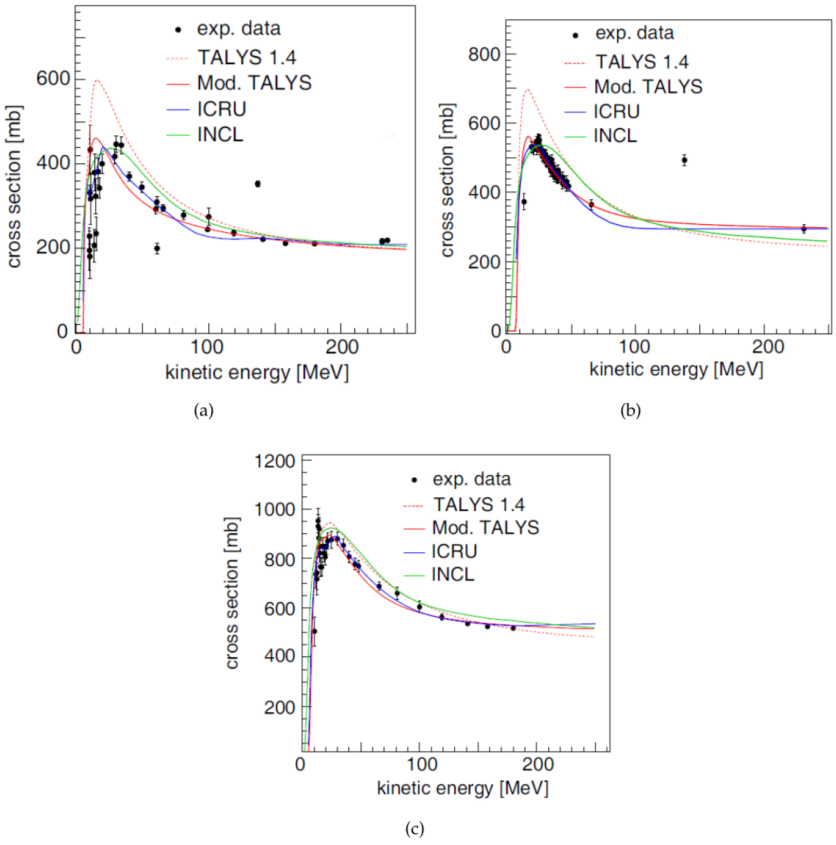


**Figure 1.26.** Reaction cross sections for the $\mathbf{p} + {}^{12}C$ (a), $\mathbf{p} + {}^{16}O$ (b) and $\mathbf{p} + {}^{40}Ca$ (c). Experimental data (black dots) are compared to the prediction of different models: two different versions of the TAYLS code [20], the ICRU63 evaluation [21] and the INCL coupled to the ABAla07 de-excitation code [22] [23].

As can be observed from the figures, the prediction differences between the models confirm that they are not able to reproduce the experimental data with the accuracy required for space and therapy applications. In particular the discrepancies

for isotopic production cross sections are more pronounced at high energies, where the database are less populated.
It is important to note also that the energy-differential cross sections for each produced fragments are missing. The knowledge of fragments energy is, however, crucial since it effects the range inside the tissues (see Eq.1.23).

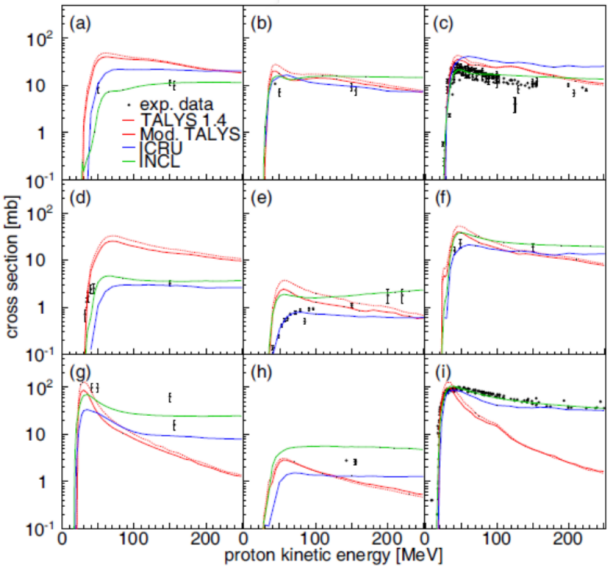


**Figure 1.27.** Production cross sections of (a) $^{6}$Li, (b) $^{7}$Li, (c) $^{7}$Be, (d) $^{9}$Be, (e) $^{10}$Be, (f) $^{10}$B, (g) $^{11}$B, (h) $^{10}$C and (i) $^{11}$C from the p+$^{12}$C reaction. Line colors and symbols have the same meaning as in Fig.1.26.

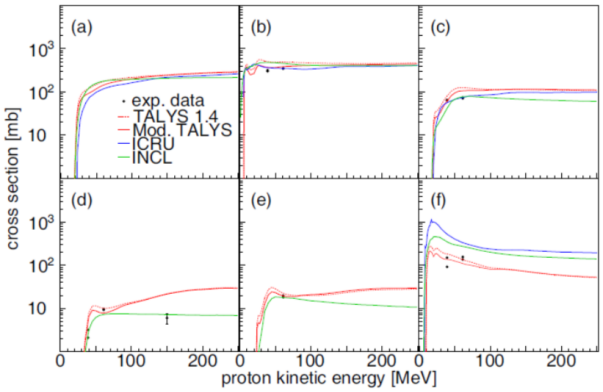


**Figure 1.28.** Production cross sections of (a) neutrons, (b) protons, (c) deuterons, (d) tritons, (e) $^{3}$He and (f) $^{4}$He from p+$^{12}$C reaction. Line colors and symbols have the same meaning as in Fig.1.26.

Due to the growing interest on ions beams for cancer treatments several experiments have been carried out to study helium, carbon and oxygen ion beam fragmentation. At GSI laboratory the production yields, energy spectra and angular distributions of H and He isotopes from $^{12}$C have been studied for a 200 MeV/u

on a water target [24]. At GANIL, France, the double differential cross sections and the angular distributions of secondary fragments produced by a 95 MeV/u and 50 MeV/u on C, $C_2H_4$ , Al, $Al_2O_3$, Ti and PMMA have been measured [25]. The Fragmentation of Ions Relevant for Space and Therapy (FIRST) experiment [26] at GSI studied the nuclear interactions of a 400 MeV/u $^{12}$C ion beam on C and Au thin targets by measuring the differential cross sections.
Recent experiments have provided some initial data about $^{4}$He fragmentation in PMMA targets. In particular the fluxes and energy spectra of H and He isotopes were measured at HIT for 102 MeV/u, 125 MeV/u and 145 MeV/u He beams [27].

However a small energy range has been explored and therefore at present the only possibility is to rely on nuclear models, which however are not exact calculable theories and suffer from many uncertainties. The FOOT (FragmentatiOn Of Target) purpose is to experimentally measure nuclear fragmentation cross sections relevant in PT and space radioprotection in order to improve the algorithms currently used in the TPS adding the variable RBE models, to study the shielding material performances and to benchmark nuclear interaction models.
In the next chapter the FOOT experiment will be described in details.

# Chapter 2

# The FOOT experiment (FragmentatiOn Of Target)

The FragmentatiOn Of Target (FOOT) project is an applied nuclear physics experiment aiming to measure the fragmentation cross sections of relevance for PT and radioprotection in space applications. As seen in sec.1.4, accurate measurements of fragments production spectra are of great importance both to improve the TPS quality and to estimate the astronauts dose exposure in far from Earth missions in order to design proper shielding systems.
These measures will be used to implement a variable RBE in TPS, taking into account the target fragmentation and the related biological effects. The results of the FOOT project will be a reference point for the scientific and medical community, allowing a significant reduction in dose release to healthy organs near the cancer region and helping designing the shielding for future space missions. In the next sections the details of the FOOT experiment will be presented, giving special importance to the experimental requirements needed to measure the fragmentation cross sections.

## 2.1 Experimental requirements

The FOOT main goal is to measure the fragments production cross sections at energies that are relevant for PT and RPS applications. Since the most strict requirements come from PT, the accuracy of these measurements is dictated by the needs sets by PT radiobiologists. To improve the RBE evaluation it is essential to measure the fragments production cross sections with a relative uncertainty of the order of 5%. These measurements will be then implemented in the kernel of the codes used in treatment planning softwares. To this aim, since fragments charge and energy (and hence range) are the quantities that mostly affect fragments biological efficacy, the FOOT main goal is to perform the charge identification with an accuracy of $2-3\%$ and to measure the fragments kinetic energy spectra with an energy resolution about $1-2$ MeV/u. Also the mass has a significant role since it influences the fragments range, therefore the isotopic identification accuracy has to reach the accuracy level of about 5%. These requirements drove the development of the FOOT experimental setup.

## 2.2 Strategy for measurements of the target fragmentation in proton treatments

The FOOT experimental program initially foresees to measure the production yield and energy of fragments generated by proton and $^{12}C$ beams in the therapeutic energy range (energies of relevance for RPS applications will be explored afterwards with a re-optimized detector). Nuclear fragmentation channels will also be explored for $^{16}O$ and $^{4}He$ beams, which are increasingly considered in PT as promising alternatives to protons and carbon ions. Once the nuclear cross sections database will be sufficiently populated, it will be possible to benchmark and match the MC nuclear models with the experimental data. However, the main obstacle to perform measurements regarding the target fragmentation induced by a proton beam resides on the energies (and hence, range) involved in the target fragmentation processes.

### 2.2.1 Inverse kinematic approach

As reported in sec.1.2, due to kinematic reasons, target fragments originating from $p + X \rightarrow p' + X'$ reactions have a very low energy and short range. Considering a 180 MeV protons beam impinging on a water target, the fragments range is of the order of micrometers (see Tab.2.1).

| Fragment | E [MeV] | LET (keV/$\mu$m) | Range ($\mu$m) |
|---|---|---|---|
| $^{15}O$ | 1.0 | 983 | 2.3 |
| $^{15}N$ | 1.0 | 925 | 2.5 |
| $^{14}N$ | 2.0 | 1137 | 3.6 |
| $^{13}C$ | 3.0 | 951 | 5.4 |
| $^{12}C$ | 3.8 | 912 | 6.2 |
| $^{11}C$ | 4.6 | 878 | 7.0 |
| $^{10}B$ | 5.4 | 643 | 9.9 |
| $^{8}Be$ | 6.4 | 400 | 15.7 |
| $^{6}Li$ | 6.8 | 215 | 26.7 |
| $^{4}He$ | 6.0 | 77 | 48.5 |
| $^{3}He$ | 4.7 | 89 | 38.8 |
| $^{2}H$ | 2.5 | 14 | 68.9 |

**Table 2.1.** Expected average physical parameters (E, LET, Range) for fragments produced by a 180 MeV proton beam impinging a water target [28].

For this reason their experimental detection is extremely difficult: a fragment produced by a proton projectile, can leave the target and thus be detected only if it has been produced at a distance less than few micrometers form the exit surface of the target material. Otherwise the fragment deposits all its energy locally, being trapped inside the target and invalidating any detection attempt. Hence even with a relatively thin target ($\sim$ mm) the produced fragments will not be able to exit and reach a detector. On other hand, an even thinner target ($\sim \mu$m) implies mechanical problems since it is difficult to handle such a fragile target without risking any damage to it and most of all the interaction rate would be extremely reduced. To

overcome these issues, an *inverse kinematic* approach has been proposed to study the fragmentation process.
To use the inverse kinematics approach is necessary to apply the Lorentz transformation that allows to switch from the laboratory frame to the *patient frame*. Therefore instead of shooting a proton beam onto a tissue-like (carbon or oxygen) target, tissue-like nuclei will be accelerated to impinge on a proton target (see Fig.2.1). Fragments originated from a carbon or oxygen beam are emitted with higher energy and so a longer range, allowing an easier detection and event reconstruction. Also it becomes possible to use a thicker target with a consequent increase of the interaction rate.

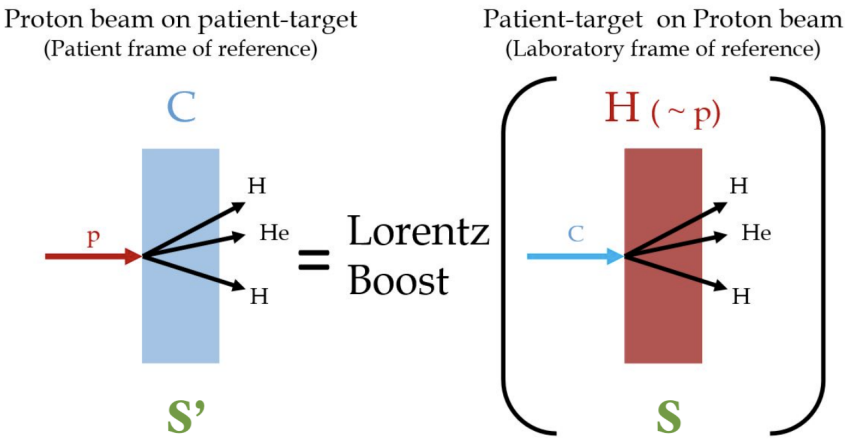


**Figure 2.1.** Scheme of the Lorentz transformation between the two reference frames.

If we consider $S$ as the laboratory frame in which the incident beam (composed by heavy charged ions) is moving along $z$ at a constant velocity $\beta$ and impinges in the stationary hydrogen target and S' the *patient frame* in which target and projectile material are switched, meaning that the beam is made of protons and the target is tissue-like, the proton 4-momentum components in the S' frame are given by:

$$P' = \Lambda P \tag{2.1}$$

where $P = (E/c, p)$ and $P' = (E/c, p')$ are the ions 4-momentum in S and S' respectively, while $\Lambda$ is a $4 \times 4$ matrix as follows:

$$\begin{bmatrix} E'/c \\ p'_x \\ p'_y \\ p'_z \end{bmatrix} = \begin{bmatrix} \gamma & 0 & 0 & -\beta\gamma \\ 0 & 1 & 0 & 0 \\ 0 & 0 & 1 & 0 \\ \beta\gamma & 0 & 0 & \gamma \end{bmatrix} \begin{bmatrix} E/c \\ p_x \\ p_y \\ p_z \end{bmatrix} = \begin{bmatrix} \gamma E/c - \beta\gamma p_z \\ p_x \\ p_y \\ -\beta\gamma E/c + p_z \end{bmatrix} \tag{2.2}$$

The inverse Lorentz transformation is:

$$P' = \Lambda^{-1} P \tag{2.3}$$

where:

$$\Lambda^{-1} = \begin{bmatrix} \gamma & 0 & 0 & \beta\gamma \\ 0 & 1 & 0 & 0 \\ 0 & 0 & 1 & 0 \\ -\beta\gamma & 0 & 0 & \gamma \end{bmatrix} \tag{2.4}$$

Even if the angular emission spectrum is not essential at least for what concerns proton interactions, because the target fragments have very short range and would deposit their energy locally, the inverse kinematic approach requires an emission angle measurements with a resolution of the order of few *mrad* in order to correctly apply the Lorentz boost. Therefore, both the projectile and fragments directions have to be measured accurately.

### 2.2.2 Target material

The targets composition has been set according to the human body composition, i.e. carbon, oxygen and hydrogen have been selected as the main targets of interest. As a pure gaseous hydrogen target would imply many technical difficulties, such as the low rate due to the low density, the measurements will be performed with two different targets: one made of carbon and the other made of an hydrogen enriched compound, i.e. polyethylene ($C_2H_4$). The hydrogen cross sections will be then extracted by the data obtained with the two targets.

$$\sigma(H) = \frac{1}{4}\Big(\sigma(C_2H_4) - 2\sigma(C))\Big) \tag{2.5}$$

The same procedure is also valid for differential cross sections:

$$\frac{d\sigma}{dE}(H) = \frac{1}{4}\left(\frac{d\sigma}{dE}(C_2H_4) - 2\frac{d\sigma}{dE}(C)\right) \tag{2.6}$$

$$\frac{d\sigma}{d\Omega}(H) = \frac{1}{4}\left(\frac{d\sigma}{d\Omega}(C_2H_4) - 2\frac{d\sigma}{d\Omega}(C)\right) \tag{2.7}$$

Doudouet *et al.* [29] at GANIL (France) have already validated the method used to combine the cross sections of composite targets to extract an elemental target, i.e. $CH_2$ and $C$ to extract $H$. Their result is shown in Fig.2.2. A disadvantage of this strategy, however, is that the resulting cross section uncertainties are the quadratic sum of the uncertainties of the two single targets, therefore the cross sections on hydrogen have a higher uncertainty.
The target thickness density should be of the order of $gcm^{-2}$ depending on the material used, in order to minimize the probability of secondary fragmentation within the target. A reasonable target thickness is $2 - 4$ cm, which is a good compromise between the interaction rate and the required angular resolution.

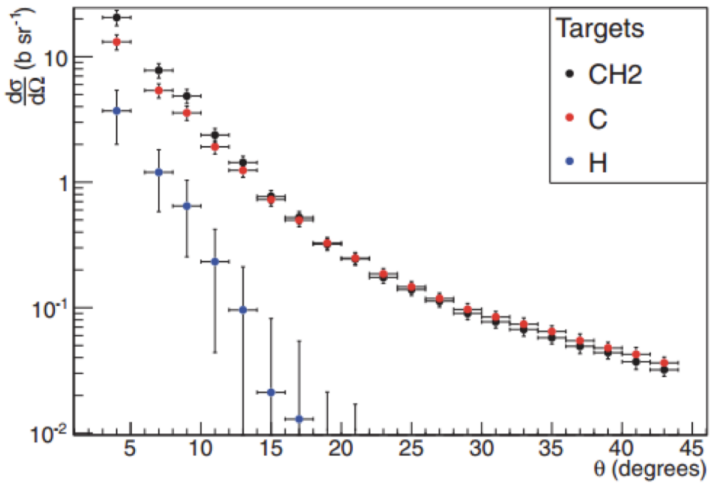


**Figure 2.2.** Combination of graphite and $CH_2$ targets angular distribution to determine the hydrogen angular distribution for $^2He$ fragments. The angular distribution for the hydrogen target is obtained as the difference between these[30].

## 2.3 Experimental setup

The first reactions, that will be investigated, are the following:

- $^{16}O +^{12} C$;
- $^{16}O +^{12} C_2H_4$;
- $^{12}C +^{12} C$;
- $^{12}C +^{12} C_2H_4$.

with beams of $100 - 400$ MeV/u energy. The fragments of interest for the FOOT experiment are those that could release relevant dose deposition outside the target region. Fig. 2.3 shows the angular and energy distribution, obtained from a Monte Carlo (MC) simulation, of the fragments produced by an oxygen ions beam at 200 MeV/u.
All the particles with $Z > 2$, interesting for their high RBE and low LET, are produced in the forward direction with $\theta < 10°$, instead helium ions and protons can be produced at $\theta \gg 10°$, where $\theta$ indicates the angle with respect to the incident beam direction. In the case of carbon incident beam a similar distribution is expected.

The FOOT project includes the development of two different experimental setup: an electronic detector setup to measure heavier fragments and an emulsion spectrometer for the lighter ones, which allows to extends the angular acceptance up to 70°. Both the experimental setups have been designed in order to be easily movable fitting the experimental room space limitations (usually located in treatment centers) and covering the fragments angular spread. The preferred sites for the data taking

are the experimental hall of the CNAO center in Pavia (Italy), the HIT center in Heidelberg (Germany) and the GSI in Darmstadt (Germany).

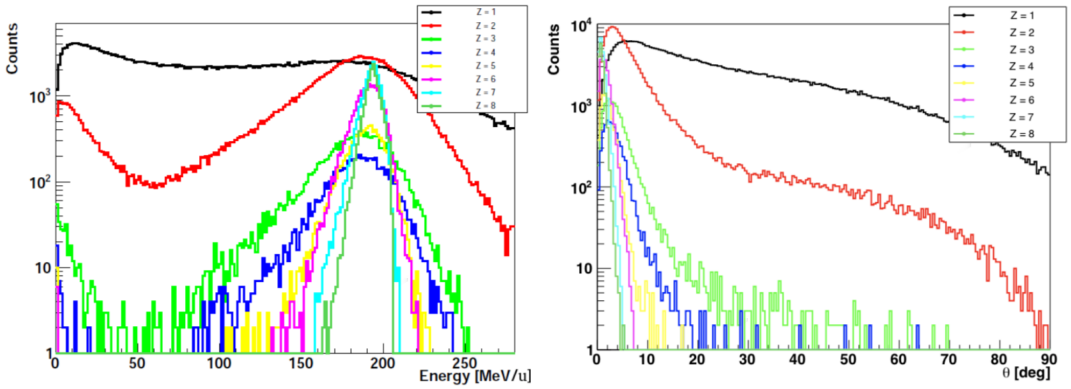


**Figure 2.3.** Emission angle distribution with respect to the beam direction (a) and energy distribution (b) for fragments produced by a $^{16}O$ beam with 200 MeV/n kinetic energy impinging on a 2 polyethylene target (results of a FLUKA simulation).

### 2.3.1 Detection of heavy ion particles

The experimental setup for the heavy particle measurements ($Z \geq 3$) is shown in Fig.2.4. The fragments mass identification is performed combining the measurements of the particles momentum, kinetic energy and Time Of Flight (TOF). The charge identification relies on the evaluation of the energy loss $\Delta$E and of the TOF, from which it is possible to obtain $\beta$, according to Eq.1.6. Further details about the mass and charge identification will be given in sec.2.4.
The setup size has been established as a compromise between the geometrical acceptance, the cost and the space available in the experimental areas of the selected facilities. Longitudinally, the whole setup can be contained in about $\sim$ 1.5m.

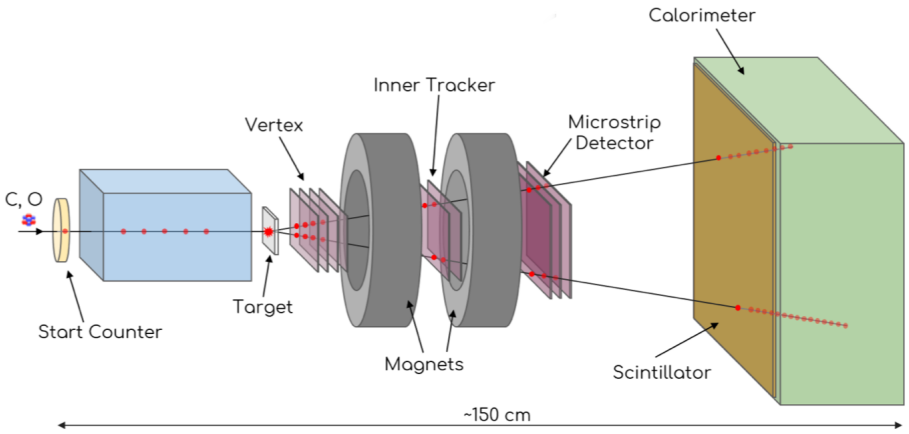


**Figure 2.4.** The FOOT experimental setup for the measurements of heavy ion fragments ($Z > 2$).

The setup includes several detectors that are explained in details in this section. Starting from the incident beam direction, three different regions can be identified in the setup: the **pre-target region**, the **magnetic spectrometer** and the **downstream region**.

**Pre-target region** The detectors in this region are designed to monitor the primary beam and are a plastic scintillator (Start Counter-SC) and a drift chamber (Beam Monitor-BM).

- **Start Counter**
  The SC is a thin plastic scintillator layer placed about 30 cm before the target that monitors the primary particles rate and gives the trigger signal for event acquisition, providing the number of primary particles and the start of the TOF. The SC is a foil of EJ-204 plastic with an active area of $5 \times 5$ cm$^2$ with a thickness ranging from 250 $\mu$m and 1 mm depending on the beam projectile energy and particle type. Since the measurement of the TOF is crucial to achieve the desired mass identification, the SC time resolution has to match the time resolution of the other scintillator detector (see par.2.3.1) that gives the end of the TOF. Therefore the SC aims for a time resolution of $60 - 70$ ps (see sec.4.2 for more details). Its properties are studied in details in this thesis.

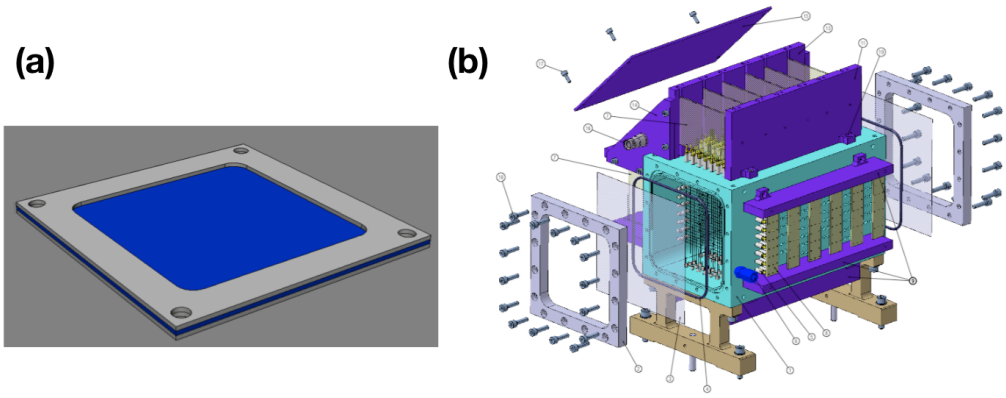


**Figure 2.5.** Technical drawing of the SC (a) and an exploded view of the BM (b) [28].

- **Beam Monitor**
  The BM is a drift chamber built for the FIRST experiment [31]. The total dimensions are 21 cm $\times$ 11 cm $\times$ 11 cm with the long side parallel to the beam direction ($z$) and placed between the SC and the target. It consists of twelve layers of wires, with three drift cells per layer. Planes with wires oriented along the $x$ and $y$ axes are alternated allowing the beam profile reconstruction. The BM is operated at the atmospheric pressure, at a working voltage of 1.8 kV when using an $Ar/CO_2$ (80/20) gas mixture. The BM efficiency was measured to be close to unity for carbon ions beam while the mean track spatial resolution was measured to be of the order of $\simeq 140\mu$m. The read-out

time is $\sim \mu$s [32][33].
The choice of a drift chamber detector relies on its low density material in order to minimize the Multiple Coulomb Scattering (MCS) and the production of fragments within the detector (pre-target fragmentation).
The BM purpose is to measure the beam direction, which is essential for the inverse kinematic approach in order to apply the correct Lorentz transformation, and reject the events in which the primary ion has fragmented before the target.

**Magnetic spectrometer** The magnetic spectrometer includes two pixel detectors, a microstrip detector and a permanent magnet system that provides the required magnetic field in order to measure the fragments momentum.

- **Permanent Magnet**
  The magnetic system is a key element of the FOOT spectrometer and it is used to bend the fragments produced in the target. The magnetic field will be provided by two permanent magnets in *Halbach* configuration (see Fig.2.6a): in each of them twelve blocks of magnets made of $Sm_2CO_{17}$ (Somarium-Cobalt) are arranged in an annular configuration. The material was chosen thanks to its low sensibility to radiation exposure compared to other magnets materials. In fact the magnets in the FOOT setup are exposed to various radiation, such as neutrons and light ions, that can degrade and damage the permanent magnets material, thus altering the produced field.
  The Halbach configuration produces an approximately uniform field in the internal hole (see Fig.2.6b).

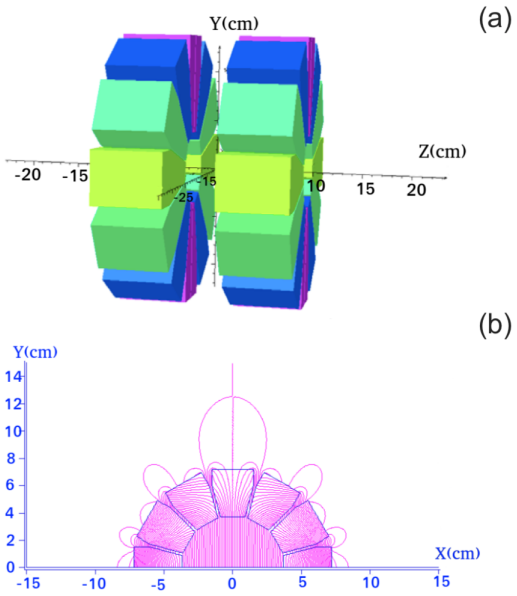


**Figure 2.6.** Design of the FOOT Permanent Magnet implementation using an Halbach geometry (left) and the relative magnetic field map (right) as obtained from a simulation[28].

Fig.2.7 shows in details the $B_y$ expected distribution as a function of $x$ and

$z$. In order to place an intermediated station (see Fig.2.4) to perform an additional momentum measurement the solution with two permanent magnets has been preferred to a single one. This geometry causes a double Gaussian trend (see Fig.2.7b) of the magnetic field along the $z$ axis.
When a particle crosses the magnets, the gained transverse momentum $\Delta p_T$ is given by:

$$\Delta p_T = q \int B dl \tag{2.8}$$

where $q$ is the particle charge and $B$ is the magnetic field intensity in correspondence of the $dl$ length element of the magnet. To improve the momentum resolution both $B$ and the total magnet length $L$ are crucial parameters: the Halbach configuration is characterized by a field intensity proportional to ratio between the external and internal radii, as follows:

$$B \propto ln\left(\frac{R_{out}}{R_{in}}\right) \tag{2.9}$$

At present, the permanent magnets are still being optimized. Using an internal and external radius equal to $\sim 4$ cm and $\sim 14$ cm respectively, the obtained B field has an expected intensity of the order of $0.8 - 0.9$ T that is compatible with the requirements sets for FOOT (details are given hereafter).

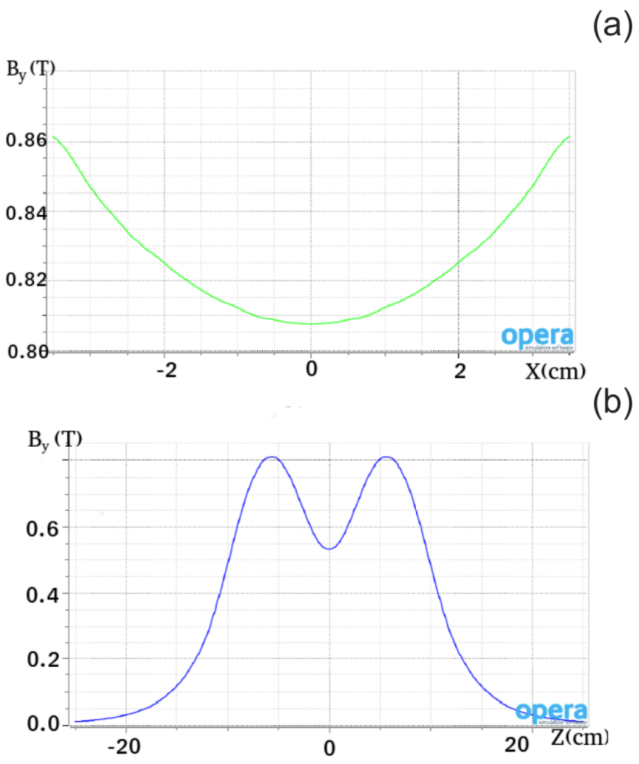


**Figure 2.7.** $B_y$ as a function of x at $y = 0$ and $z =$ center of one of the two permanent magnets (a) and as a function of z at $x = y = 0$ [28]. The figures have been obtained for two 7 cm long (z) permanent magnets of 10 cm blocks thickness.

- **Vertex detector**
  The Vertex detector (VTX) consists of four tracking layers of MIMOSA28 (M28) silicon chips (see Fig.2.8a) belonging to the family of the CMOS Monolithic Active Pixel Sensors (MAPS). Each sensor is a matrix of 928 rows × 960 (columns) pixels of 20.7 $\mu$m pitch, for a total sensitive area of 20.22 mm × 22.71 mm. Each M28 is 50 $\mu$m thick, resulting into an overall material budget for the entire vertex tracker of 200 $\mu$m. The VTX stack consists of two sub-stations with two sensor each: within the same sub-station the sensors are placed at a relative distance of 2 mm while the two sub-stations are separated by 10 mm due to the size of the electronic components on the readout boards. This detector is placed at a distance of $\sim$ 0.5 cm after the target (see Fig.2.8b). It contributes to the measurements of the particle momentum in the magnetic field providing the fragments direction when they exit the target and they change their path inside the magnetic field and evaluates the vertex position (the position inside the target where all the fragments are produced) for each event. The VTX has already been tested and used in the FIRST experiment [30]. The tracking efficiency was measured to be $\sim$ 95%, the measured cluster position resolution was better than 10 $\mu$m and the vertex spatial resolution was 10 $\mu$m in the plane orthogonal to the beam direction and 60 $\mu$m along the beam direction. The main drawback of such technology is the large readout time is of about 100 $\mu$s, leading to a low rate capability of few kHz.

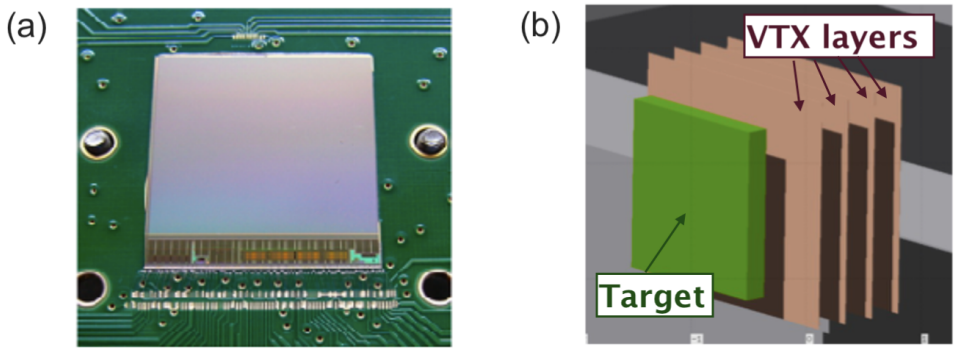


**Figure 2.8.** Picture of a M28 chip (a) and target and vertex tracker geometrical scheme (b) [28].

- **Inner Tracker**
  The FOOT Inner Tracking system is placed between the two permanent magnets, at a distance of $\sim$ 20 cm from the target (see Fig.2.4). It covers an area of about 8 cm × 8 cm according to the emission angle distribution that is broader here than in the VTX. The detector is composed by two planes of 16 M28 sensors. The detector structure is composed by ladders similar to the ones implemented in the PLUME project[34], where each ladder is composed by two modules of six M26 pixel sensors. In the FOOT setup, the six M26 are replaced by four M28 sensor per plane in each module. Fig.2.9 shows a schematic view of four of these ladders. In each module the four sensors are

glued and bonded on a Flexible Printed Cable (FPC) made of Kapton having two or three conductive planes and an overall thickness $\sim 100$ $\mu$m.

- **Microstrip Silicon Detector**
  The Microstrip Silicon Detector (MSD) is the final station of the magnetic spectrometer and consists of three microstrip layers, separated by 2 cm and placed beyond the permanent magnets at about 35 cm from the target. This detector gives information regarding the track position and measures also the fragments energy loss. Each layer covers a total area of 9 cm $\times$ 9 cm. In order to achieve a spatial resolution $< 35$ $\mu$m a strip pitch of 125 $\mu$m has been chosen.

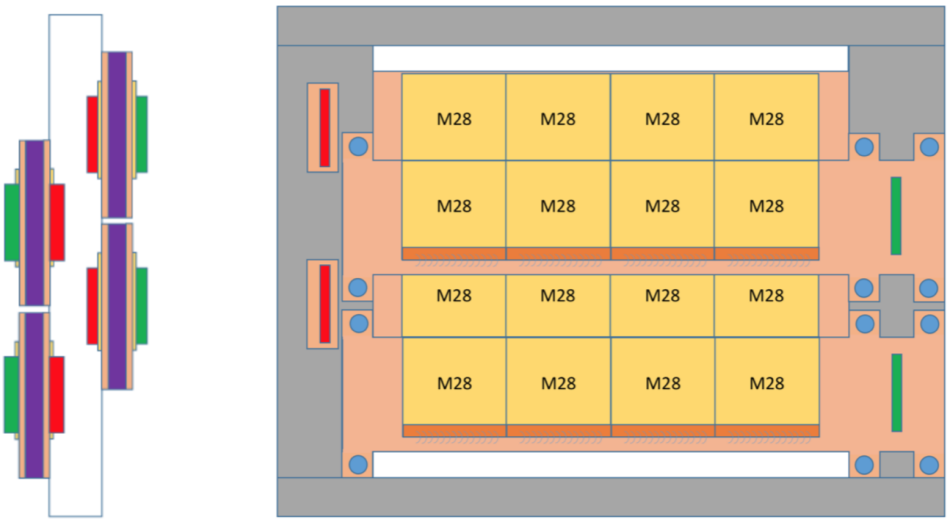


**Figure 2.9.** Schematic view of the Inner Tracker[28].

Depending on the beam energy, the detectors position, except the VTX one, will be different: at 200 MeV/u the inner tracker and permanent magnets system will be placed at $\sim 30$ cm from the target while the Microstrip Silicon Detectors at $\sim 60$ cm. At higher energy these distances will be increased in order to increase the magnetic region length and improve the momentum resolution. An overview of the pre-target and magnetic spectrometer regions is shown in Fig2.10, where is possible to observe the positioning mechanism of all the detectors including the target.

**Downstream region** The last part of the FOOT electronic setup is composed by a plastic scintillator wall ($\Delta$E-TOF detector) and a calorimeter.

- **$\Delta$E-TOF detector**
  The scintillator detector measures the fragments energy loss ($\Delta$E) and provides the stop of the time of flight measurements. Since the TOF is inversely proportional to its velocity $\beta$, it is possible to evaluate the fragments atomic number $Z$ from the Bethe-Bloch formula (Eq.1.6) using the $\Delta$E and $\beta$ measurements.

It is composed of two layers of 20 orthogonally oriented plastic scintillator bars, each one 3 mm thick, 2 cm large and 40 cm long, with a covered total area of 40 cm × 40 cm in order to match the fragments aperture at 1 m from the target. The energy resolution is estimated to be between 3 % and 5% while the time resolution is of the order of 40 ps. This detector is described in details in sec.4.3.

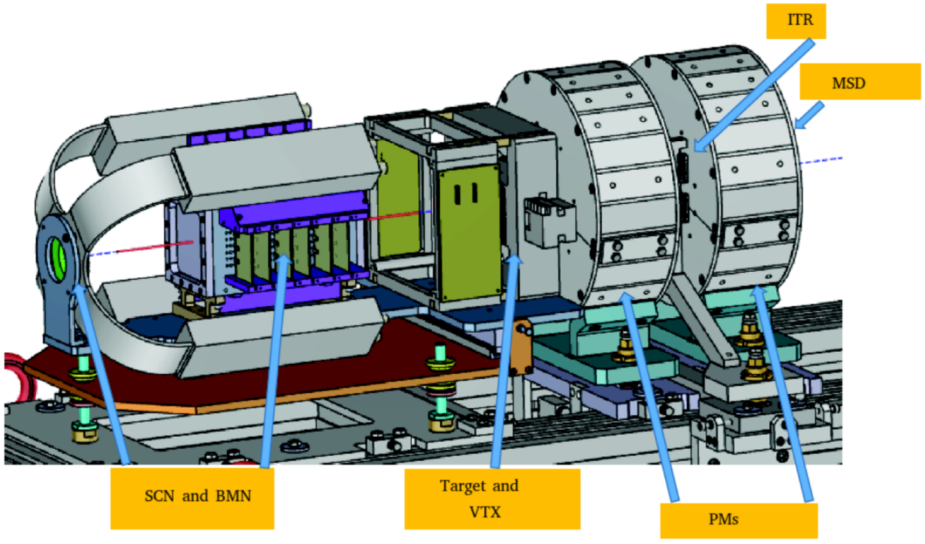


**Figure 2.10.** Technical drawing of the pre-target and magnetic spectrometer regions.

- **Calorimeter**

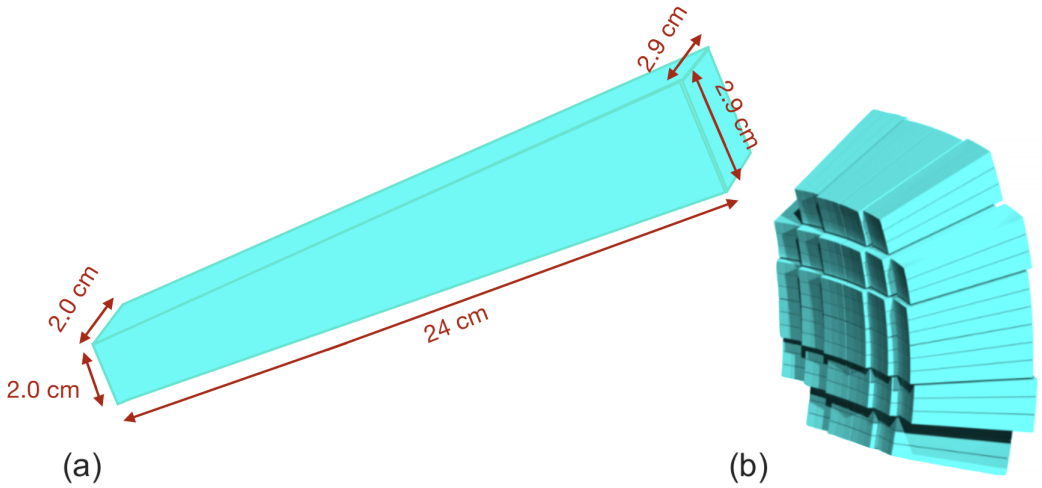


**Figure 2.11.** Schematic view of the BGO crystal (a) and of the fully assembled calorimeter detector (b).

The calorimeter (CALO) is composed by 288 BGO crystals with a truncated pyramid shape, chosen according to the fragments angular aperture, and a

length of 24 cm with a front and outer face area of about 2 cm × 2 cm and 3 cm × 3 cm, respectively (see Fig2.11a). These crystals are arranged in a pointing geometry (see Fig2.11b). The segmentation of the calorimeter is determined by the average angular separation of the traces and by the distance of the CALO from the target. In fact the fragments angular separation increases as the distance from the target increases. The segmentation (2 cm × 2 cm) is therefore chosen as a good trade-off between the cost and the fragment containment up to 400 MeV/u.
The crystals are then read-out by 8 mm × 8 mm Silicon PhotoMultipliers (SiPMs). The expected energy resolution ranges between $1-3\%$ depending on the fragment type and overall energy.

The distance of these two detectors with respect to the target position is different depending on the beam energy. As an example, at 200 and 400 MeV/u they will be placed at a distance of about 1 m and 2.9 m from the target, respectively. Therefore the downstream distance must be increased with increasing beam energy in order to improve the resolution on the fragments velocity ($\beta$).
These distances are compatible with the requirements sets by the experimental room where FOOT will be operated.

### 2.3.2 Detection of light charged particles

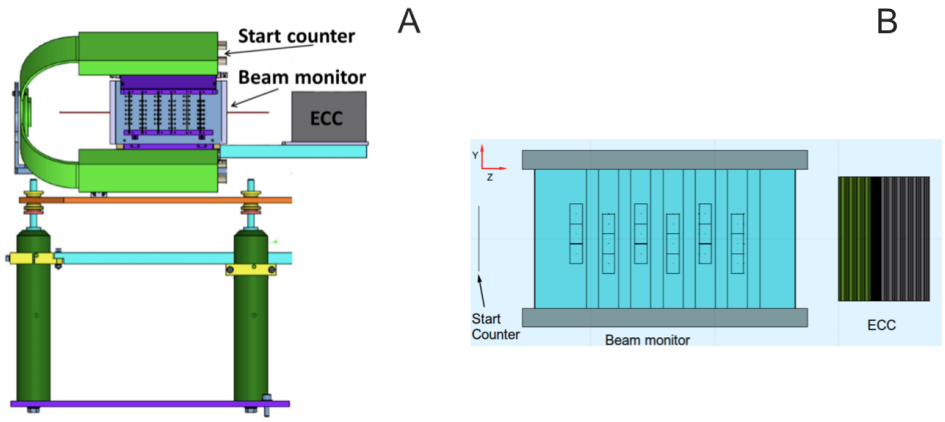


**Figure 2.12.** Emulsion spectrometer setup (A). Detailed $x-y$ schematic view of the same setup (B) [28].

To detect the low $Z$ (i.e. $Z \leq 3$ ) produced fragments, an Emulsion Cloud Chamber (ECC) detector [35], has been envisaged, since it extends the angular acceptance up to about 70°. The detector is placed, see Fig.2.12, after the SC and the BM, described above. This system integrates in a compact setup the target and the detector, providing a very accurate reconstruction of the interactions occurring inside the target with a high spatial ($\sim 0.06$ $\mu$m) and angular resolution (0.4-2 mrad). The emulsion films employed for FOOT are composed of 70 $\mu$m thick sensitive layers made of $AgBr$ crystals of 0.2 $\mu$m diameter scattered in a gelatin binder and placed on two sides of a 180 $\mu$m plastic base, with a total thickness of 320 $\mu$m and a

transversal area of 12 cm × 10 cm (see Fig.2.13 for emulsion details).
When a ionizing particle crosses a nuclear emulsion film. it produces a latent image which is turned into a sequence of silver grains after a process, named *development*. These sequence represents the particle track, then the fragments position and direction can be measured while the energy loss can be retrieved from the grain density[36].

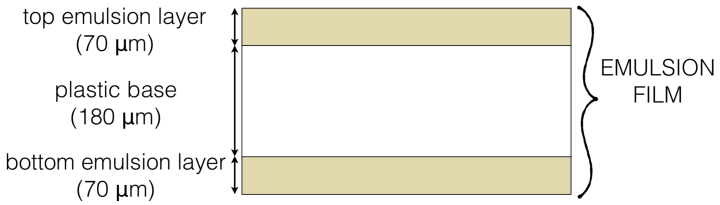


**Figure 2.13.** Schematic view of an emulsion film.

The ECC is composed of three sections: vertexing, tracking detector and ionization detector for momentum measurement and isotope identification (Fig.2.14 shows the emulsion spectrometer in details). The Emulsion Spectrometer (ES) first section is made of several elementary cells made of emulsion films interleaved with carbon or $C_2H_4$ layers. Each passive layer acts as target, while the emulsion reconstructs the vertex position. The thickness of the layers is defined by the interaction length, in order to obtain a sufficiently high number of interactions fully contained in the detector. The charge measurement region is composed by emulsion films, aiming to the atomic number identification for low charged fragments (proton, helium and lithium). In this case, the elementary cell is made of three emulsion films.

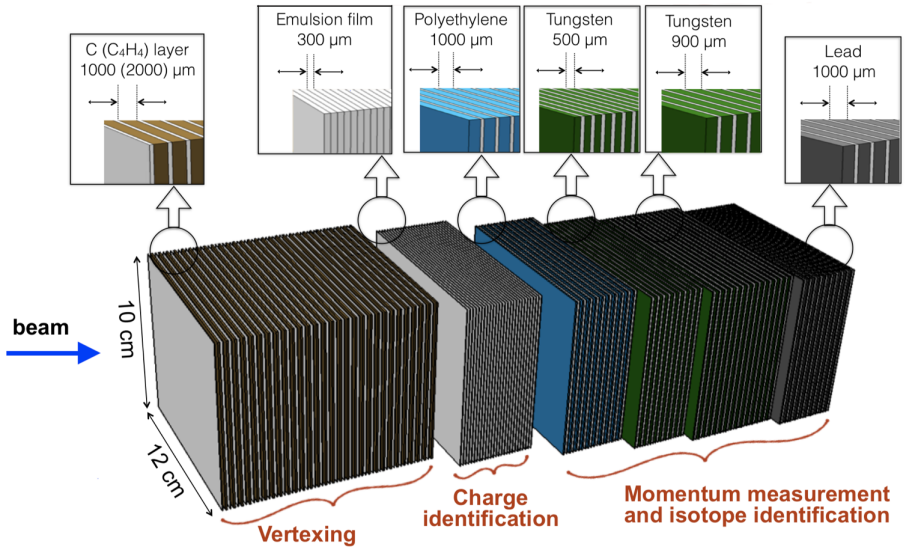


**Figure 2.14.** Scheme of the Emulsion Spectrometer (ES) composition for the FOOT experiment. The vertexing region consists on alternated layers of emulsions and target ($C$ and $C_2H_4$), the charge identification region is composed by only emulsion layers while the last region consists on alternated layers of emulsions and passive material, such as plastic, tungsten and lead.

The last region, dedicated to the momentum measurement, consists on several alternated emulsion films (300 $\mu$m thick) and absorber layers (1 mm of Pb). By measuring the entire particle track length, the kinetic energy is evaluated taking into account the correlation between range and momentum. The particles momentum can be estimated through the Multiple Coulomb Scattering (MCS) process:

$$p = \frac{13.6MeV}{\beta\delta\theta}\sqrt{\frac{x}{X_0}} \tag{2.10}$$

where $\delta\theta$ is the deviation of the track slope along its path. In this way is possible to measure independently the energy and momentum, allowing to evaluate the fragments mass number.

## 2.4 Fragments identification

The FOOT experiment has been designed to identify the fragments produced in inelastic interactions. To this aim, both the atomic $Z$ and mass $A$ number must be correctly determined. In particular the produced hydrogen, carbon or helium isotopes which, for a given kinetic energy per nucleon have different ranges, produce different biological damages. To properly account for the different fragments range and its impact on the radiation RBE it is essential to achieve a high accuracy on the isotopic identification and thus on the TOF, momentum and kinetic energy measurements.

### 2.4.1 Mass and mass number identification

To perform the fragments isotopic identification, goal of the FOOT experiment, the measurements of TOF, momentum and kinetic energy can be combined in three different ways. Obtaining three different estimates of the mass number ($A_1$, $A_2$ and $A_3$).

**Momentum and TOF measurements** The fragment mass $m$ is related to its momentum and velocity according to the following formula:

$$p = m\gamma\beta c = \frac{m\beta c}{\sqrt{1-\beta^2}} \rightarrow m = \frac{p\sqrt{1-\beta^2}}{\beta} \tag{2.11}$$

and then the mass number can be calculated as follows:

$$A_1 = \frac{m}{u} = \frac{1}{u}\frac{p}{\gamma\beta c} \tag{2.12}$$

where $u$ is the atomic mass unit equal to 931.494 $MeV/c^2$.
The $A$ resolution is then:

$$\sigma(A_1) = \sqrt{\left(\frac{\partial A_1}{\partial p}\sigma(p)\right)^2 + \left(\frac{\partial A_1}{\partial \beta}\frac{\partial \beta}{\partial TOF}\sigma(TOF)\right)^2} = \frac{1}{u}\frac{p}{\beta c}\sqrt{\frac{1}{\gamma^2}\left(\frac{\sigma(p)}{p}\right)^2 + \frac{\gamma^2}{\beta^2}\frac{L^2}{c^2 TOF^2}\sigma^2(TOF)} \tag{2.13}$$

As it can be concluded looking at Eq.2.13, the A uncertainty depends strongly on the resolution of the momentum and $\beta$, and therefore on the TOF measurements accuracy.

**TOF and kinetic energy measurements** Since the particle kinetic energy is equal to:

$$E_{kin} = (\gamma - 1)mc^2 \tag{2.14}$$

where $E_{kin}$ is the energy measured by the calorimeter, $A_2$ can be extracted as follows:

$$A_2 = \frac{m}{u} = \frac{1}{u}\frac{E_{kin}}{(\gamma - 1)c^2} \tag{2.15}$$

The related uncertainty is:

$$\sigma(A_2) = \sqrt{\left(\frac{\partial A_2}{\partial E_{kin}}\sigma(E_{kin})\right)^2 + \left(\frac{\partial A_2}{\partial \beta}\frac{\partial \beta}{\partial TOF}\sigma(TOF)\right)^2} = \tag{2.16}$$

$$\frac{1}{u}\frac{E_{kin}}{c}\frac{\gamma}{\gamma - 1}\sqrt{\frac{1}{\gamma^2}\left(\frac{\sigma(E_{kin})}{E_{kin}}\right)^2 + \frac{\beta^2\gamma^4}{(\gamma-1)^2}\frac{L^2}{c^2 TOF^2}\sigma^2(TOF)} \tag{2.17}$$

As in the case of $A_1$, one can conclude that the final attainable resolution depends on the resolution of the TOF and kinetic energy measurements.

**Momentum and kinetic energy measurements** The particle total energy can be defined by the sum of the kinetic and rest energies or by the energy momentum relation, from which we obtain:

$$E_{tot} = \sqrt{E_{kin}^2 + mc^2} = \sqrt{p^2c^2 + m^2c^4} = \tag{2.18}$$

Therefore the mass can be evaluated using Eq.2.18:

$$m = \frac{p^2c^2 - E_{kin}^2}{2c^2 E_{kin}} \tag{2.19}$$

while the mass number:

$$A_3 = \frac{1}{u}\frac{p^2c^2 - E_{kin}^2}{2c^2 E_{kin}} \tag{2.20}$$

The resolution on the mass number determination is then:

$$\sigma(A_3) = \sqrt{\left(\frac{\partial A_3}{\partial p}\sigma(p)\right)^2 + \left(\frac{\partial A_3}{\partial E_{kin}}\sigma(E_{kin})\right)^2} = \tag{2.21}$$

$$\frac{1}{u}\frac{1}{E_{kin}}\sqrt{p^4\left(\frac{\sigma(p)}{p}\right)^2 + \frac{(p^2c^2 + E_{kin}^2)}{4c^4}\left(\frac{\sigma(E_{kin})}{E_{kin}}\right)^2} \tag{2.22}$$

As in the case of $A_1$ and $A_2$ a dependence on the momentum and kinetic energy is observed.

The required precision on the mass measurements, coming from the requirements posed by PT applications, is $\frac{\sigma(A)}{A} \sim 5\%$, which can be accomplished if TOF, momentum and energy measurements resolutions are the ones already reported in sec.2.1: 100 ns, 2-3 % and 1-2% respectively.

### 2.4.2 Energy loss

The released energy is evaluated as the sum of the energy deposited by the same particle in the microstrip detector (MSD) ($\Delta E_{MSD}$) and in the FOOT scintillator ($\Delta E_{tw}$), as follows:

$$\Delta E = \Delta E_{MSD} + \Delta E_{tw} \tag{2.23}$$

and since the MSD resolution is defined mainly by the stochastic nature of the energy loss process and is hence much larger when compared to the one that can be obtained on the TW, the $\sigma(\Delta E)$ is given by:

$$\sigma(\Delta E) = \sigma(\Delta E_{tw}) \tag{2.24}$$

and its value is within the range 3-10 % depending on the fragment type and energy.

### 2.4.3 Particle energy measurement

The particle kinetic energy is measured by the calorimeter at the end of the beam line. The energy resolution for electromagnetic calorimeters can be expressed by the following formula[37]:

$$\frac{\sigma(E_{cal})}{E_{cal}} = \frac{a}{\sqrt{E}} \oplus \frac{b}{E} \oplus c \tag{2.25}$$

where $\oplus$ indicates a quadratic sum. The first term on the right-hand side is called *stochastic term* and includes the statistical fluctuations of the energy released by an incident particle. The second term is the *noise term* while the third one is the *constant term*, that arises from the calibration uncertainties. The relative importance of the various terms depends on the energy of the incident particle. The aimed energy resolution goal for the FOOT is of the order of 2%-3% for a particle kinetic energy equal to 200 MeV/n.

### 2.4.4 Particle momentum measurement

The fragments momentum is derived from the particle deflection inside the magnetic field or from the MCS scattering in the matter if the electronic or the ECC experimental setup is considered, respectively.
In general due to the Lorentz force a charged particle inside the magnetic filed has a circular orbit of curvature radius $\rho$ (see Fig.2.15a) in a homogeneous magnetic field $B$ (generated by a $L$ long magnet), which depends on the particle momentum $p$ as follows:

$$\rho = \frac{p}{qB} \tag{2.26}$$

where $q$ is the particle charge. Since $\rho >> L$ the deflection angle $\theta$ can be approximated to $\frac{L}{\rho}$ and thus, assuming $B = (0, B_y, 0)$, the particle momentum is:

$$p = \frac{L}{\theta} q B_y \tag{2.27}$$

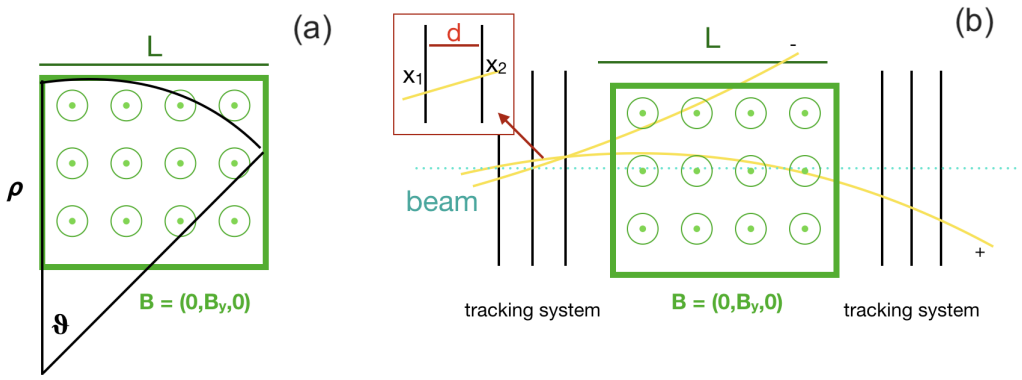


**Figure 2.15.** Track deflection of a charged particle in a magnetic spectrometer (a) and particle momentum evaluation scheme (b) where the red box shows a magnification of the incident angle measurement strategy.

Thanks to the tracking system (see Fig.2.15b) it is possible to evaluate the particle momentum, measuring its direction before ($\theta_{in}$) and after ($\theta_{out}$) the magnetic field. Then the particle momentum can be computed using:

$$p = \frac{qLB_y}{(\theta_{out} - \theta_{in})} \tag{2.28}$$

Since the deflection angle is measured by the tracking system (see Fig.2.15):

$$tg\theta \simeq \theta = \frac{x_2 - x_1}{d} \tag{2.29}$$

where $d$ is the distance between the tracking planes, the momentum resolution can be computed as:

$$\frac{\sigma(p)}{p} = \frac{2\sigma(x)}{d}\frac{p}{qBL} \tag{2.30}$$

where $\sigma(x)$ is the tracking system position resolution. In the FOOT electronic setup the detectors are located in such a way to estimate the particle position before, in the middle and after the permanent magnets. Then using GENFIT [38], it is possible to reconstruct the particle track and so measure the particle momentum. The expected momentum resolution for the FOOT experiment is at the level of 5% for a particle energy of 200 MeV/n.

When using the ECC setup, as seen in Eq.2.10, the particle momentum is evaluated from its multiple Coulomb scattering inside the emulsions. Also in this case the expected momentum resolution is of the order of 5%.

### 2.4.5 Time Of Flight and $\beta$ measurements

The fragments time of flight measurement is performed by subtracting the start time $t_{sc}$ measured by the SC, to the stop time $t_{tw}$ measured by the ΔE-TOF detector. The resulting time, however, includes also the time ($t_{offset}$) taken by the primary beam to travel from the SC to the target, that has to be subtracted as well. The

$t_{offset}$ is easily calculable since the kinetic energy and target-SC distance are known *a priori*. Therefore the TOF is evaluated as follows (see Fig.2.16):

$$TOF = t_{tw} - t_{sc} - t_{offset} \tag{2.31}$$

In general the time resolution, studied in details in this thesis (see ch.4), scales with the inverse of the energy released in the SC or ΔE-TOF detectors, and thus it gets worse as the particle kinetic energy increases (see Eq.1.6):

$$\frac{dE}{dx} \propto \frac{1}{\beta^2} \propto \frac{1}{E_{kin}} \rightarrow \frac{\sigma(t)}{t} \propto \frac{1}{\sqrt{\Delta E}} \propto \sqrt{E_{kin}} \tag{2.32}$$

where $\Delta E$ is the energy released in the detector.

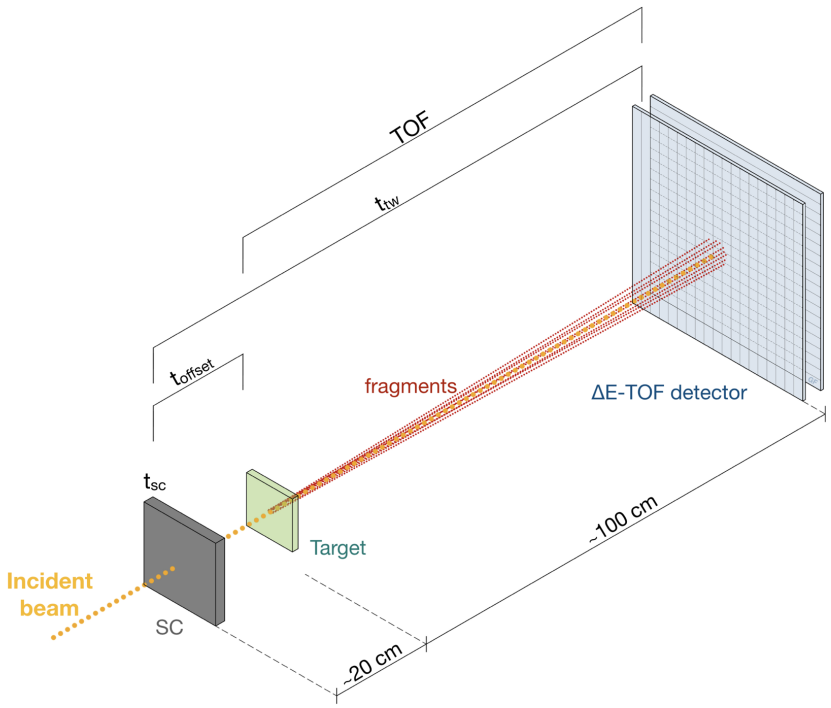


**Figure 2.16.** Schematic view of the fragments TOF measurement. For simplicity, the detectors not included in the measurement are not represented.

Since the resolution on the offset that has to be subtracted $\sigma(t_{offset})$ is ∼O(ps), well below the ones coming from the SC and $\Delta E$-TOF detector, it can be neglected and so the final resolution on the time of flight measurement is computed as follows:

$$\sigma(TOF) = \sqrt{\sigma(t_{sc})^2 + \sigma(t_{tw})^2} \tag{2.33}$$

In order to match the requirements on the cross section measurements and isotope identification, the TOF measurement needs to be performed with an overall resolution of 100 ps or less. The SC detector needs hence to achieve a 70 ps resolution on the incoming ions (at all the different energies). The TW, in a similar way, needs to measure the fragments crossing time with resolution $\sim 30 - 40$ ps for all the different fragments at different energies. The preliminary results obtained from the data samples with $^{12}C$ and $^{16}O$ ions beam are reported in chapter 4.

The particle velocity $\beta$, can be obtained from the TOF measurement as follows:

$$\beta = \frac{L}{TOF \times c} \tag{2.34}$$

where L is the total distance traveled by the particle form the production point to the entrance face of the $\Delta E$-TOF detector.
Due to both magnetic field and MCS the particle trajectory is not a straight line, therefore at the moment $L$ is approximate as the sum of several consecutive segments. Assuming that the $\sigma(L)$ is negligible with respect to the other quantities, the $\sigma(\beta)$ can be expressed as:

$$\sigma(\beta) = \frac{\partial \beta}{\partial TOF}\sigma(TOF) = -\frac{1}{c}\frac{L}{TOF^2}\sigma(TOF) \tag{2.35}$$

### 2.4.6 Charge identification

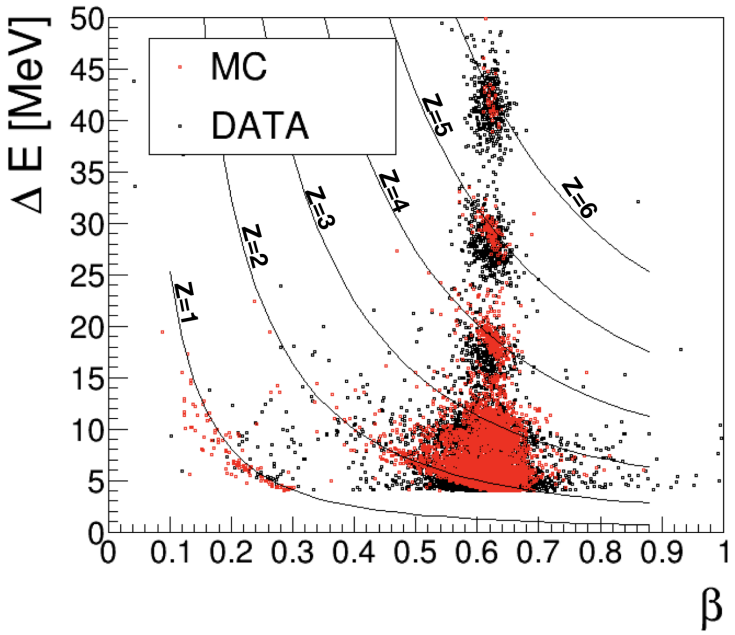


**Figure 2.17.** Fragments Z identification when a $^{12}C$ ions beam of 280 MeV/u impinges on the TW system. The experimental data (black) are compared to the simulated ones (MC, red).

As already said in sec.2.3.1, the charge is evaluated using both the $\Delta E$ and the TOF measurements. In fact these two quantities are related to the particle charge according to the Bethe-Block equation (see Eq.1.6).
In the electronic setup case , the energy loss per unit path length can be obtained form the ratio between the $\Delta$E and the total thickness of the three MSD planes and the $\Delta E$-$TOF$ detector while $\beta$ is extracted from the TOF value (see sec.2.4.5) Therefore the fragment $Z$ value can be retrieve by inverting the Eq.1.6, with a resolution of the order of 2-3%. Figs.2.17 shows the fragments charge identification according to the relation between the energy released and the particles velocity ($\beta$).

# Chapter 3

# Simulation and Reconstruction tools

The software developed for the FOOT experiment called SHOE (Software for Hadrontherapy Optimization Experiment), is organized as a toolkit. In my thesis project I have mainly contributed to the development of the simulation and data reconstruction tools while trying to understand if the technologies proposed for FOOT experiment were adequate, and then checking on data samples if the simulation estimates were correct. In fact even if the nuclear interaction models included in simulation software do not match the accuracy required by the radiobiologists, MC simulations have been used to design the FOOT experimental setup and investigate the expected performances of the full reconstruction chain (reported in sec.2.4). The FOOT simulation has been built in the framework of the FLUKA Monte Carlo (MC) software[39][40][41]. FLUKA is a general purpose tool for calculations of particle transport and interactions with matter, covering an extended range of applications such as proton ad electron accelerator shielding, dosimetry, cosmic rays and radiotherapy. The simulation framework provides the tools to simulate the beam interactions with the detectors and allows to study how the expected performances of the individual detectors determine the final precision of the measured double differential sections.
Taking into account the MC information, the track reconstruction is performed by means of a Kalman filter algorithm implemented in GENFIT which takes into account magnetic fields and Multiple Coulomb Scattering inside crossed materials[42]. The reconstruction tools are used to combine the different sub-detectors information aiming at the complete event reconstruction and in particular at the cross-section measurements.
A general introduction of FLUKA will be given in the next section, followed by a summary of the nuclear models included in the simulation. In the last section the details about the FOOT simulation will be discussed.

## 3.1 FLUKA Monte Carlo simulation code

The FLUKA code, developed from the collaboration of INFN and CERN, provides the software tools to simulate the interaction and transport of hadrons, heavy ions

and electromagnetic particles in the energy range from keV to TeV. Therefore FLUKA can be used in a wide range of applications, from high energy experimental physics to cosmic rays studies and medical physics. The consistency among all the reaction steps and reaction type is always ensured, conservation laws are enforced at each step and the results are checked against experimental data at single interaction level. As a result, final predictions are obtained with a minimal set of free parameters fixed for all energy, target and projectile combinations. FLUKA physical models are integrated in the code and not modifiable but a set of user interface routines (written in Fortran 77) can bu used to customize the software.
To run the simulation the user must provide the definition of all the information necessary to the software for the data processing, which have to be included in input and geometry files. The main FLUKA inputs, which are called *cards*, are the following:

- GEOMETRY: define the geometry, which is made of bodies and regions. The regions are uniform objects formed by the boolean combination of many bodies, which are geometrical objects;
- MATERIAL: define the materials and their assignment to the different regions;
- PHYSICAL OPTIONS: selects predefined physics settings, i.e. production and transport energy cutoffs or $\delta$ rays production thresholds;
- BEAM and BEAMPOS: define the beam characteristics and beam position and direction;
- RANDOMIZ, START and STOP: initialize the seed for the generation of random numbers and the number of primaries, and declares the end of the program.

The MC code handles the transport of all primary and secondary particles throughout the experimental volume and scores the quantities of interest. Fig.3.1 shows a schematic view of the data simulation process. The simulation of each detector response is stored in a ROOT file[43], then the data analysis is performed.

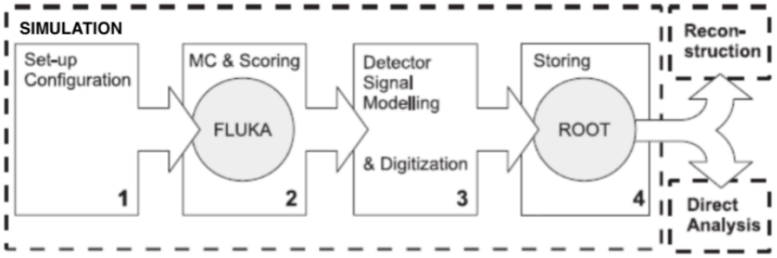


**Figure 3.1.** Data simulation process.

For a better management of the different cards, the FLuka Advanced InteRaface (FLAIR) can be used, which is an all-in-one user friendly graphical interface. FLAIR is endowed with a fully featured input file editor, and it allows interactive visualization

of the geometry as well as the compilation, running and plotting results. A 3D rendering of the FOOT apparatus made by FLAIR is shown in Fig.3.2.

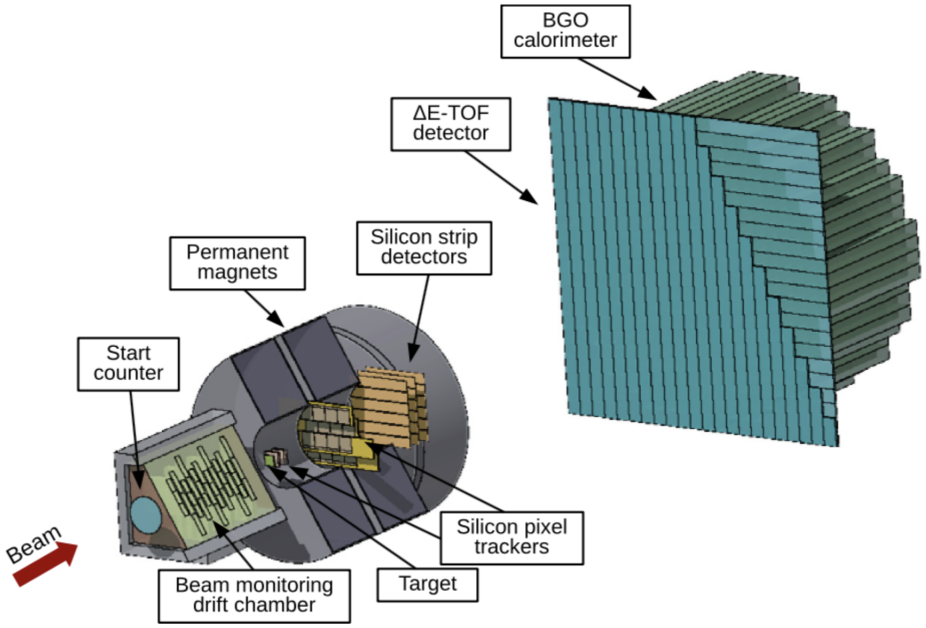


**Figure 3.2.** 3D rendering of the FOOT apparatus.

To simulate particle interactions with the various materials, FLUKA makes use of experimental cross sections, if available, otherwise different theoretical models are employed, according to the interacting particle type and energy.
The agreement between the experimental data and the FLUKA nuclear fragmentation models is reasonable but not sufficient for medical applications. As reported in sec. 1.4, to improve the data-MC agreement and thus to achieve the required PT accuracy, the double differential cross sections measurements, missing at present, are crucial. However the models already implemented are appropriate to stimulate the FOOT expected performance and to optimize the experimental apparatus.
The hadron-nucleus and nucleus-nucleus models managed by FLUKA are described in the next sections.

### 3.1.1 Hadron-nucleus model

The general scheme adopted for the simulation of hadron-nucleus interactions in FLUKA can be described by PEANUT (Pre-Equilibrium Approach to NUclear Thermalisation) model, which consists on the following steps:

- Glabuer-Gribov cascade [44] [45] for energy $> 5$ GeV, or Generalized Intra-Nuclear Cascade (GINC) for lower energy.
- Pre-equilibrium.
- Evaporation/Fragmentation/Fission and final de-excitation processes.

The first step (*abrasion* process, see sec.1.2) describes the interaction between two systems in terms of nucleons interaction with two different method depending on

the energy. As an example, the Glauber formalism provides a powerful method to derive elastic, quasi-elastic and absorption hadron (H)-nucleus (N) cross sections from the free H-nucleon cross sections. The inelastic interactions are evaluated as multiple collisions of the projectile with $n$ target nucleons.
At the end of the reaction chain, the nucleus is a thermally equilibrated system, characterized by its excitation energy. This system can "evaporate" nucleons, or fragments, or $\gamma$ rays, or even fission, to dissipate the residual excitation energy (*ablation* process, see sec.1.2). The Evaporation/Fragmentation/Fission process continues until the nuclear excitation energy becomes smaller then all the separation energies for nucleons and fragments, and generally leaves the residual nucleus in an excited state.

### 3.1.2 Nucleus-nucleus model

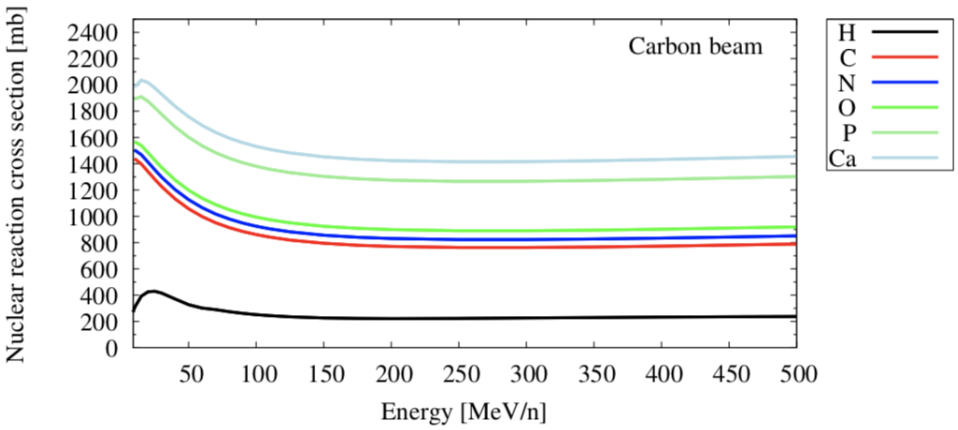


**Figure 3.3.** Reaction cross section of carbon ions at therapeutic energies as predicted by FLUKA for the most frequent elements present in the human body[46].

For the description of nucleus-nucleus interactions, that are extremely important in the PT field, the last two stages reported in sec. 3.1.1 for hadron-nucleon interaction, are essentially the same. Instead, for the initial cascade stage the nucleus-nucleus reactions are simulated with two main methods, depending on the energy range[47]. The relativistic Quantum Molecular Dynamics (rQMD) [48] [49] approach is applied in FLUKA for projectile energies in the range from about 100 MeV/n to 5 GeV/n. The rQDM model describes the interaction of two nuclei starting from their initial state described as a Fermi gas, following the propagation of each nucleon in the potential generated by all others nucleons and described according to a quantum mechanical formalism. The dynamical evolution of particles, the formation of heavy and light fragments and secondary nucleons is then predicted.
At lower energies, FLUKA uses a model based on the Boltzmann Master Equation (BME) [50] [46] theory. The BME model describes the de-excitation evolution of the system composed by two interacting nuclei during the pre-equilibrium phase. By solving a set of time-dependent transport equations, the model describes the evolution towards an equilibrium state through a sequence of two body reactions and ejection of unbound particles, whose multiplicity can be calculated.

The inelastic interaction probability for nucleus-nucleus interaction is given by the total reaction cross section $\sigma_R$. FLUKA uses the $\sigma_R$ value in addition to the particle decay time for the determination of the mean free path of a transported particle: the next collision point is chosen using the reaction cross section calculation. For energy below a few GeV down to the Coulomb barrier, FLUKA uses a parametrization of $\sigma_R$ based on the Trapathi semi-empirical model [51][52][53] while for higher energies the Glauber model predictions is used. As an example, Fig.3.3 shows the predicted nuclear reaction cross section of carbon ions for the most frequent elements present in the human body as a function of the energy. Fig.3.3 shows a strong dependence on energy at energies lower than 20 MeV/n while at energies grater than $100 - 500$ MeV/n a constant behavior is observed.

## 3.2 Implementation of FOOT simulation in FLUKA

The MC simulations produced using the FLUKA code have been used to design the whole FOOT electronic setup aiming to enhance the fragments reconstruction performances. Fig.3.4 shows the geometry of the experimental setup described in sec.2.3.1, implemented in FLUKA.

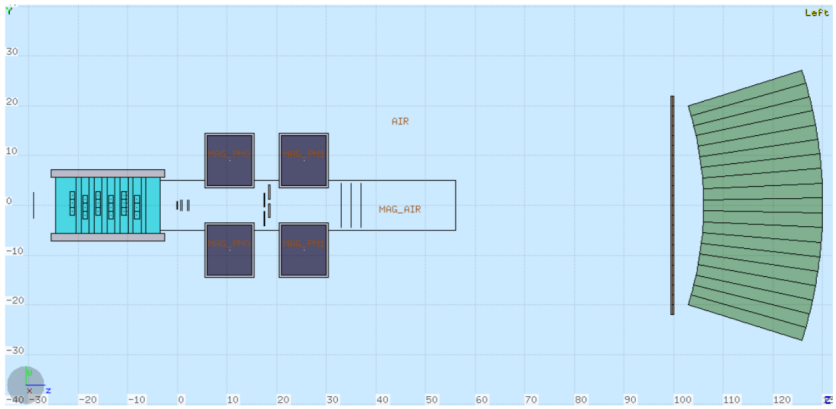


**Figure 3.4.** 2D view of the simulated FOOT geometry.

The origin of the reference frame coincides with the center of the target and the particle beam travels along the z-axis. Moving from right to left, the SC has been simulated as a plastic scintillator cylinder with a thickness of 250 $\mu$m, the BM has been implemented as a parallelepiped filled with gas and surrounded by an aluminum box with mylar entrance and exit windows along the beam direction and the target is a simple parallelepiped made of carbon or polyethylene. Then the four VTX planes, as well as the four ITR ladders, have been simulated according to the Mimosa-28 chips design [28]. The two permanent magnets have been simulated as annular magnets surrounded by an aluminum case while the MSD detector planes as simple silicon parallelepipeds. Finally, each $\Delta$E-TOF detector bar and calorimeter crystal has been simulated as parallelepiped or truncated pyramid respectively.
This simulated setup has been used to investigate the achievable detector accuracies, as already anticipated in sec.2.4, using a different combination of beam energies and target materials. The resolutions obtained as reported in sec.2.4, are summarized in Tab.3.1. The obtained values are already including the effect of some reasonable

safety factors introduced to take into account the over estimation of the detector performance or incomplete description of the detector response in terms of noise, cross talk and other possible defects. With the obtained values an estimate of the mass number relative uncertainty was possible. A value of $\sigma(A)/A \simeq 5\%$ has been obtained, fully matching the requirements set for proton therapy applications.

| | |
|---|---|
| $\sigma(E)/E$ | 2-3 % |
| $\sigma(p)/p$ | 5 % |
| $\sigma(TOF)$ | 100 ns |
| $\sigma(Z)/Z$ | 2-3 % |
| $\sigma(\Delta E)/\Delta E$ | 3-10 % |

**Table 3.1.** Expected resolution values for the particles kinetic energy (E), momentum (p), time of flight (TOF), atomic number (Z) and energy loss ($\Delta E$) obtained from MC simulations.

# Chapter 4

# Time Of Flight detectors

At the energy range of interest for PT applications explored by the FOOT collaboration, it is essential to maximize the time resolution since the energy and momentum ones are limited by the experiment dimension (*table-top*). Therefore a crucial role in minimizing the uncertainty on the isotope mass number determination is played by the fragments Time Of Flight (see sec.2.4.1). In particular the fragments mass has a significant role since it influences their range: when incident proton beams undergo fragmentation, they produce hydrogen, carbon or helium isotopes which, for a given kinetic energy per nucleon, have different ranges and so they produce different biological damages. To properly account for the different fragments range and its impact on the radiation RBE it is essential to achieve a high accuracy on the isotopic identification and thus on the TOF, momentum and kinetic energy measurements.
As already anticipated the measurement of the TOF drives the resolution on $A$ (sec.2.4.1) and hence was the subject of several optimization studies concerning the technology to be adopted. Finally, in FOOT, the choice was to perform the measurement using two distinct detectors: the Start Counter (SC) placed at $20 - 30$ cm upstream of the target, and the scintillator wall (TW) placed at $\sim 100$ cm downstream.
As discussed in chapter 2, in the FOOT apparatus the SC and the $\Delta E$-TOF detectors are both plastic scintillators and are read by silicon photomultipliers (SiPM). Plastic scintillators are particularly advantageous because they are fast, can be easily shaped based on custom requirements and have long attenuation length. They are appropriate for charged particle detectors because they are capable to reveal minimum-ionizing-like particles with a few mm thick detectors. SiPMs are smaller than conventional photomultiplier tubes, thus being more suitable for the coupling to thin bars, and the combination of plastic scintillator bars to SiPMs is also cost-effective.

In this chapter the main organic scintillator characteristics and principles of operation are reported. Then the SC and the FOOT scintillator wall are presented in details.

## 4.1 Principles of operation of the organic scintillators

The detection of ionizing radiation using the scintillation light produced in certain material is a long-standing technique in particle physics that has known a lot of applications and continuous and extensive studies. The scintillators consist of a material that is capable of emitting pulses of light (visible or ultraviolet, $\lambda \sim$ 350-700 nm) generated by the the intreraction with the incoming radiation.
When coupled to a photodetection device, the scintillation signal can be converted into electrical pulses which can be analyzed to give information concerning the incident radiation. In general, a scintillation material should ideally possess the following properties:

- It should convert the kinetic energy of charged particles into detectable light with a high scintillation efficiency (ideally equal to 1);
- This conversion should be linear, i.e. the light yield should be proportional to deposited energy over the wider possible range;
- A good light collection and hence a high transparency to the emitted light;
- The decay time of the induced luminescence should be short;
- The index of refraction should be near that of the glass ($\sim$ 1.5) to permit efficient coupling of the scintillation light to a photomultiplier tube.

No material can meet simultaneously all these requirements and for this reason a careful study of the best material is performed in order to find a good compromise of the different requirements as a function of the final measurement that has to be done.
The scintillating materials can be divided in two main classes: organic and inorganic. The inorganic ones have the best light output and linearity, but in general have a very slow response time. Instead organic scintillators are faster but characterized by a smaller light yield. The scintillator choice depends on the final application, i.e. gamma rays spectroscopy and beta spectroscopy or fast neutron detection are studied with inorganic (high density and high Z value) and organic (due to their hydrogen content) scintillators respectively.
For the organic scintillator specific characteristics see [54].

## 4.2 SC detector

The *start* of the TOF measurement is performed by a thin scintillator that provides the trigger signal to the whole experiment and the measurement of incoming ion flux to be used for the cross section measurement.
As FOOT aims to characterize the fragmentation that occurs in polyethylene and graphite targets, the detectors that are placed upstream with respect to the target must be as thin as possible in order to avoid a large and unwanted out of target fragmentation that could lead to a significant systematic uncertainty on the final cross section measurement. For this reason the SC thickness was carefully optimized looking for a good compromise between the out of target fragmentation probability,

that called for the smallest possible thickness, and the time resolution, that is directly linked to the light yield requiring a thick detector. A TOF resolution below 100 ps is needed to allow the proper separation of fragments with high mass number. Since the $\sigma^2_{TOF} = \sigma^2_{T_{tw}} + \sigma^2_{T_{sc}}$, a reasonable goal for the SC time resolution is 70 ps. In addition, the SC needs to be operated in a relatively low rate environment (incoming beam rate $\sim$ 10 kHz) allowing to measure with high precision the number of incoming ions.
The final detector layout, that was optimized using MC simulations, foresees a squared $EJ-204$ plastic scintillator ($5 \times 5$ cm$^2$ active area) arranged in a set of four different thickness (ranging from 250 $\mu$m to 1 mm) used depending on the beam projectile and energy range. The scintillator holder is made out of two 1 mm thick transparent 3D printed clear photopolymer. The $EJ-204$ is characterized by a rise time of $\sim$ 700 ps with a light yield of 10k photons per released MeV of energy. The scintillator counter is held by means of an aluminum cage enclosed in a black 2D printed box to provide the light tightness needed for the detector operation. The black box has two thin (4 $\mu$m) aluminized mylar windows, made by two 57 EJ-5902 layers each. Fig.4.1 shows the SC schematic view.
According to this geometrical proprieties the expected beam fragmentation inside the SC is about 5% of the incident ions.
The plastic scintillator readout is performed by means of $3 \times 3$ mm$^2$ Hamamatsu MPPCs (Multi-Pixel Photon Counters) SiPMs (in total 12 SiPMs for each readout side of the squared detector). The readout and powering of the SiPMs is handled by the WaveDREAM board, described in sec.4.4, and will be performed using 8 board channels.

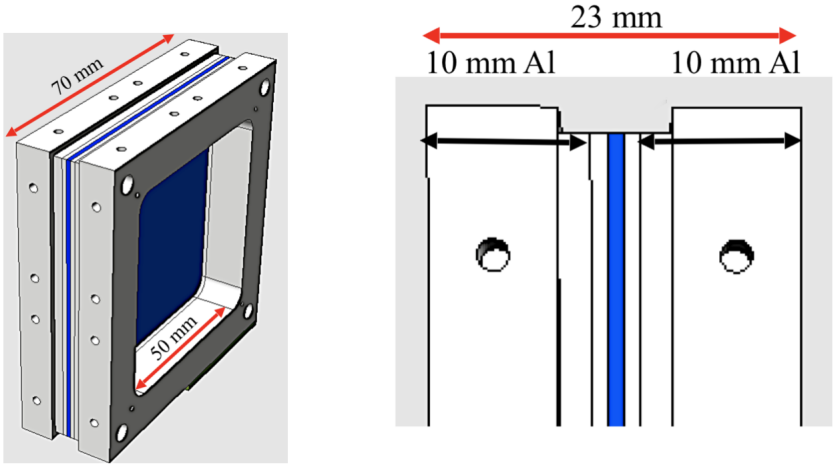


**Figure 4.1.** Schematic view of the SC FOOT: the EJ-204 plastic scintillator is held by an aluminum mechanical structure. The holes in the aluminum frame are used to fix the readout electronics and the SiPMs used for the readout in the proper position ensuring the silicon sensors contact with the plastic scintillator.

## 4.3 ΔE-TOF detector

The ΔE-TOF detector contributes to the particle identification by providing the velocity $\beta$ of the crossing fragments, which can be obtained by the TOF, and the atomic number Z (see sec.2.4.5). The detector is composed of two layers of plastic scintillator bars ( $EJ-204$), arranged orthogonally and wrapped with a thin layer of aluminum that minimise the light loss. Each bar, read by silicon photomultipliers, is 4 mm thick, 2 cm wide and 44 cm long. Each layer is composed by 20 bars in order to match the angular aperture ($< 10°$) of the heavier fragments at the distance of the detector from the target ($40 \times 40$ cm$^2$ active area at $\sim 2$ m distance). Fig.4.2 shows a schematic view of the ΔE-TOF detector. The thickness of the bars is chosen as a trade-off between the amount of scintillation light produced in the bar (resulting in a better timing and energy resolution), which increases with the deposited energy and therefore with the bar thickness, and the systematic uncertainty induced on the ΔE-TOF measurement by secondary fragmentation in the bars that would worsen the particle identification and tracking. Each extremity of the bar is coupled to two Hamamatsu MPPCs SiPMs with $3 \times 3$ mm$^2$ active area and 25 $\mu$m microcell pitch. The 80 signals are digitized at 5 Gsamples/s by the WaveDAQ electronics, described in sec.4.4. A total of 1024 samples are collected for each signal allowing to record the whole waveform. To meet the FOOT experiment final requirements, the ΔE-TOF detector should achieve resolutions $\sigma_{\Delta E}/\Delta E \sim 2-3\%$ and $\sigma_{TOF} \sim 70$ ps when performing the ΔE and TOF measurements, respectively.

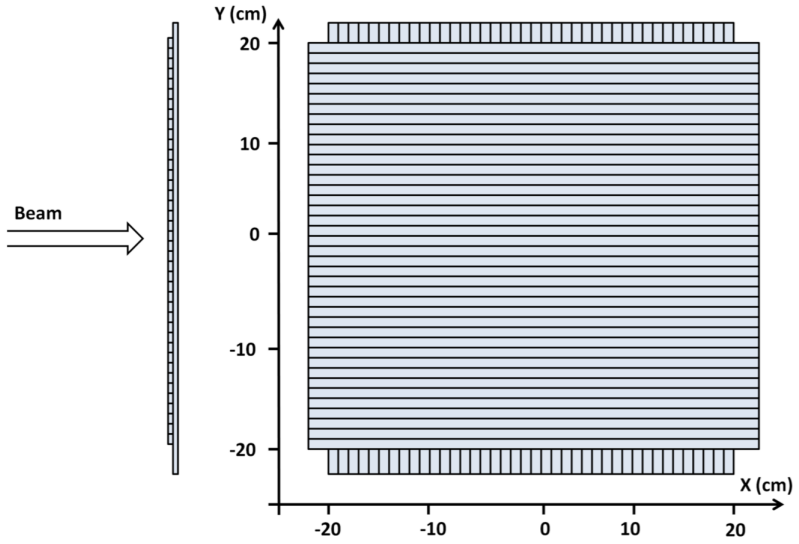


**Figure 4.2.** Schematic view of the TOF wall scintillator detector.

## 4.4 WaveDAQ system

The WaveDAQ (WDAQ), developed in collaboration by PSI and INFN[55], is a compact and highly integrated trigger and data acquisition system.
One crate has 16 digitizing boards, called WaveDREAMs (WDB) connected to the

two central slots and used to receive 16 inputs to be digitized by two Domino Ring Sampler chips (DRS) (one chip for 8 boards)[56] capable of 0.5-5 GSPS sampling speeds. The 16 inputs provide GHz bandwidth and programmable amplification with a selectable pole zero cancellation circuit.
The trigger, synchronization and busy flags are distributed on the backplane together with a low jitter ($< 10$ ps) and a low skew clock (trigger bus). Fig.4.3 shows a schematic view of the WaveDAQ system. The two central slots in a create are:

- The Data Concentrator Board (DCB) that generates and distributes the main reference clock while handling the data received by WaveDREAMs, combining them into a single Gigabit Ethernet interface;
- The Trigger Concentrator Board (TCB) that receives all trigger informations from the WaveDREAMs and generates a shared trigger signal when amplitude and time based algorithms detect an event of interest.

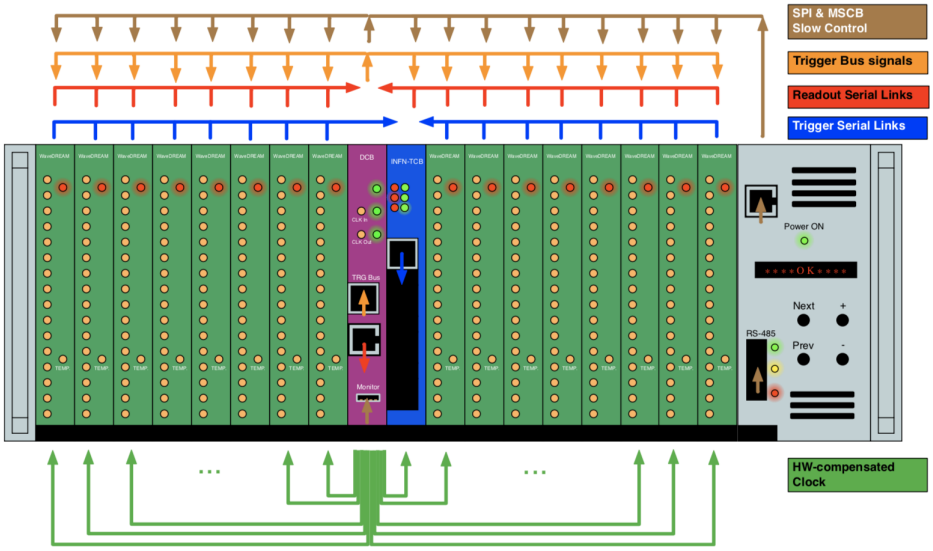


**Figure 4.3.** Schematic view of a single FOOT WaveDAQ crate: green boards are WaveDREAM fronted boards, the magenta board is the DCB while the blue one is the TCB. Arrows show connections in the backplane: red arrows for data transmission to backend machines, blue arrows for trigger serial links, orange arrows to distribute the trigger signal on the backplane and green arrows for hardware compensated clock distribution. Brown arrows show low level access for slow control and configuration.

**Time calibration** The DRS4 chip is an analog waveform digitizer composed of a chained array of 1024 cells, each of them is used to store a time-bin of the waveform. As the doping level of the silicon present in the DRS4 sampling cells is known with an uncertainty of about 10% and thus the transistors parameters in the chip are not fixed, a timing calibration is necessary to take into account for the different time response of each cell. An internal oscillator with known frequency is sampled by the channels of DRS4, and the deviation between the expected period and the measured one is used to determine the effective width of each cell [57].

**Inter-calibration** As already mentioned, the FOOT experiment TOF detectors have several readout channels (8 for the SC and 80 for the TW) that are arranged in different WaveDREAM boards or Domino chips of the same WaveDREAM board. In order to compute the particles TOF it is crucial to synchronize the detectors signals acquired by the channels that belong to different DRS4 chips of the same WaveDREAM board or to different boards. To this aim the clock curve of each DRS4 chip is acquired by a dedicated clock readout channel that is hence used to measure time jitter between the detectors.

# Chapter 5

# Study of the Time Of Flight detectors performance

In this chapter I present the analysis work I have done to asses the partial electronic setup performance and in particular the TOF detectors performance and overall resolution. The data analyzed have been acquired using $^{12}C$ and $^{16}O$ ion beams of different energies, impinging on the start counter (SC) and the scintillator wall (TW). For the first time, in 2019, the SC has been tested in the FOOT experiment context. Therefore I have concentrated my efforts on the analysis of the signals acquired by the SC to characterize the detector and obtain the expected time resolution. Aim of my work was the development and characterization of the Time Of Flight (TOF) detectors: the SC and TW signals, which provide the start and the end of the TOF respectively, have been analyzed to measure the achievable TOF resolution in the experimental conditions that are foreseen for the FOOT future operation.
In sec.5.1 the experimental setup used for the data collection with carbon and oxygen beams are described in detail. In sec.5.2 the procedures and algorithms used to analyze the waveforms and evaluate the arrival time on both SC and TW are reviewed. Finally, in sec.5.3 the results obtained for each experimental setup are reported.

## 5.1 Experimental setup at CNAO and GSI

The data analyzed in this chapter were acquired using different experimental setups, testing the time of flight detectors with $^{12}C$ and $^{16}O$ ions beam at CNAO (Pavia, Italy) and GSI laboratory (Darmstadt, Germany) respectively. Each experimental setup is described in detail hereafter.

### 5.1.1 $^{12}C$ ions beam

**CNAO1**
The SC has been tested for the first time at the CNAO experimental room with $^{12}C$ ions beam. The general setup is shown in Fig.5.1: the beam crosses the SC, 250 $\mu$m thick, and then two vertical bars (bar1 and bar2) used to build the TW that are placed at a relative distance of 45 cm, starting from a distance of 80 cm from the

start detector. Since it is expected that only 5% of the incident ions fragment inside the SC or TW, I neglected the fragmentation contribution and assumed that the beam crossed the setup approximately along a straight line without being subjected to deflections or fragmentations. Therefore to reconstruct the exact interaction point only two parallel bars were needed.

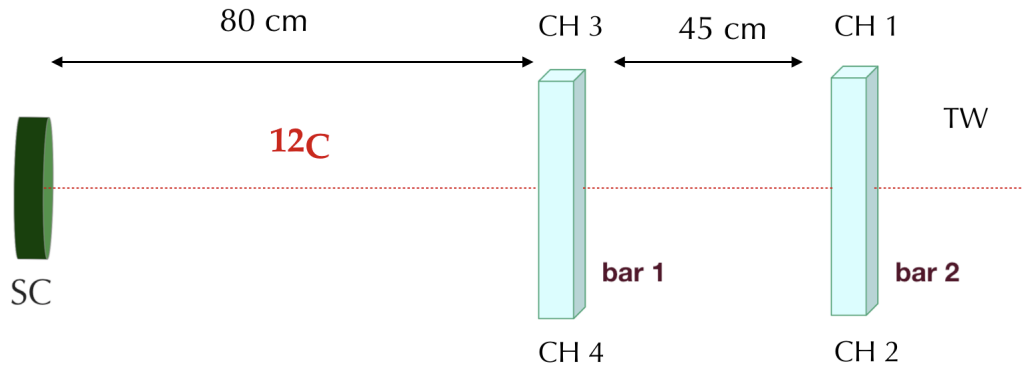


**Figure 5.1.** Schematic view of the CNAO1 experimental setup.

Concerning the electronic readout, only one board has been used to acquire the 16 waveforms and the detectors clock readout channels (explained in detail in sec.5.2). All the channels employed are listed in Tab.5.1 together with their connection details.

| CH | Detector | CH | Detector |
|---|---|---|---|
| **0** | EMPTY | **9** | SC |
| **1** | TW (bar2) | **10** | SC |
| **2** | TW (bar2) | **11** | SC |
| **3** | TW (bar1) | **12** | SC |
| **4** | TW (bar1) | **13** | SC |
| **5** | EMPTY | **14** | SC |
| **6** | EMPTY | **15** | SC |
| **7** | EMPTY | **16** | CLK-TW |
| **8** | SC | **17** | CLK-SC |

**Table 5.1.** WaveDREAM board channels map: the SC and TW terms indicate the channels that belong to the start counter and the scintillator wall bars respectively. The TW and SC detector channels belong to two different chips and thus they have two different clock curves (see sec.4.4) acquired by CLK-SC and CLK-TW channels.

This experimental setup has been tested using carbon ions beams with 3 mm transverse dimension ($\sigma$) measured at the isocenter, of the following energies: 115 MeV/u, 151 MeV/u, 221 MeV/u and 280 MeV/u.

**CNAO2**

Several carbon ions beams were also used to test the full FOOT scintillator wall in coincidence with the SC detector. Fig.5.2a shows the experimental setup: the SC, 250 $\mu$m thick, and the fully assembled TW are positioned at a relative distance of 2.10 m.

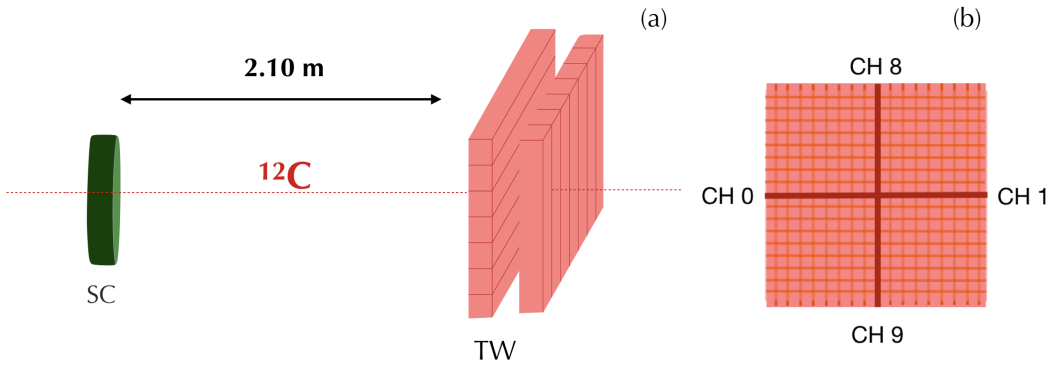


**Figure 5.2.** Schematic view of the CNAO2 experimental setup (a) and of the considered TW bars (b).

The SC signals have been acquired using 8 channels of the WaveDREAM board n.27 while the ones of the scintillator wall by six WaveDREAMs. Each board had two clock readout channels, one for each chip (see Tab.5.2).
Since also in this case the expected fragmentation contribution in the SC or TW is lower than 5% and therefore negligible for the data analysis purposes, only the central bars of the two layers have been considered (see Fig.5.2b), namely I have analyzed only the waveforms acquired by CH 0-1 of the board 94 and CH 8-9 of the board 82.

The TOF resolution has been tested using carbon ions beam with 3 mm ($\sigma$) isocenter size, of energies: 115 MeV/u, 260 MeV/u and 400 MeV/u.

| **Board** | **CH** | **Detector** |
|---|---|---|
| **27** | **0-7** | SC |
| | **8-15** | EMPTY |
| | **16,17** | CLK |
| **78** | **0-15** | TW |
| | **16,17** | CLK |
| **79** | **0-15** | TW |
| | **16,17** | CLK |
| **80** | **0-15** | TW |
| | **16,17** | CLK |
| **81** | **0-15** | TW |
| | **16,17** | CLK |
| **82** | **0-15** | TW |
| | **16,17** | CLK |
| **94** | **0-15** | TW |
| | **16,17** | CLK |

**Table 5.2.** Board channels map: the SC and TW terms indicate the channels that belong to the start counter and the scintillator wall respectively. The ninety TW readout channels were divided into blocks connected to different WaveDREAM boards. Each board has two chips and thus two different clock signals acquired by the CLK channels.

### 5.1.2 $^{16}$O ions beam

**GSI**

At the GSI laboratory the TOF detectors (the SC, 250 $\mu$m thick, and the TW) have been tested using the experimental setup reported in Fig.5.3a, using $^{16}$O ions beam with a transversal plane dimension of 2 mm ($\sigma$) measured at isocenter, of 400 MeV/u. In the setup were included also the Beam Monitor and Vertex detector (see sec.2.3.1). Likewise to the beam test at CNAO, the target was not included and only the central barrels of the scintillator wall have been considered (see Fig.5.3b), neglecting the contribution from possible fragmentation interactions in the different detectors placed between the SC and the TW.
The readout configuration is the one reported in Tab.5.2.

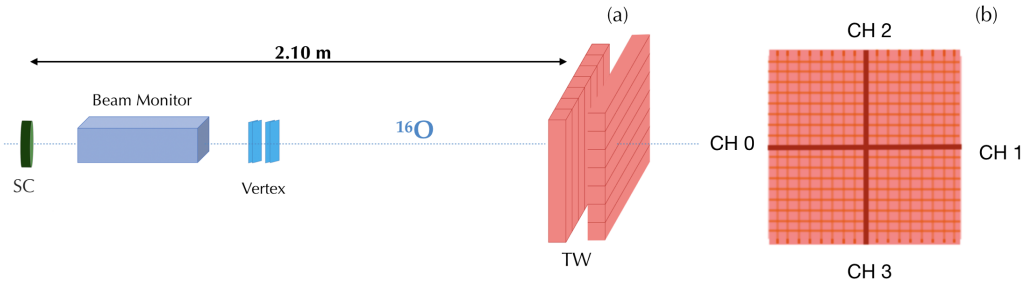


**Figure 5.3.** Schematic view of the GSI experimental setup (a) and of the considered TW bars (b).

## 5.2 Waveforms Analysis

As already said in chapter 2, the TOF measurement is provided by the coincidence between the SC and the TW detectors. When the incident particles hit the detectors, the produced electronic signals are acquired by a certain number of channels connected to one or more boards, depending on the experimental setup. Fig.5.4 shows some examples of the signals produced by the interaction of incoming Carbon ions with the SC and acquired by eight different readout channels.
All the results presented hereafter have been obtained using the same analysis strategy with algorithms that have been fine tuned accordingly to the different experimental setup. Fig.5.5 shows the SC and TW signals as measured using a waveform digitizer obtained when a $^{12}C$ ions beam of 115 MeV/u energy was impinging on the two detectors without crossing any target. Both signals have been fitted using an inverted **Lognormal function** (from this point on called $\boldsymbol{f}$).

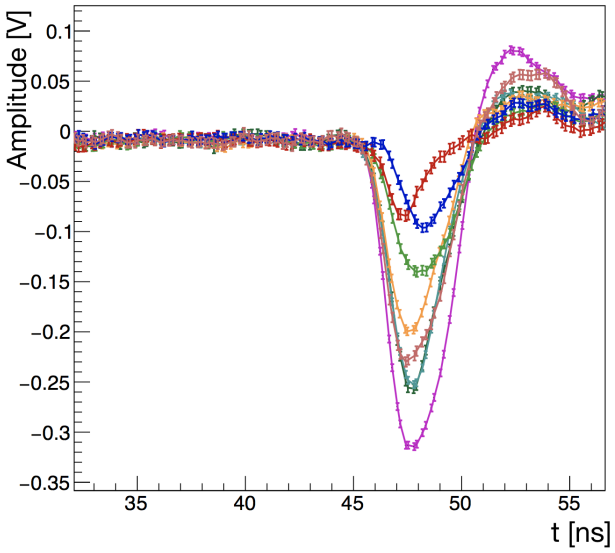


**Figure 5.4.** The electronic signals produced by the interaction of a $^{12}$C ion of 115 MeV/u energy with the SC (CNAO1) and acquired by the eight SC readout channels. The channels with a worse time resolution correspond to the signals with a less amplitude, e.g. CH 9 (red curve) and 10 (blue curve), and vice versa.

The amplitude uncertainties of all the waveforms have been assigned looking at the baseline fluctuations: the first 50 samples acquired when the particle has not yet crossed the detector, have been considered and the uncertainties have been set as the standard deviation (0.003 V mean value for the SC and 0.004 V mean value for the TW):

$$< v >_{SDD} = \sqrt{\frac{\sum_i (v_i - < v >)^2}{N-1}} \tag{5.1}$$

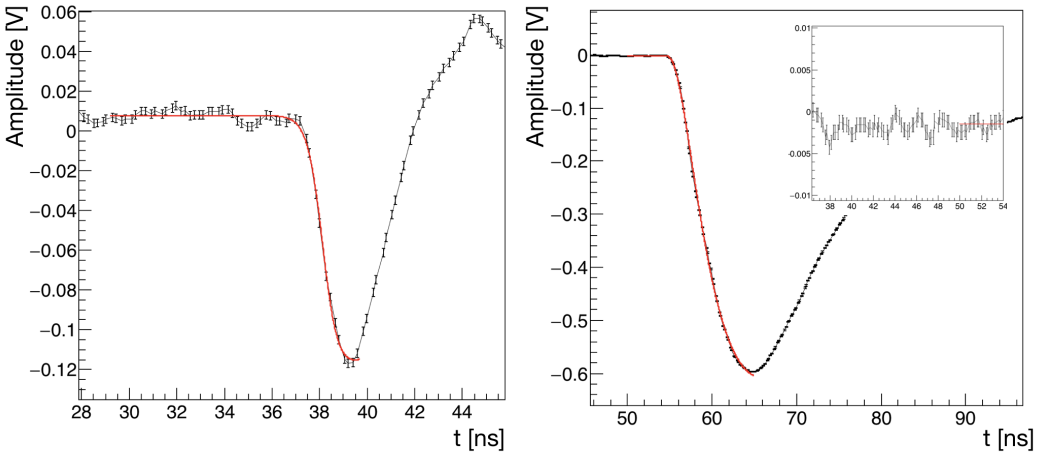


**Figure 5.5.** Example of the SC (left) and TW (right) waveforms as measured from the digitizer, obtained when a $^{12}C$ ion beam of 115 MeV/u energy was impinging on the SC and then on the TW. Both signals have been fitted using the function $f$ (red curve). The baseline has been already subtracted. The box (right) at the top right is a magnification of the first ns acquired by the TW.

For each experimental setup I verified the goodness of the fit performing the $\chi^2$ test. Fig.5.6 shows the $\chi^2$ distribution for the SC and TW fitted signals obtained for the CNAO1 data samples at 115 MeV/u (analyzing the other data I have obtained similar results).

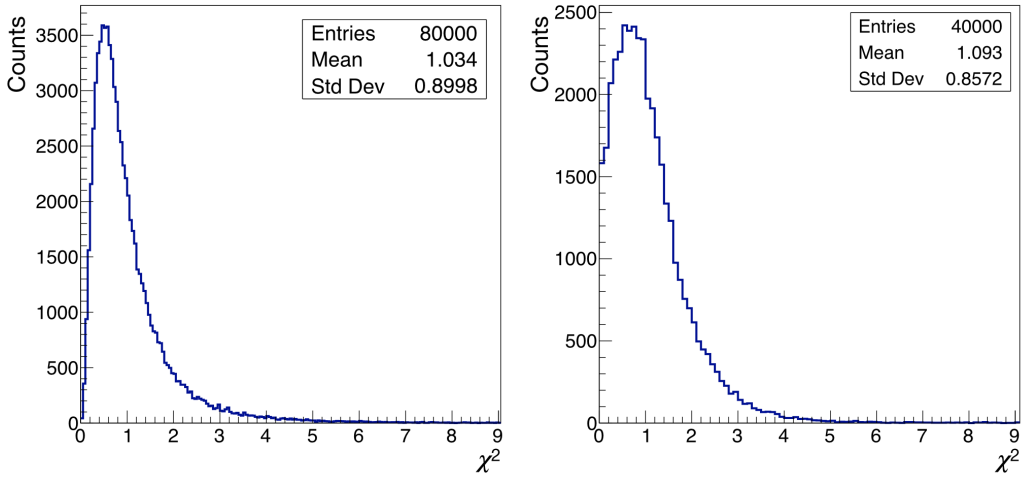


**Figure 5.6.** Example of the $\chi^2$ distribution of all SC and TW channels obtained when analyzing the data samples with $^{12}C$ ions beam of 115 MeV/u energy.

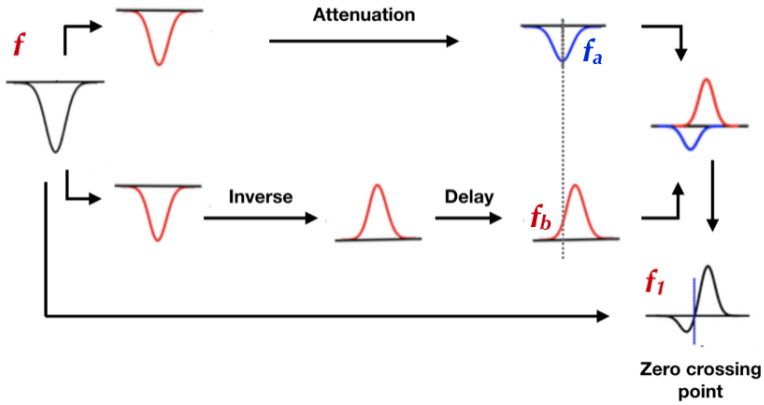


**Figure 5.7.** Scheme of the Constant Fraction Discriminator (CFD) operation coded in my algorithm. The input signal is split into two identical parts equal to the original signal. One part is attenuated to a fraction **frac** of the original amplitude, and the other part is inverted and delayed by a **del** factor. These two signals $f_a$ and $f_b$ respectively are subsequently added to form the constant-fraction timing signal $f_1$. The reference time is set as the zero crossing point of the $f_1$ function.

As can be seen in Fig.5.4, the signals have different amplitudes. To account for such fluctuations and to evaluate the arrival times on both SC and TW, independently of the signal amplitude, I have implemented a software algorithm capable of reproducing the Constant Fraction Discriminator (CFD) operation mode. Fig.5.7 shows the schematic view of the CFD operation coded in my algorithm. Each signal is fitted using ***f***. The resulting function is split into two identical parts equal to the

original one. One part is attenuated to a fraction **frac** of the original amplitude obtaining $f_a$, and the other is inverted and then delayed by a **del** factor obtaining $f_b$. These two signals are subsequently added to form the constant-fraction timing signal ($f_1$). The reference time then is set as the zero crossing point of the function $f_1$. The values of the parameters **frac** and **del** have been carefully optimized by evaluating their impact on the time resolution: each experimental setup has been analyzed several times using **frac** and **del** values between 0.005-0.5 and 0.5-2 ns respectively and the time resolution has been used to identify the best set of operational parameters.
Since the signals produced by the TW and SC end up in different electronic chips of the same (CNAO1) or of two different (CNAO2 and GSI) WaveDREAM boards which have different clock times (see sec.4.4), it is necessary to synchronize the various clock times to minimize the systematic uncertainty contribution to the time resolution. The time jitter ($\Delta Clock$) between the two detectors needs to be properly taken into account when computing the particles TOF. For this reason, in order to synchronize the signals, each TOF detector has a clock readout channel, to measure the corresponding clock time. Fig.5.8 shows, as an example, the SC related clock curve (the eight SC channels end up in a single chip and thus they have a common reference clock signal).

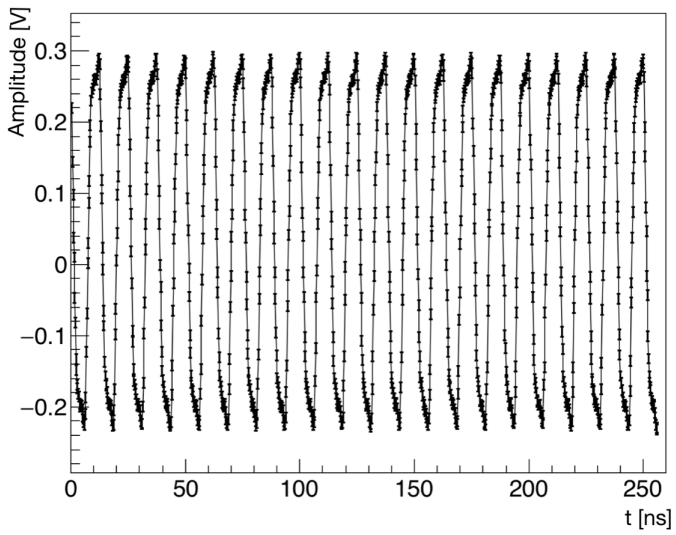


**Figure 5.8.** Clock curve acquired for the SC detector. The uncertainties have been set as the mean between the ones assigned to the TW and SC signals (see Eq.5.1).

The rising edges of the clock waveforms have been parametrized with the function ***fc***, obtained from the Fermi-Dirac distribution.

$$f_c = \frac{[0]}{1 + e^{-\frac{x-[1]}{[2]}}} - [3] \tag{5.2}$$

where the parameters [0],[1],[2] and [3] have been extracted from a fit to the acquired waveforms. The zero-crossing point of the fit function is identified as the reference time $Tc$.

The full signal window is analyzed and the stability of the clock ($\Delta$t between two consecutive crossing times) can be checked. When analyzing the clock waveforms I had to consider not only the precision and accuracy of the implemented analysis methods but also the processing time. To this purpose I have tested the impact of simplifying the fit function using a linear fit ***fc'*** ($[0] * x + [1]$, with [0] and [1] fit parameters). In this case, the fit range has been set to include at least 4 points before and after $t_0$ ($t_0 - 0.8$ ns, $t_0 + 1.2$ ns). Fig.5.9a-b shows a comparison between the two fit functions. Using the linear parametrization I have obtained the $\chi^2$ distribution reported in Fig.5.9c with a mean $\chi^2$ equal to 1.13.
Fig.5.10 shows the clock curve of the SC detector with all the rising edges fitted using the ***fc'*** function.

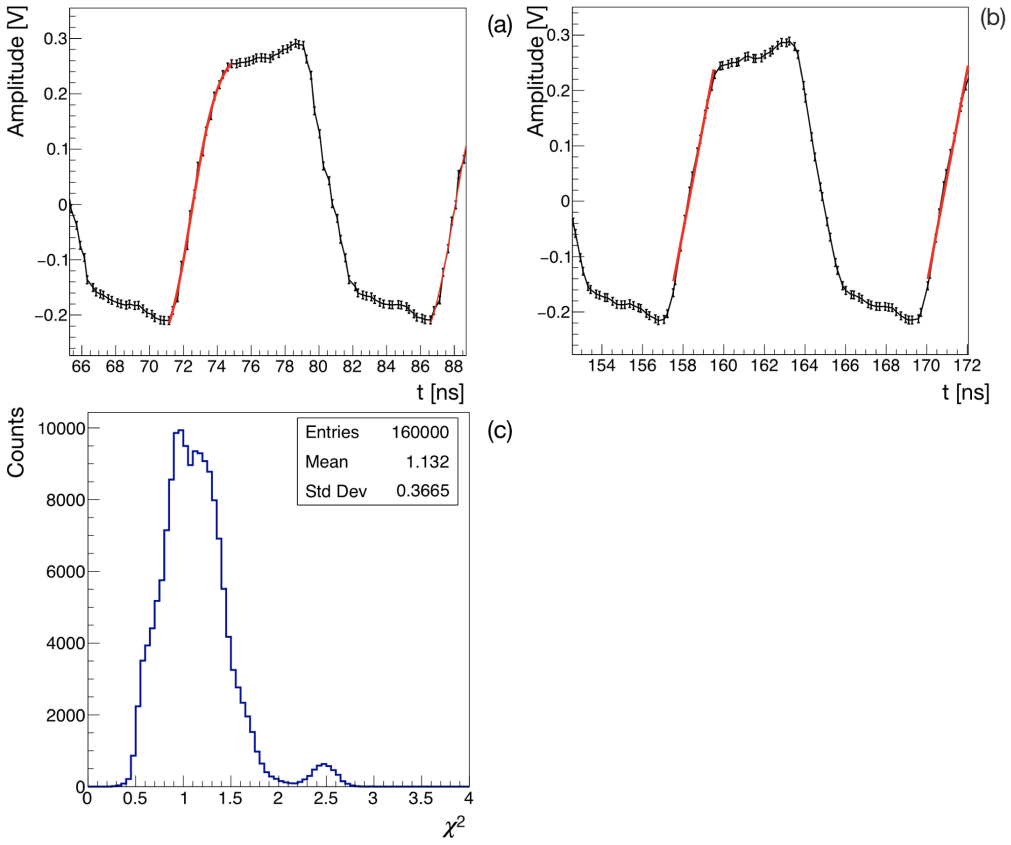


**Figure 5.9.** Clock curves for the SC detector fitted with the Fermi-Dirac function (a) and with a 1st order polynomial (b). For the last parametrization the $\chi^2$ distribution is also reported (c), the second peak is attributed to the small fraction of cases in which the fit failing to reproduce the waveform behavior (delayed onset or anticipated plateau regions).

Since each TW and SC channels acquired by the digitizer, ends up in two different chips of the same (CNAO1) or different (CNAO2 and GSI) WaveDREAMs boards, each having its corresponding reference clock time, the time jitter between the SC and TW chips for the i-th rising edge has been evaluated as follows:

$$\Delta Clock_i = Tc_{tw_i} - Tc_{sc_i} \tag{5.3}$$

where $Tc_{tw_i}$ and $Tc_{sc_i}$ are the zero crossing points of the TW and SC clock curves, respectively.

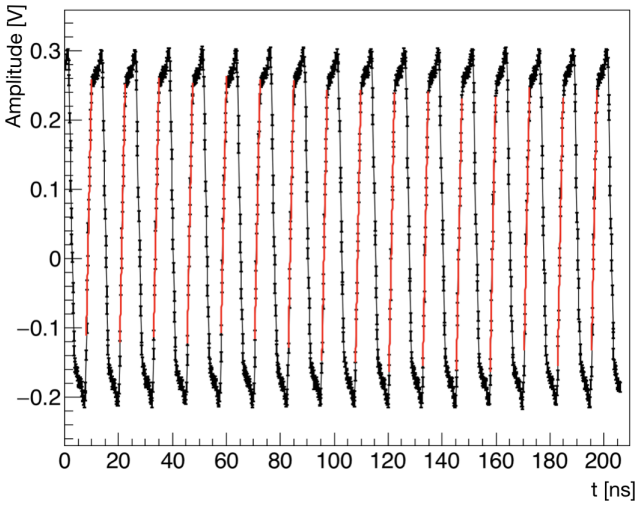


**Figure 5.10.** Clock waveforms for the SC detector. The fit performed with $f_c'$ function is superimposed in red.

Fig.5.11a shows a magnification of the SC (blue curve) and TW (green curve) overlapping clock signals while Fig.5.11b shows in detail the $\Delta Clock$ evaluation. Finally, the total time jitter has been evaluated for each channel as the difference between the average clock times of the TW and that of the SC:

$$\overline{\Delta Clock} = \overline{Tc}_{tw} - \overline{Tc}_{sc} \tag{5.4}$$

where

$$\overline{Tc}_{tw} = \frac{\sum_i Tc_{tw_i}}{N} \qquad \overline{Tc}_{sc} = \frac{\sum_i Tc_{sc_i}}{N} \tag{5.5}$$

with N the number of the fitted rising edges. These $\Delta Clock$ values have been subtracted to the TOF measurements. From this point on, if the considered TW and SC channels belong respectively to only one WaveDREAM board and chip and therefore they have only one reference clock time each[1], the TOF values have already the $\Delta Clock$ subtracted as follows:

$$TOF = \overline{T}_{tw} - \overline{T}_{sc} - \Delta Clock \tag{5.6}$$

Since the particles arrival time on the scintillator wall is measured by the TW channels with approximately the same resolution, $\overline{T}_{tw}$ has been set as the arithmetic average arrival time measured by the $N$ TW channels:

$$\overline{T}_{tw} = \frac{\sum_i T_{tw_i}}{N} \tag{5.7}$$

where $T_{tw_i}$ is the arrival time measured by the i-th channel.

[1] In the data analysis presented here this condition is always verified.

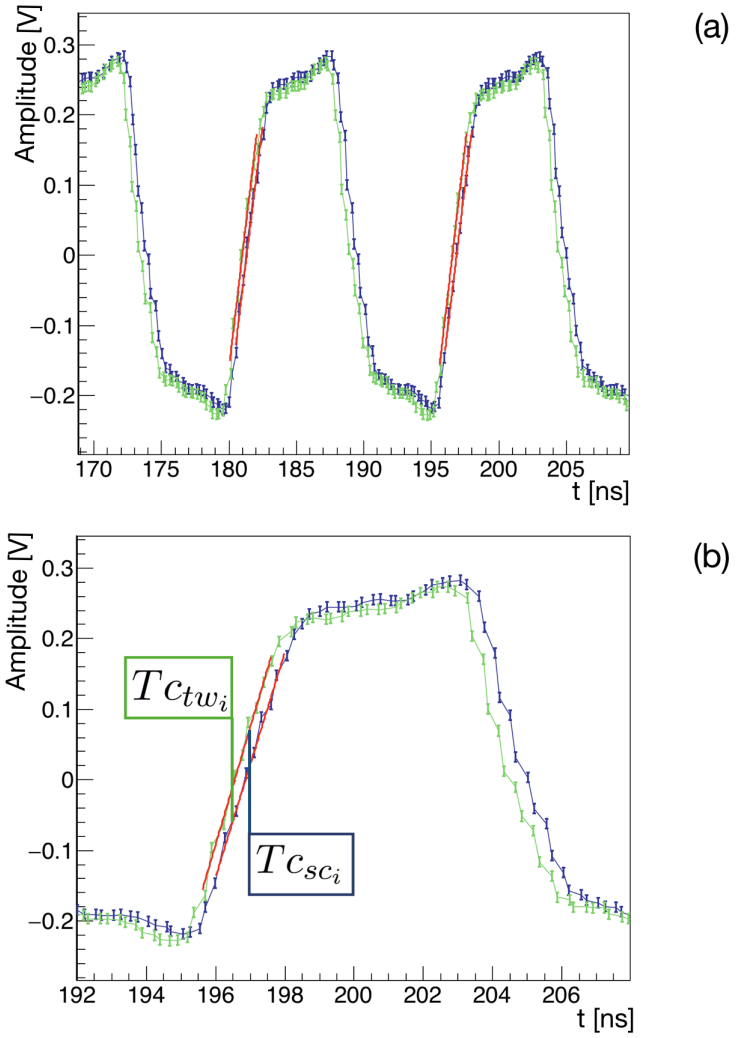


**Figure 5.11.** SC (blue) and TW (green) clock curve. The (b) panel is a magnification of the (a) one. $Tc_{tw_i}$ and $Tc_{sc_i}$ are the reference times of the TW and SC respectively, to evaluate the time jitter.

As the time resolutions of the SC channels differ significantly I have computed the start time of the TOF ($\overline{T}_{sc}$) as the weighted average of the 8 SC channels arrival times:

$$\overline{T}_{sc} = \frac{\sum_i \omega_i t_{sc_i}}{\omega_i} \qquad \omega_i = \frac{1}{\sigma_i^2} \tag{5.8}$$

The weights used correspond to the inverse square of each channel time resolution that has been extracted from the TOF distribution measured by each SC channel. These distributions have been obtained computing the difference between Eq.5.7 and the arrival time measured by the i-th SC channel $T_{sc_i}$ (see Fig.**??**):

$$TOF_i = \overline{T_{tw}} - T_{sc_i} \tag{5.9}$$

where $i = 1, ..., 8$ is the SC channel index. Finally the TOF has been evaluated as follows:

$$TOF = \overline{T}_{tw} - \overline{T}_{sc} \tag{5.10}$$

where the $\Delta Clock$ is correction has been already applied. The corresponding resolution $\sigma(TOF)$ is then:

$$\sigma(TOF)^2 = \sigma(T_{tw})^2 + \sigma(T_{sc})^2 \tag{5.11}$$

Fig.5.12 shows an example of the TOF distribution obtained for $^{12}$C ions beam of 151 MeV/u energy (CNAO1).

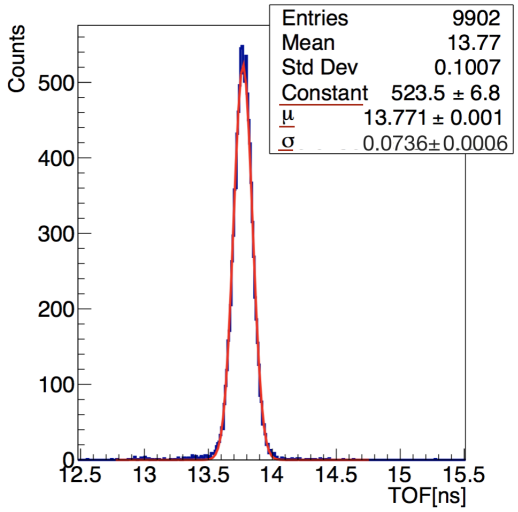


**Figure 5.12.** TOF distribution evaluates according to Eq.5.10, the data are retrieved from the CNAO1 data analysis acquiring with $^{12}$C ions beam of 115 MeV/u energy.

The resolutions $\sigma(T_{tw})^2$ and $\sigma(T_{sc})^2$ assigned to each detector will be discussed in the next section where the results obtained for both $^{12}C$ and $^{16}O$ ion beams are reported in detail.

## 5.3 TOF measurements

In this section I present the results obtained analyzing the data samples collected using $^{12}C$ and $^{16}O$ ion beams. Each analyzed dataset contains approximately 10000 events.

### 5.3.1 Arrival time measurements optimization

To evaluate the arrival time on the SC and the TW with the best achievable resolution, as said in the previous section, I have used an algorithm implementing the CFD operation mode. First of all I have looked for the **frac** and **del** parameters combinations minimizing the resolution on the arrival time of the SC and TW. I have performed an analysis in which **frac** and **del** factors have been changed in the range 0.005-0.5 and 0.5-2 ns respectively, and the values that optimize the single TOF distribution, i.e. the one obtained as Eq.5.9, have been chosen. As an

example Tab.5.3 shows the obtained factors for the SC and TW channels for $^{12}$C ions beam of 115 MeV/u energy (CNAO1). This procedure has been performed for each experimental setup and beam energy.

| **TW** | | | **SC** | | | **SC** | | |
|---|---|---|---|---|---|---|---|---|
| $CH$ | $frac$ | $del$ [ns] | $CH$ | $frac$ | $del$ [ns] | $CH$ | $frac$ | $del$ [ns] |
| **1** | 0.5 | 4 | **8** | 0.2 | 2 | **12** | 0.2 | 2 |
| **2** | 0.5 | 4 | **9** | 0.5 | 2 | **13** | 0.2 | 2 |
| **3** | 0.5 | 4 | **10** | 0.5 | 2 | **14** | 0.2 | 2 |
| **4** | 0.5 | 4 | **11** | 0.2 | 2 | **15** | 0.2 | 2 |

**Table 5.3. Frac** and **del** factors for the SC channels chosen for the $^{12}$C ions beam data samples at 115 MeV/u.

As already anticipated, I have decided to evaluate the arrival time on the SC detector according to Eq.5.8 with the $\omega_i$ equal to the inverse square of the sigma values retrieved from the distribution of the TOF values measured for each SC channel (see Eq.5.9).
For example, Fig.5.13 shows the distributions obtained from the data samples with carbon ions of 115 MeV/u energy (CNAO1). In Tab.5.4 are summarized the relative SC channel resolutions evaluated according to Eq.5.11 (see sec.5.3.3 for the TW resolution). As can be seen, there are some channels that show better resolutions, while other (e.g. CHs 9, 10, 11 and 12) are significantly worse.

| **CH** | $\sigma$ [ns] | **CH** | $\sigma$ [ns] |
|---|---|---|---|
| **8** | $0.130 \pm 0.002$ | **12** | $0.170 \pm 0.002$ |
| **9** | $0.315 \pm 0.002$ | **13** | $0.119 \pm 0.002$ |
| **10** | $0.252 \pm 0.002$ | **14** | $0.115 \pm 0.002$ |
| **11** | $0.167 \pm 0.002$ | **15** | $0.117 \pm 0.002$ |

**Table 5.4.** The $\sigma$ values used to evaluate the arrival time on the SC, are extracted from the difference between the single TOF distributions given by Eq.5.9 and the TW resolution (see sec.5.3.3), $\sigma(T_{sc})^2 = \sigma(TOF_i)^2 - \sigma(TW)^2$. The data are retrieved from the CNAO1 data analysis and were collected using $^{12}$C ion beams of 115 MeV/u energy.

The same result has been obtained analyzing the distribution of the TOF measured for each SC channels (see Eq.5.9) of the other available data. Tab.5.4 shows a significant difference between the time resolution obtained for channels 9 and 10 with respect to the other channels. Such behavior is observed also in the other data sets. A possible explanation of such difference comes from the different optical coupling of some SiPMs to the scintillator (e.g. SiPMs misplaced). Such hardware misalignments or hardware defects are also explaining the large difference in the signal amplitude reported in Fig.5.4.

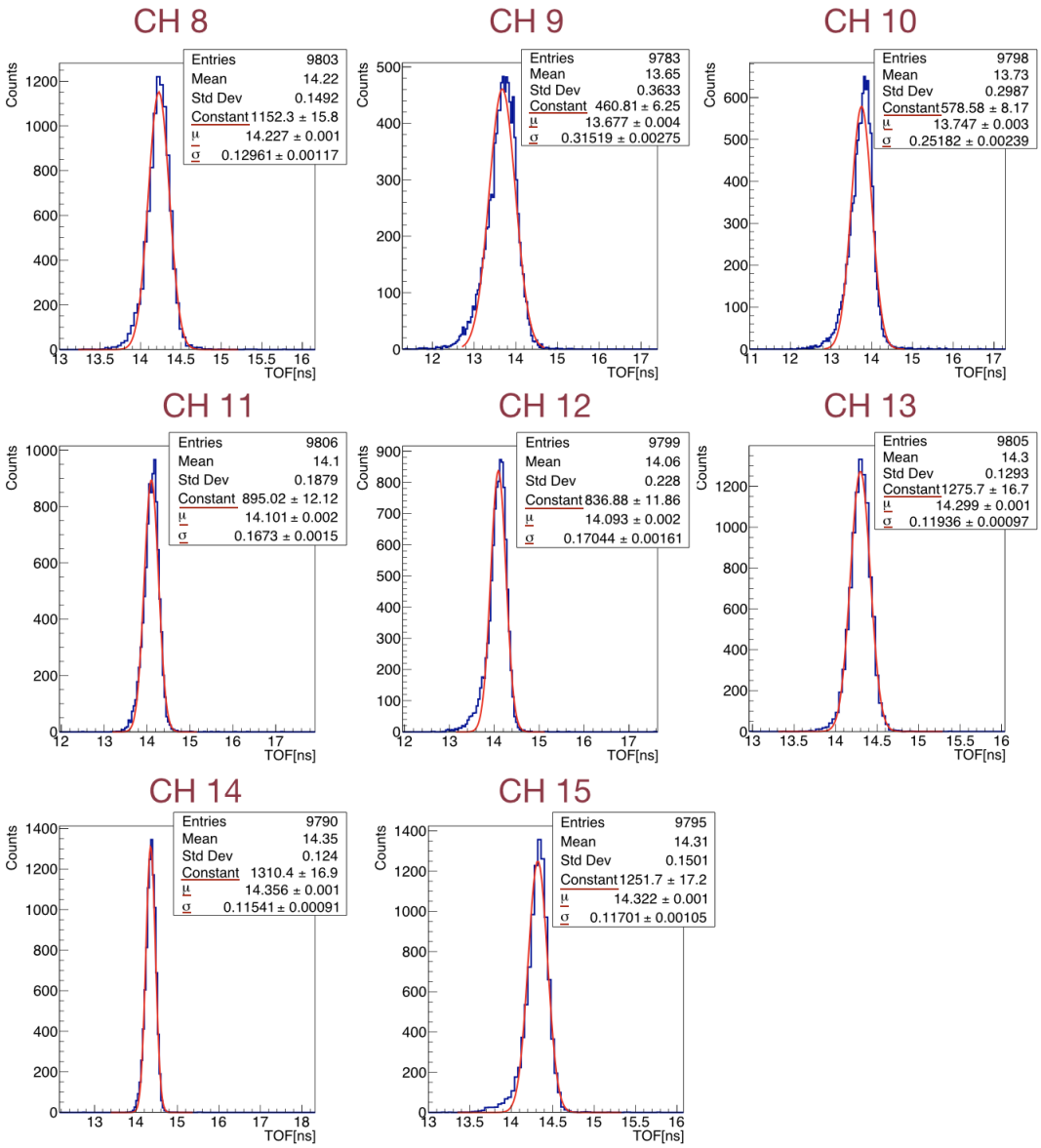


**Figure 5.13.** TOF distributions measured for each SC channel according to Eq.5.9, the data are retrieved from the CNAO1 data analysis acquiring with $^{12}$C ions beam of 115 MeV/u energy.

The TOF values measured by each SC channel ($TOF_i$) are distributed according to a Gaussian function $G(\mu_i, \sigma_i)$ (see Fig.5.13). Therefore the TOF measured at each event is approximately distributed according to a Gaussian distribution given by:

$$\overline{TOF} \sim G\left(\frac{\sum_i \frac{\mu_i}{\sigma_i^2}}{\sum_i \frac{1}{\sigma_i^2}}, \sqrt{\frac{1}{\sum_i \frac{1}{\sigma_i^2}}}\right) \qquad i = 1, .., 8 \tag{5.12}$$

since the SC channels have different resolutions ($\sigma_i$). In order to improve the time resolution, I have decided to apply a cut on the goodness of the fit used to parametrize the SC waveforms: the channels with a $\chi^2$ value under a certain threshold (5%) have

been rejected. Hence all the 8 SC channels are not always considered at each event. For this reason, since the channels $\mu_i$ values vary significantly (see Fig.5.14a), the TOF values measured at each event show a large dependence on the actual channels that have collected a signal. To account for such effect that can cause a widening of the TOF distribution, I have decided to add an additive constant $c_i$ to equalize the times of flight mean values ($\mu_i$) measured by the single SC channels (see Eq.5.9), equal to:

$$c_i = \mu_i - \mu_{ref} \qquad i = 1, .., 8 \tag{5.13}$$

where $\mu_{ref}$ is the TOF mean value measured by the SC channel that has the best time resolution. For example for the CNAO1 data samples at 115 MeV/u I have chosen CH 14 (see Tab.5.4). Therefore subtracting to the TOF distribution measured by each SC channel the constant $c_i$, the $TOF_i$ values measured by each SC channel will be distributed according to Gaussian distributions (see Fig.5.14b) with the same mean values ($G(\mu_i - c_i, \sigma_i) = G(\mu_{ref}, \sigma_i)$).

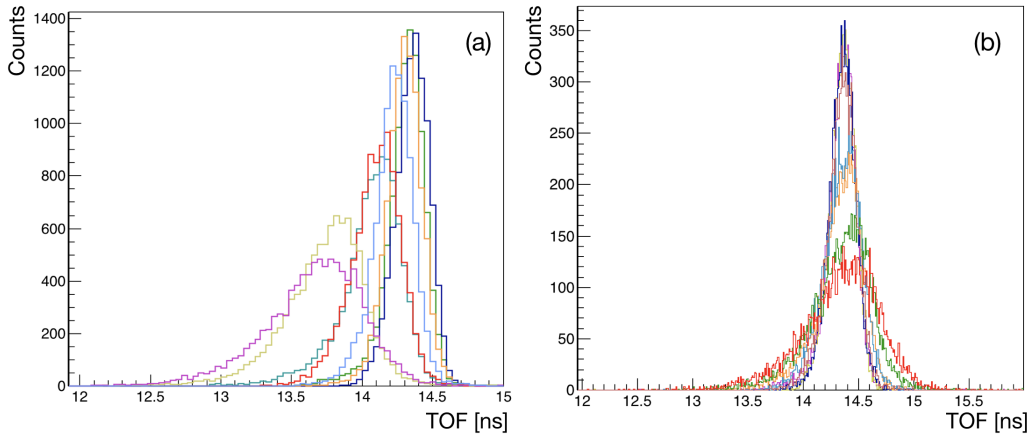


**Figure 5.14.** TOF distributions measured by each SC channels (according to Eq.5.9) with (b) and without (a) having applied the $c_i$ factors. The data are retrieved from the CNAO1 data analysis and were collected using $^{12}$C ion beams of 115 MeV/u energy.

For what concerns the evaluation of the arrival time on the TW, since the information about the TOF mean value was not relevant for the purpose of my work, I have assumed that all the TW bars have the same time resolution, and to consider only the first bar (CH 3-4) and the central bar of the first layer (CH 0-1) for CNAO1 and CNAO2-GSI data samples, respectively.

### 5.3.2 TOF resolution

Hereafter are reported the TOF resolutions obtained for each experimental setup using Eqs. 5.8 and 5.7 to evaluate the SC and TW arrival times respectively.

**CNAO1**

In Fig.5.15 are reported the TOF distributions obtained from the data samples at 115, 151, 221 and 280 MeV/u. The arrival time on the TW has been evaluated using CHs 3-4 of the first bar.

The $\sigma(TOF)$ values obtained from these distributions (Fig.5.15), are summarized in Tab.5.5.

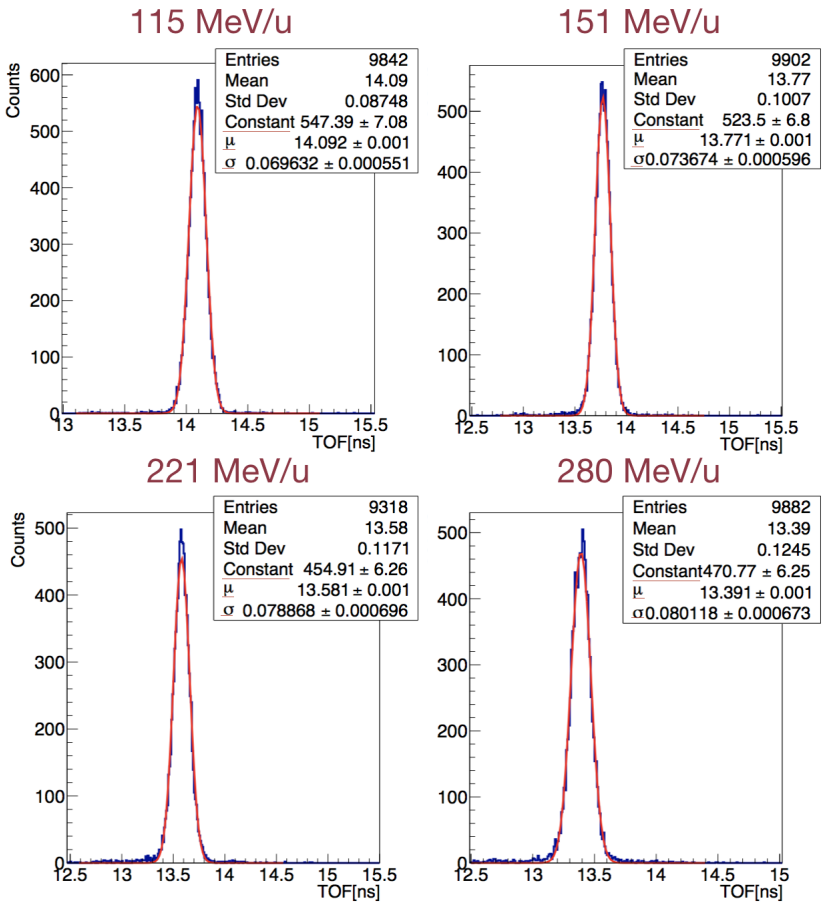


**Figure 5.15.** TOF distribution measured as the difference between the weighted average arrival times of the SC channels and the arithmetic average arrival times of two TW channels (i.e. CH 1-2). The terms highlighted in red in the box at the top right are the fit parameters.

| **Energy [MeV/u]** | $\sigma(TOF)$ [ps] |
|---|---|
| 115 | $69.6 \pm 0.6$ |
| 151 | $73.6 \pm 0.6$ |
| 221 | $78.9 \pm 0.7$ |
| 280 | $80.1 \pm 0.7$ |

**Table 5.5.** TOF resolutions for 115, 151, 221 and 280 MeV/u. The assigned uncertainties are only accounting for the statistical contribution.

**CNAO2**

Fig.5.16 shows the obtained TOF distributions of the data samples at 115, 260 and 400 MeV/u. The arrival time on the TW has been evaluated using CH 0-1 of the first layer central barrel.

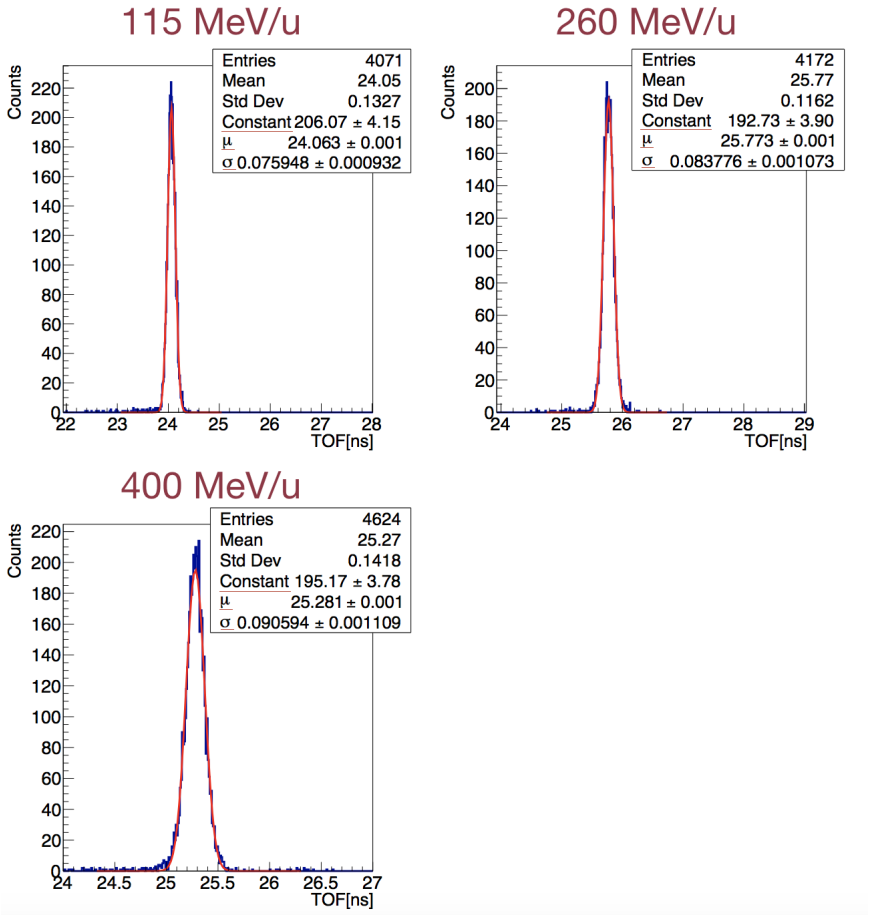


**Figure 5.16.** TOF distribution measured as the difference between the weighted average arrival times of the SC channels and the arithmetic average arrival times of two TW channels (i.e. CH 0-1). The terms highlighted in red in the box at the top right are the fit parameters.

In Tab.5.6 are reported the TOF resolutions retrieved from the fit performed on each distribution.

| **Energy [MeV/u]** | $\sigma(TOF)$ [ps] |
|---|---|
| 115 | $76.9 \pm 1.0$ |
| 260 | $88.9 \pm 1.1$ |
| 400 | $93.2 \pm 1.1$ |

**Table 5.6.** TOF resolutions for 115, 260 and 400 MeV/u. The assigned uncertainties are only accounting for the statistical contribution.

**GSI**

The TOF distribution of the data samples with $^{16}O$ ions beam of 400 MeV/u is shown in Fig.5.17. As the CNAO2 case, the TW arrival time has been evaluated using CH 0-1 of the first layer central barrel. In Tab.5.7 is reported the obtained TOF resolution.

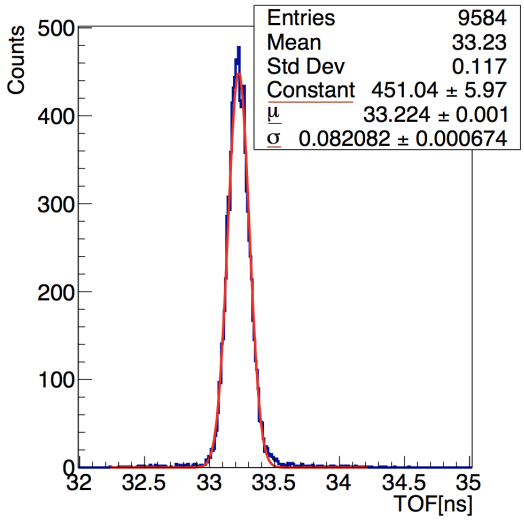


**Figure 5.17.** TOF distribution measured as the difference between the weighted average arrival times of the SC channels and the arithmetic average arrival times of two TW channels (i.e. CH 0-1). The terms highlighted in red in the box at the top right are the fit parameters.

| **Energy [MeV/u]** | $\sigma(TOF)$ [ps] |
|---|---|
| 400 | $82.1 \pm 0.7$ |

**Table 5.7.** TOF resolutions for 400 MeV/u oxygen ions beam. The assigned uncertainties are only accounting for the statistical contribution.

Fig.5.18 shows the obtained TOF resolutions for all the experimental setups as a function of the beam energy. From the figure it can be seen that $\frac{\sigma(t)}{t}$ follows the expected behavior $\sim \sqrt{E_{kin}}$ (see Eq.2.32).
I would have expected that the values of CNAO1 and CNAO2 data samples at 115 MeV/u were comparable, since the detectors used and the beam particles were the same. However, this is not verified: these experimental results indicate that there is a further effect (trigger cell correction) that had not yet been considered. In sec.5.3.5 these time resolutions will be corrected.

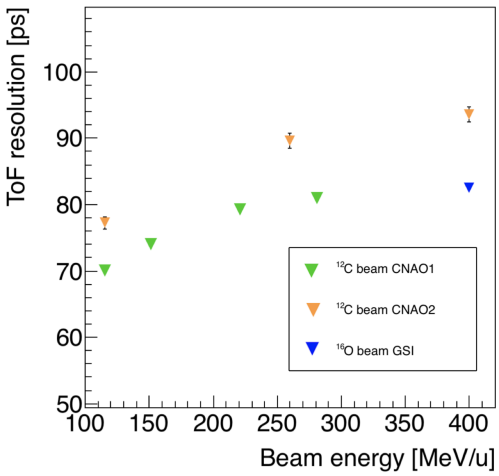


**Figure 5.18.** TOF resolutions as a function of the beam energy. The green, orange and blu points represent the value obtained from the CNAO1, CNAO2 and GSI data analysis respectively.

### 5.3.3 TW resolution

To evaluate the TW resolution, included in Eq.5.11, I have studied the bar resolutions that can be extracted from the distribution of the $\Delta_{bar}$ observable computed as the difference between the averages arrival times measured by the two channels belonging to the same bar (for example $T_{bar_1}$ and $T_{bar_2}$, see Fig.2.4):

$$\Delta_{bar} = T_{bar_1} - T_{bar_2} \tag{5.14}$$

where

$$T_{bar_1} = \frac{t_1 + t_2}{2} \qquad T_{bar_2} = \frac{t_3 + t_4}{2} \tag{5.15}$$

$t_1$ and $t_2$ are, in the case of CNAO1 data samples, the arrival times measured by CH 1 and 2 and in the same way $t_3$ and $t_4$ are the ones measured by CH 3 and 4. If the two bars are assumed to have the same characteristics, and thus $\sigma(T_{bar_1}) = \sigma(T_{bar_2}) = \sigma(T_{bar})$, it follows that:

$$\sigma(\Delta_{bar}) = \sqrt{2}\sigma(T_{bar}) \rightarrow \sigma(T_{bar}) = \frac{\sigma(\Delta_{bar})}{\sqrt{2}} \tag{5.16}$$

From this point on, the TW time resolution has been calculated according to Eq.5.16. Fig.5.19 shows an example of the $\Delta T$ distribution obtained from the CNAO1 data samples at 115 MeV/u.

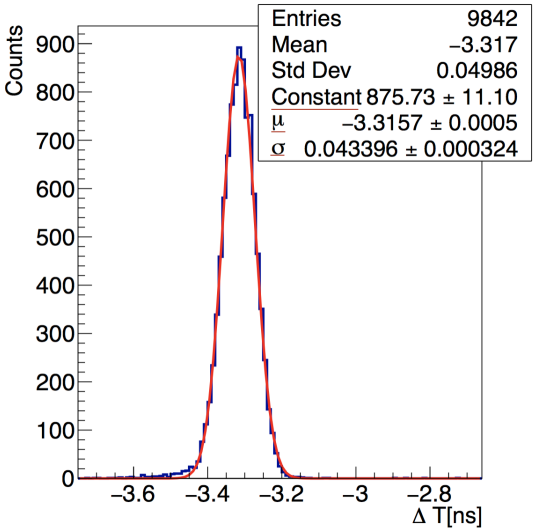


**Figure 5.19.** The arrival times difference ($\Delta T$) distribution between CH 3 and CH 4 retrieved from CNAO1 data samples at 115 MeV/u.

However, since my purpose was the TOF optimization I have decided to investigate whether there were better channels than others. Therefore I have dropped the assumption that the channels response was the same, i.e. $\sigma(T_{bar_1}) \neq \sigma(T_{bar_2})$ and I have studied the single channel time resolutions. I have evaluated the TOF using six possible channels combinations (each experimental setup has four TW readout channels, see sec.5.1):

- CNAO1 data samples: CH 1-2, CH 1-3, CH 1-4, CH 2-3, CH 2-4 and CH 3-4;
- CNAO2 data samples: CH 0-1, CH 0-8, CH 0-9, CH 1-8, CH 1-9 and CH 8-9;
- GSI data samples: CH 0-1, CH 0-2, CH 0-3, CH 1-2, CH 1-3 and CH 2-3.

To determine which of these possible combinations maximize the time resolution I have studied the distributions of the TOF and the arrival times difference measured by each TW channels ($\Delta T = t_j - t_i$). As an example, I report the distributions obtained from the CNAO1 data samples with 115 MeV/u carbon ions beam (see Fig.5.20 and 5.21). The results show that there is a correlation between the TW channels, linked to the geometry and the light attenuation in the bars, which has an appreciable experimental effect.
Considering the CNAO1 data samples, the channels that belong to the same bar are in fact anti-correlated. Due to the attenuation of optical photons in the bar, the collected energy at the two ends of the bar is a function of the ions interaction position: if an incident ion (see Fig.5.22a) hits the first bar at point A, CH 3 will acquire a greater amount of light compared to CH 4.

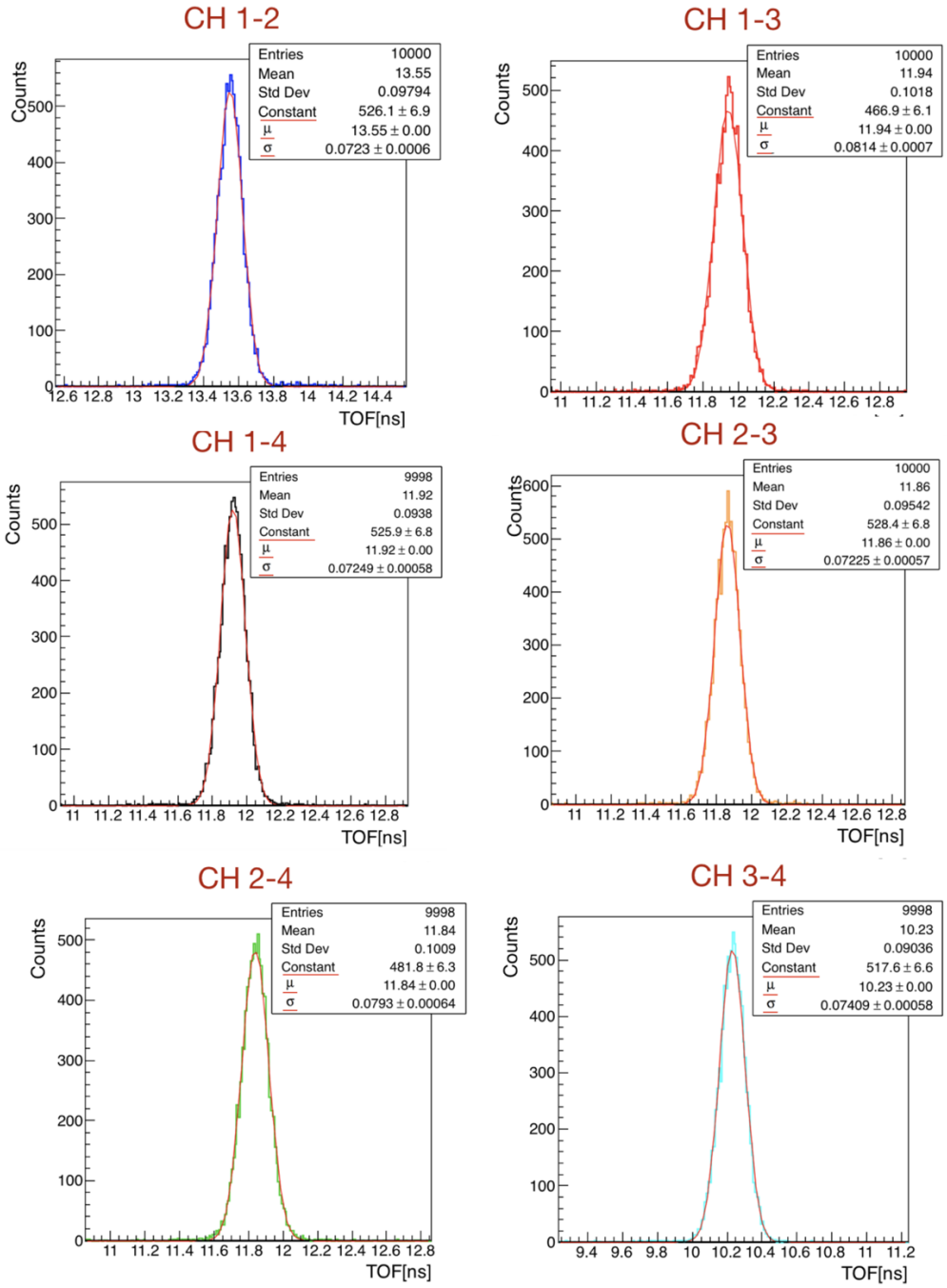


**Figure 5.20.** TOF distribution measured as the difference between the weighted average arrival times of the SC channels and the arithmetic average arrival times of two TW channels. The terms highlighted in red in the box at the top right are the fit parameters. The data are retrieved from the CNAO1 data samples at 115 MeV/u.

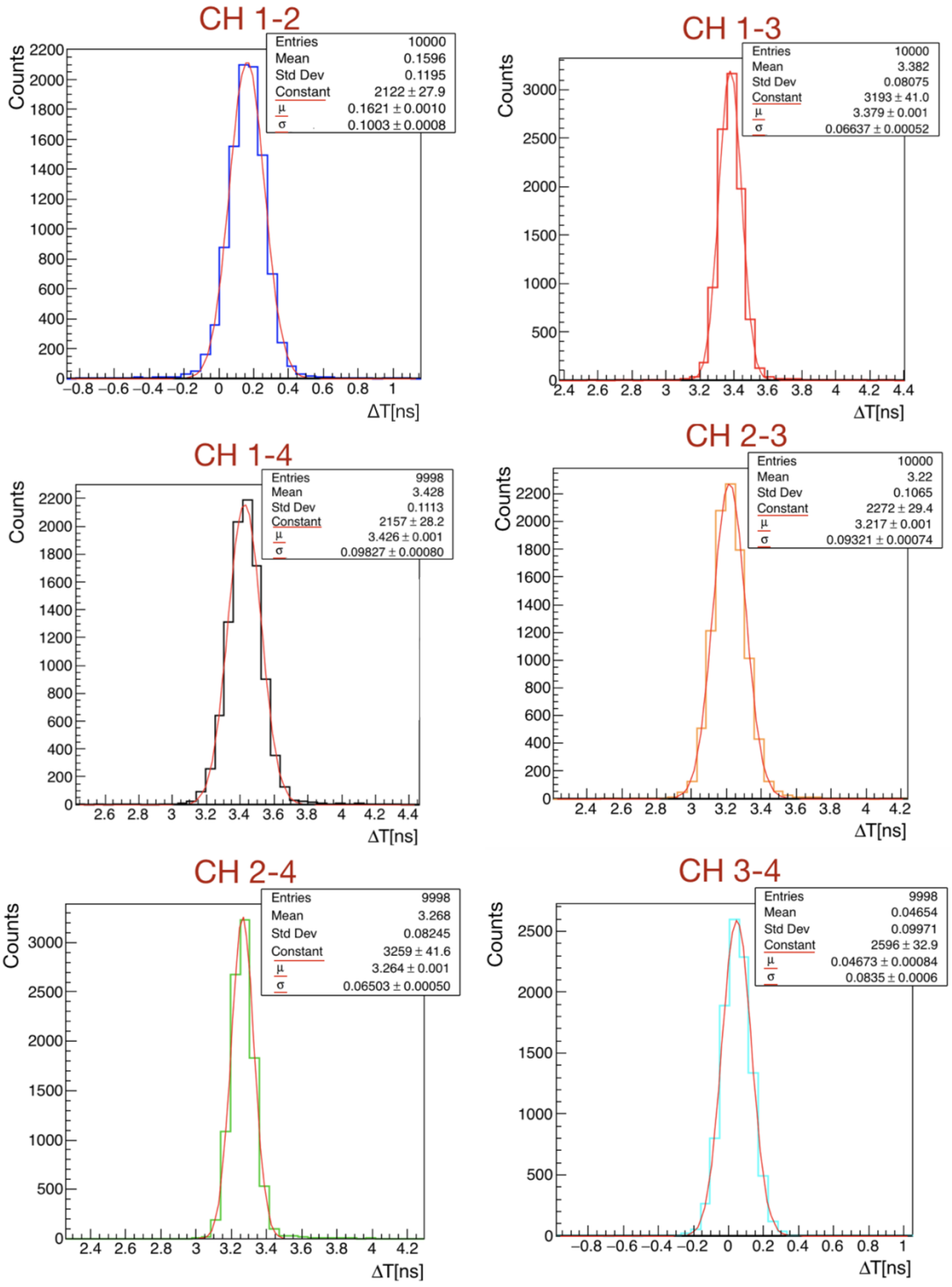


**Figure 5.21.** $\Delta T$ distribution, i.e. the difference between the arrival times measured by the two considered channels. The terms highlighted in red in the box at the top right are the fit parameters. The data are retrieved from the CNAO1 data samples at 115 MeV/u.

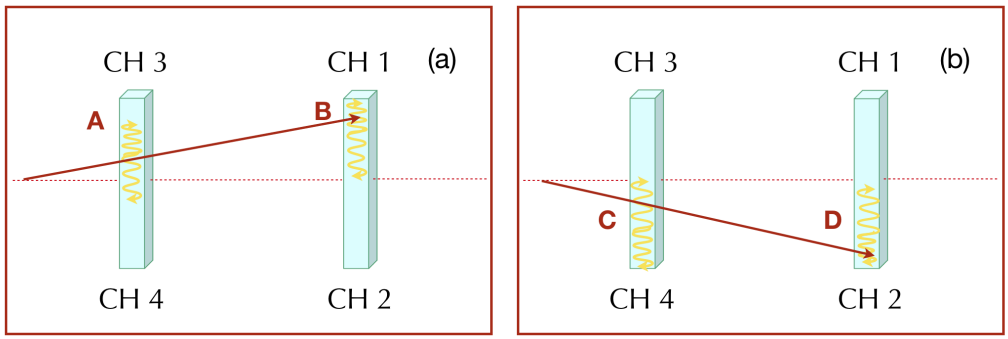


**Figure 5.22.** The arrival time on the TOF wall is evaluated as the average arrival times measured by two channels. Depending on the position in which the particles hit the bars positive or negative correlations between the considered channels, are observed.

We can easily conclude that the two channels that belong to the same bar have a negative correlation. However, considering the very small beam divergence and the negligible impact of the multiple scattering, if the ion hits the first bar at point A, the second bar will be hit approximately at the same height, at point B, thus introducing a geometrical correlation between CH 1 and 3. For this reason the two channels have a positive correlation. The same effect can be observed if the bars are hit at points C and D (see Fig.5.22b). Fig.5.23 shows the possible correlations between the TW channels.

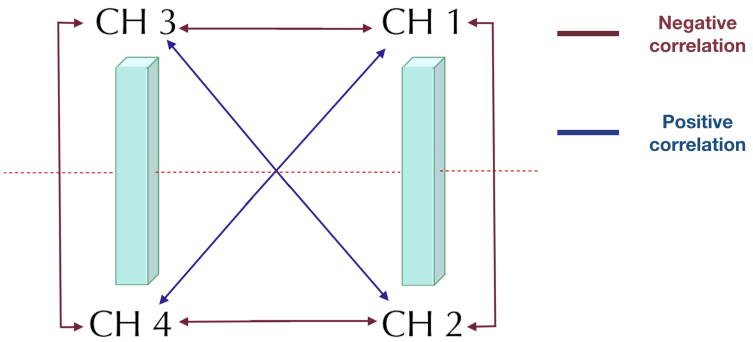


**Figure 5.23.** TW channels correlations for CNAO1 experimental setup.

In fact, if the correlation between the two channels (CH $i$ and $j$) is included, the resolution on the $\Delta t = t_i - t_j$ distribution becomes:

$$\sigma(\Delta t)^2 = \sigma_i^2 + \sigma_j^2 - 2\rho_{ij}\sigma_i\sigma_j \tag{5.17}$$

where $i, j = 1, 2, 3, 4$ and the last term accounts for the positive or negative correlation between CH $i$ and CH $j$. In the same way, also the TW and thus the TOF resolution change. In fact the $\sigma(\overline{T}_{tw})$ which is included in the TOF resolution (see Eq.5.11), becomes:

$$\overline{T}_{tw} = \frac{t_i + t_j}{2} \tag{5.18}$$

$$\sigma(\overline{T}_{tw})^2 = \frac{\sigma_i^2}{4} + \frac{\sigma_j^2}{4} + \frac{\rho_{ij}\sigma_i\sigma_j}{2} \tag{5.19}$$

So, looking at Eqs.5.17 and 5.19, if anti-correlated channels are considered the TW resolution worsens while that of the TOF improves and vice versa. Comparing Figs.5.20 and 5.21 with the equations just reported (Eqs.5.17 and 5.19), it can be concluded that the obtained TOF and $\Delta T$ resolutions for all the different channel combinations are in full agreement with the expected ones when including the contribution from the channels geometrical correlation.
Concerning the other data samples, i.e. CNAO2 and GSI which had the same TW detector and electronic setup, I have observed, as expected, the same TW channels correlation.

Considering these channels and using Eq.5.16 I have obtained for each experimental setup the following TW bar resolutions ($\sigma(\overline{T}_{tw})$):
**CNAO1**

| **Energy [MeV/u]** | $\sigma(\overline{T}_{tw})$ [ps] |
|---|---|
| 115 | $30.7 \pm 0.3$ |
| 151 | $30.7 \pm 0.3$ |
| 221 | $31.6 \pm 0.3$ |
| 280 | $30.8 \pm 0.3$ |

**Table 5.8.** For the CNAO1 experimental setup the first bar has been considered. The table summarizes the TW bar resolutions at 115, 151, 221 and 280 MeV/u obtained using Eq.5.16. The assigned uncertainties are only accounting for the statistical contribution. The TW detector is in saturation condition, the value at 221 MeV/u is due to statistical fluctuations.

**CNAO2**

| **Energy [MeV/u]** | $\sigma(\overline{T}_{tw})$ [ps] |
|---|---|
| 115 | $29.8 \pm 0.4$ |
| 260 | $30.7 \pm 0.4$ |
| 400 | $34.0 \pm 0.4$ |

**Table 5.9.** For the CNAO2 experimental setup the central bar of the first layer has been considered with CH 0-1. The table summarizes the TW bar resolutions at 115, 260 and 400 MeV/u obtained using Eq.5.16. The assigned uncertainties are only accounting for the statistical contribution.

**GSI**

| **Energy [MeV/u]** | $\sigma(\overline{T}_{tw})$ [ps] |
|---|---|
| 400 | $25.3 \pm 0.2$ |

**Table 5.10.** For the GSI experimental setup the central bar of the first layer has been considered with CH 0-1. The table reports the TW bar resolution at 400 MeV/u obtained using Eq.5.16. The assigned uncertainties are only accounting for the statistical contribution.

I have tested that, when comparing the data samples at 400 MeV/u of $^{16}O$ and $^{12}C$ ions, the ratio between the obtained TW time resolutions of oxygen and carbon

beam (0.74) was comparable to the expected one given by (see Eq.2.32):

$$\frac{\sigma(t^o)}{\sigma(t^c)} \sim \frac{Z_c}{Z_o} = 0.75 \tag{5.20}$$

since the time resolution $\sigma(t) \sim 1/\sqrt{\Delta E}$ and from the Bethe-Block equation (see Eq.1.6) it follows that:

$$\Delta E \sim \frac{Z^2}{\beta^2} \sim \frac{Z^2}{E_{kin}} \tag{5.21}$$

where $\Delta E$ is the energy released in the detector.

### 5.3.4 SC resolution

Since the arrival time on the SC has been evaluated accordingly to Eq.5.8, where the $\sigma_i$ values have been extracted from Eq.5.9, the expected SC time resolution can be retrieved from the following equation:

$$\sigma(\overline{T}_{tw-sc})^{ex} = \sqrt{\frac{1}{\sum_i \frac{1}{\sigma_i^2}}} \tag{5.22}$$

where the $\sigma_i$ values are the resolutions obtained from the single TOF distributions ($TOF_i = \overline{T}_{tw} - T_{sc_i}$) measured for each SC channel. Hence, knowing the $\sigma(\overline{T}_{tw})$ from Tabs.5.8 5.9 and 5.10, the expected SC resolution can be retrieved from Eq.5.22 as follows:

$$\sigma(\overline{T}_{sc}^{ex}) = \sqrt{(\sigma(\overline{T}_{tw-sc})^{ex})^2 - \sigma(\overline{T}_{tw})^2} \tag{5.23}$$

Instead, the measured SC time resolutions have been retrieved inverting the Eq.5.11 and using the values of $\sigma(TOF)$ and $\sigma(\overline{T}_{tw})$ just reported in the chapter (see Tabs.5.5 and 5.8 for CNAO1, Tabs.5.6 and 5.9 for CNAO2 and Tabs.5.7 and 5.10 for GSI):

$$\sigma(\overline{T}_{sc}) = \sqrt{\sigma(TOF)^2 - \sigma(\overline{T}_{tw})^2} \tag{5.24}$$

The measured (Eq.5.24) and expected (Eq.5.23) SC resolutions are reported in Tabs.5.11 5.12 5.13 for the three experimental setups:
**CNAO1**

| **Energy [MeV/u]** | $\sigma(\overline{T}_{sc})$ [ps] | $\sigma(\overline{T}_{sc}^{ex})$ [ps] |
|---|---|---|
| 115 | $68.1 \pm 0.7$ | 50.2 |
| 151 | $71.6 \pm 0.7$ | 53.3 |
| 221 | $73.6 \pm 0.7$ | 56.9 |
| 280 | $76.9 \pm 0.8$ | 60.0 |

**Table 5.11.** Measured and expected SC time resolutions obtained from Eqs.5.24 and 5.23 for CNAO1 experimental setup.

**CNAO2**

| **Energy [MeV/u]** | $\sigma(\overline{T}_{sc})$ [ps] | $\sigma(\overline{T}_{sc}^{ex})$ [ps] |
|---|---|---|
| 115 | $70.9 \pm 1.2$ | 50.1 |
| 260 | $83.4 \pm 1.2$ | 58.3 |
| 400 | $86.8 \pm 1.2$ | 61.4 |

**Table 5.12.** Measured and expected SC time resolutions obtained from Eqs.5.24 and 5.23 for CNAO2 experimental setup.

**GSI**

| **Energy [MeV/u]** | $\sigma(\overline{T}_{sc})$ [ps] | $\sigma(\overline{T}_{sc}^{ex})$ [ps] |
|---|---|---|
| 400 | $78.0 \pm 0.7$ | 57.7 |

**Table 5.13.** Measured and expected SC time resolution obtained from Eqs.5.24 and 5.23 for GSI experimental setup

As it can be seen from the results shown in tables 5.11-5.13 for the SC and before for the TW, there is a clear inconsistency between the results obtained with the CNAO1 setup and the CNAO2 one. Furthermore, the time resolution measured for the C and O projectiles does not scale as expected from simple energy deposit considerations. The reasons behind these two different findings are the following: the inconsistency between the setup can be explained by the absence of the trigger cell correction (expected to have a negligible impact, but found to have a significant effect instead) and the exceptional noise measured in the GSI cave (difference between C and O ions). Both effects have been detailed below.

### 5.3.5 Trigger cell correction

Depending on the particle crossing time, a specific trigger cell of the circular buffers is activated. Since the time calibration is not uniform along the buffer (see Fig.5.24), the detector performance depends on the actual event trigger cell (TC). Since the SC channels share the same TC at each event, this effect introduces a natural correlation between them that depends on the trigger cell position in the buffer.

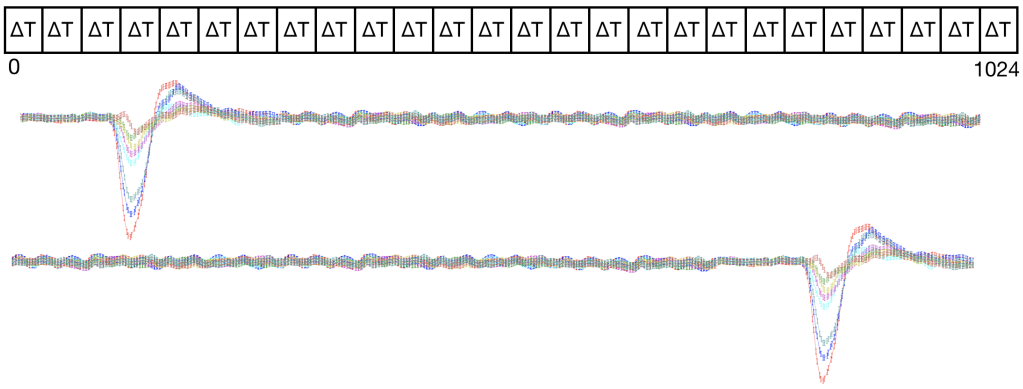


**Figure 5.24.** The buffer of the WaveDAQ system is composed of 1024 trigger cells. The particle transition produces a signal that is acquired by the 8 SC channels. The trigger cell position depends on the particle crossing time and thus it can change event by event. Since it is the same for all SC channels it introduces a correlation that degrades the time resolution.

To analyze this contribution I have studied the TOF measurements as a function of the trigger cell. Fig.5.25 shows the 2D histogram obtained for the CNAO1 data samples with $^{12}C$ ions beam of 115 MeV/u.
Plotting the TOF distribution obtained for the same trigger cell, I have observed that the corresponding mean values have a clear correlation with the trigger cell. To account for such effect I have implemented a correction of the TOF measurements according to the activated trigger cell.

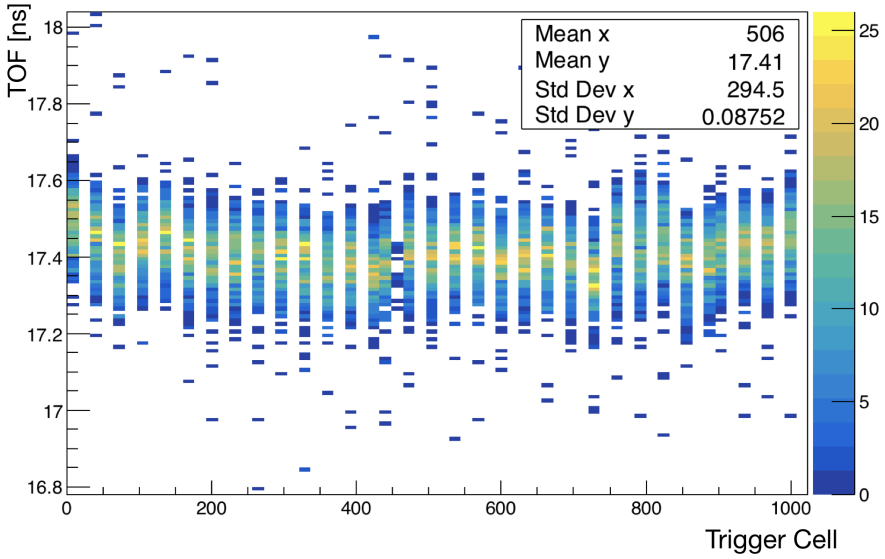


**Figure 5.25.** TOF values as a function of the activated trigger cell in the circular buffer. The data are retrieved from the CNAO1 data samples of $^{12}C$ of 115 MeV/u energy.

To this aim, I have calculated, by setting a reference TC, the correction factors as the difference between the average TOF obtained for a given trigger cell $\overline{TOF}_i$

and the one obtained for a reference trigger cell $\overline{TOF}_r$ :

$$\delta_{TC_i} = \overline{TOF}_r - \overline{TOF}_i \tag{5.25}$$

where $i$ is the index on the trigger cell. Hence, the TOF measurements have been corrected as follows:

$$TOF^f = \overline{T}_{tw} - \overline{T}_{sc} - \delta_{TC_i} \tag{5.26}$$

where $\delta_{TC_i}$ changes event by event depending on the activated trigger cell.
With these $\delta_{TC}$ values I have corrected the TOF and SC resolutions (see Tab.5.14). Figs. 5.26 and 5.27 show the $\sigma(TOF)^f$ and $\sigma(\overline{T}^f_{sc})$ as a function of the beam energy for all the experimental setups.

| | **Energy [MeV/u]** | $\sigma(TOF^f)[ps]$ | $\sigma(\overline{T}^f_{sc})$ [ps] |
|---|---|---|---|
| CNAO1 | 115 MeV/u | $64.2 \pm 0.6$ | $56.3 \pm 0.6$ |
| | 151 MeV/u | $68.3 \pm 0.6$ | $61.1 \pm 0.6$ |
| | 221 MeV/u | $73.9 \pm 0.7$ | $66.8 \pm 0.6$ |
| | 280 MeV/u | $76.1 \pm 0.7$ | $69.5 \pm 0.6$ |
| CNAO2 | 115 MeV/u | $61.5 \pm 0.9$ | $53.8 \pm 0.9$ |
| | 260 MeV/u | $75.1 \pm 1.0$ | $69.2 \pm 0.9$ |
| | 400 MeV/u | $82.5 \pm 1.1$ | $75.2 \pm 0.9$ |
| GSI | 400 MeV/u | $68.5 \pm 0.7$ | $63.7 \pm 0.6$ |

**Table 5.14.** TOF ($\sigma(TOF^f)$) and SC time resolutions ($\sigma(\overline{T}^f_{sc})$) for all experimental setups.

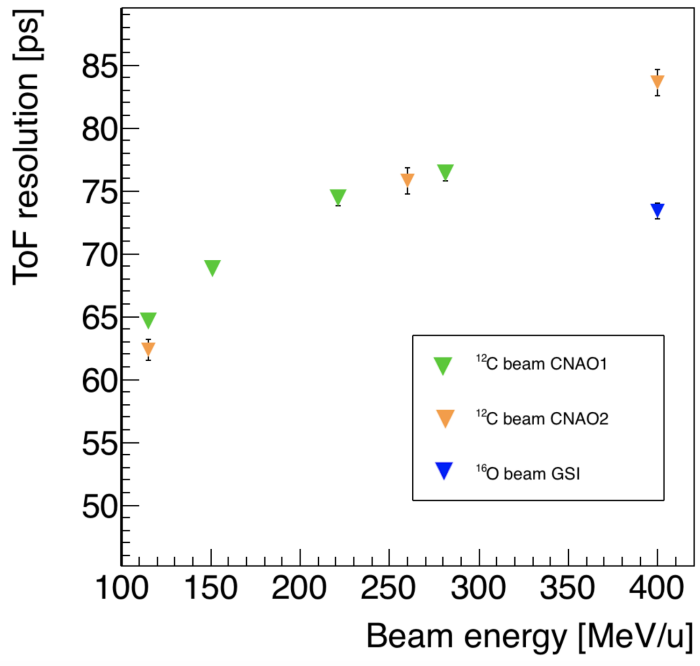


**Figure 5.26.** TOF distribution obtained from Eq.5.26, as a function of the beam energies of the three experimental setups. The green, orange and blu points represent the value obtained from the CNAO1, CNAO2 and GSI data analysis respectively.

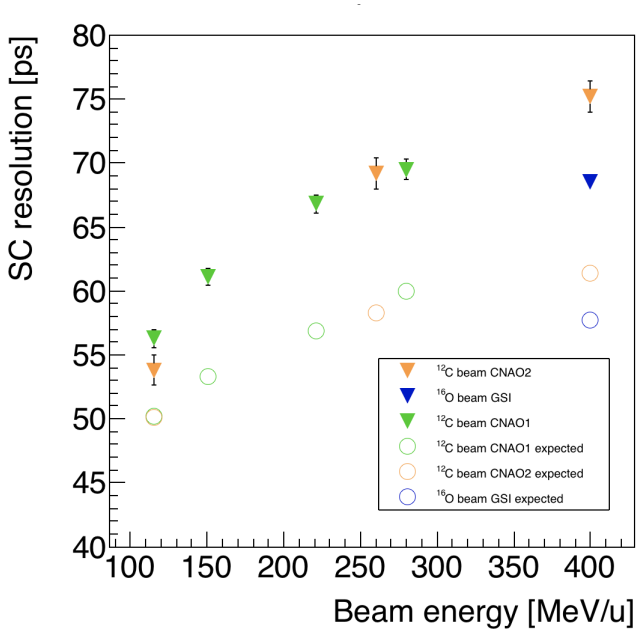


**Figure 5.27.** SC resolutions as a function of the beam energy. The green, orange and blu points represent the value obtained from the CNAO1, CNAO2 and GSI data analysis respectively. The circles points represent the expected SC resolutions $\sigma(\overline{T}_{sc}^{ex})$ reported in Tabs.5.11,5.12 and 5.13.

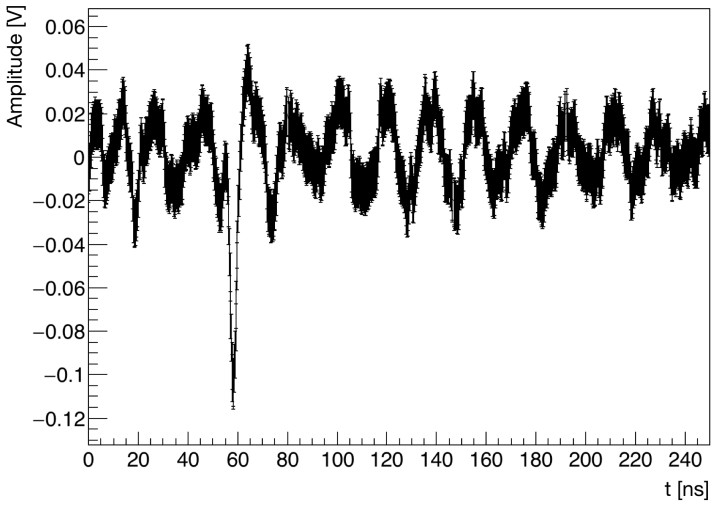


**Figure 5.28.** SC signal produced by the interaction of incoming oxygen ion of 400 MeV/u energy and acquired by CH 8.

Even if the trigger cell correction has improved significantly the time resolution, the expected and measured $\sigma$ values still differ. This is probably due to the a low optical coupling efficiency between the SiPMs and the scintillator detectors and to the SC and TW channels correlation.
As can be seen, the SC time resolutions follows the expected behavior (see Eq.2.32):

$$\frac{\sigma(t)}{t} \sim \sqrt{E_{kin}} \tag{5.27}$$

Considering the data samples at 400 MeV/u of $^{12}C$ and $^{16}O$ ion beams, I have verified, through MC simulation, that the energy loss in the SC by the carbon ion is $(6/8)^2$ times the one of the oxygen ion (Beth-Block, see Eq.1.6). However, I have observed that the ratio between the obtained SC time resolutions (0.84) of oxygen and carbon beam differs from the expected one (see Eq.5.20). This discrepancy suggests that there's a systematic effect that has to be accounted for when comparing the results obtained using the carbon and oxygen data samples. In fact concerning the GSI data samples we observed a relevant noise superimposed to the signals (see Fig.5.28) in $\sim 3-4\%$ of the events which can have contributed significantly to the time resolution worsening.

# Conclusions and perspectives

This thesis reports the study that I have carried out, of the time of flight detectors which are being used within the FOOT experiment. FOOT is an applied nuclear physics experiment that aims to measure the nuclear fragmentation cross-sections which are relevant for PT and RPS applications. These measurements are crucial to improve the description and benchmark the nuclear interaction models used to calculate the dose maps in treatment planning and in radiation shielding studies. The FOOT experiment has been designed to identify the fragments produced in inelastic interactions in thin detectors. To this aim, it measures the particles Time of Flight, energy loss and bending in magnetic field, thus allowing to evaluate their velocity, energy and momentum. These measurements can be then combined in different ways to perform the fragments isotopic identification with a high accuracy. At the energy range of interest for PT and RPS applications explored by the FOOT collaboration, it is essential to maximize the time resolution since the measurements of the bending and energy loss have a resolution that is limited by the experiment dimension (table-top) and affordable magnetic field. Therefore a crucial role in minimizing the uncertainty on the fragments isotope mass number determination is played by the particles Time Of Flight measurements.
This thesis describes in detail the analysis work I have done to evaluate the TOF detectors performance and overall resolution. The data analyzed have been acquired using $^{12}C$ and $^{16}O$ ion beams of different kinetic energies, that were impinging on the start counter and the scintillator wall. The SC and TW detector performance were studied in detail for the first time in the FOOT experiment context, and the expected time resolution was obtained for both detectors and compared with the expectation values. In order to achieve the required resolution on the mass number $\sigma(A)$, the overall TOF resolution needs to be $< 100$ ns. In order to evaluate the best time resolution achievable in FOOT, I had to take into account the time jitter ($\sim$ few ns) between the detectors and the SC and TW channels correlation. The obtained results are really promising even if the SC time resolution is worse with respect of the expected one of about $\sim 10$ ps, probably due to the low optical coupling efficiency between the SiPMs and the scintillator detectors.
This thesis work proved that a careful check of the detector implementation is needed in order to match the required time resolution and triggered also additional simulation and R&D studies that will explore other solutions of the SC detector implementation.
For what concerns the TW detector, these preliminary studies have actually proven that the expectations are met in the energy range of interest for FOOT, allowing to achieve the required time resolution. The analysis algorithm that I have developed

are currently used within the collaboration to analyze the waveforms collected in the different detector tests and are the basis of the data analysis that will happen in 2020 using the full electronic setup to perform double differential cross section measurements.

# Bibliography


[1] Daniel Cussol. *Nuclear Physics and Hadrontherapy.* LPC Caen, ENSICAEN, Université de Caen Basee-Normanide, IN2P3/CNRS, 2000.

[2] J. P. Biersack J. F. Ziegler and M. D. Ziegler. Srim—the stopping and range of ions in matter (srim, chester, md). *http://www.srim.org/*, 2008.

[3] P.V. Vavilov. Ionizational losses of high energy heavy particles. *Zh. Eksp. Teor. Fiz.*, 32:920–923, 1957.

[4] Thilo Elsässer Dieter Schardt and Daniela Schulz-Ertner. Heavy-ion tumor therapy: Physical and radiobiological benefits. *Rev. Mod. Phys*, 82(383), 2010.

[5] Serber R. Nuclear reactions at high energies. *Phys. Rev.*, 72:1114–1115, 1947.

[6] C. Perrin J. Arvieux R. Bertholet J. F. Bruandet M. Buenerd R. Cherkaoui A. J. Cole Y. El-Masri N. Longequeue J. Menet F. Merchez S. Kox, A. Gamp and J. B. Viano. Trends of total reaction cross sections for heavy ion collisions in the intermediate energy range. *Phys. Rev. C.*, 25:1678–1691, 1987.

[7] H. Iwase E. Haettner and D. Schardt. Experimental fragmentation studies with 12-c therapy beams. *Radiat. Prot. Dosis*, 122:485–487, 2006.

[8] Durante M. Tommasino F. Proton radiobiology. *Cancers*, 7:353–381, 2015.

[9] Weyrather W.K. Medical applications of accelerated ions. *Lecture Notes in Physics*, 651:469–490, 2004.

[10] Kraft G. Tumor therapy with heavy charged particles. *Progress in Particle and Nuclear Physics*, 45:473–544, 2000.

[11] Belli et al. (1998) and Furusawa et al. (2000). *Scholz.* 2003.

[12] Thilo Elsässer Dieter Schardt and Daniela Schulz-Ertner. Heavy-ion tumor therapy: Physical and radiobiological benefits. *Rev. Mod. Phys*, 82(383), 2010.

[13] Scholz M. Weyrather W.K., Ritter S. and Kraft G. Rbe for carbon track-segment irradiation in celllines of differing repair capacity. *International Journal of Radiation Biology*, 75:1357–1364, 1999.

[14] R.; Wilson J.W.; Townsend L.W.; Shinn J.; Hajnal F. Cucinotta, F.A.; Katz. Biological effectiveness of high-energy protons: Target fragmentation. *Radiat. Res.*, 127:130–137, 1991.

[15] Paganetti H. Relative biological effectiveness (rbe) values for proton beam therapy. variations as a function of biological endpoint, dose, and linear energy transfer. *Phys. Med. Biol.*, 59:419–472, 2014.

[16] Kramer M. Zink K. Durante M. Engenhart-Cabillic R. Scholz M. Grun R., Friedrich T. Biologically effective proton range analysis. *Med. Phys.*, 40:1–10, 2013.

[17] Braunn B. et al. Assessment of nuclear-reaction codes for proton-induced reactions on light nuclei below 250 mev. *Eur. Phys. J. Plus*, 130(7), 2015.

[18] Exfor website : https:// www-nds.iaea.org/exfor/exfor.htm.

[19] Iljinov A. et al. Production of radionuclides at intermediate energies. *LandoltBònstein, New Series, Subvol. I/13*, 1991.

[20] Koning A. J. et al. Talys-1.0. *International Conference on Nuclear Data for Science and Technology. EDP Sciences*, page 211–214, 2007.

[21] ICRU. Nuclear data for neutron and proton radiotherapy and for radiation protection. *Radiation Research*, 2001.

[22] Boudard A. et al. New potentialities of the liege intranuclear cascade model for reactions induced by nucleons and light charged particles. *Phys. Rev.*, C 87(1), 2013.

[23] Kelic A. et al. Abla07-towards a complete description of the decay channels of a nuclear system from spontaneous fission to multifragmentation. *arXiv preprint: 0906.4193*, 2009.

[24] Gunzert-Marx K. et al. Secondary beam fragments produced by 200 mev/u 12-c ions in water and their dose contributions in carbon ion radiotherapy. *New J. Phys.*, 10(7), 2008.

[25] Dudouet J. et al. Double-differential fragmentation cross-sections measurements of 95 mev/u 12-c beams on thin targets for hadrontherapy. *Phys. Rev. C.*, 88(2), 2013.

[26] Toppi M. et al. Measurements of 12-c ion fragmentation on thin carbon target from the first collaboration at gsi. *Journal of Physics: Conference Series*, 590, 2015.

[27] Marafini M. et al. Secondary radiation measurements for particle therapy applications: nuclear fragmentation produced by 4-he ion beams in a pmma target. *Phys. Med. Biol.*, 62(4), 2017.

[28] *FOOT Conceptual Designed Report.*

[29] Dudouet J. et al. Double-differential fragmentation cross-section measurements of 95 mev/nucleon 12-c beams on thin targets for hadron therapy. *Physical Review*, 88, 2013.

[30] Rescigno R. et al. Performance of the reconstruction algorithms of the first experiment pixel sensors vertex detector. *Nuclear Instruments and Methods in Physics Research*, A767:34–40, 2014.

[31] Abou-Haidar Z. et al. Performance of upstream interaction region detectors for the first experiment at gsi. *Journal of Instrumentation*, 7, 2012.

[32] Paoloni A. et al. The upstream detectors of the first experiment at gsi. *Physics Proc.*, 37:1466–1472, 2012.

[33] Anelli M. et al. First experiment upstream detectors performance on gsi 400 mev/u 12c beam. *Nuclear Science Symposium and Medical Imaging Conference*, IEEE:2800–2804, 2011.

[34] Plume website: www.iphc.cnrs.fr/plume.html.

[35] De Lellis G. et al. Nuclear emulsions. *CW Fabjan and H Schopper, Elementary Particles: Detectors for Particles and Radiation*, 21B Springer, 2011.

[36] De Lellis G. et al. Emulsion cloud chamber technique to measure the fragmentation of a high-energy carbon beam. *J Instrum,*, 2(06), 2007.

[37] Gianotti F. Fabjan C. Calorimetry for particle physics. *CERN-EP*, 75, 2003.

[38] Schluterb T. Rauch J. Genfit a generic track-fitting toolkit. *Journal of Physics*, 608, 2015.

[39] Fassò A. Ranft J. Ferrari A., Sala P. Fluka: a multi-particle transport code. *Technical Report CERN-2005-10*, 2005. INFN/TC 05/11, SLAC-R-773, CERN, INFN, SLAC.

[40] M.P.W. Chin A. Fassò A. Ferrari P.G. Ortega A. Mairani P.R. Sala G. Smirnov T.T. Bohlen, F. Cerutti and V. Vlachoudis. The fluka code: Developments and challenges for high energy and medical applications. *Nuclear Data Sheets*, 120:211–214, 2014.

[41] Battistoni G., Böhlen T. T., Cerutti F., Chin P. W., Esposito L. S., Fassò A., Ferrari A., Lechner A., Empl A., Mairani A., Mereghetti A., Ortega P. G., Ranft J., Roesler S., Sala P. R., Vlachoudis V., and Smirnov G. Overview of the fluka code. *Annals of Nuclear Energy*, 82(10), 2015.

[42] T. Schluterb. J. Rauch. Genfit a generic track-fitting toolkit. *Journal of Physics*, 608, 2015.

[43] Brun R. and et al. Root an object oriented data analysis framework. *Nuclear Instruments and Methods in Physics Research Section A: Accelerators, Spectrometers, Detectors and Associated Equipment*, 389:81–86, 1996.

[44] Matthiae G. Glauber R. J. High-energy scattering of protons by nuclei. *Nucl. Phys*, B12(135), 1970.

[45] Gribov V.N. Glauber corrections and the interaction between high- energy hadrons and nuclei. *Sov. Phys JETP 29 N.3*, 483, 1969.

[46] Toppi M. and et al. Measurements of fragmentation cross section of c-12 ions on a thin gold target with the first apparatus. *Phys. Rev.*, C93, 2016.

[47] Kraan A. C. Range verification methods in particle therapy: underlying physics and monte carlo modeling. *Frontiers in Oncology*, 5(150), 2015.

[48] Aichelin J. Quantum molecular dynamics. a dynamical microscopic n-body approach to investigate fragment formation and the nuclear equation of state in heavy ion collisions. *Phys. Rep.*, 202(62, pages =).

[49] Gupta S.D. Bertsch G. A guide to microscopic models for intermedia- te energy heavy ion collisions. *Phys. Rep.*, 160(4):189–233, 1988.

[50] Gadioli E. and et al. Boltzmann master equation theory of angular di- stributions in heavy-ion reactions. *Nuclear Physics*, A643, 1998.

[51] Triparthi R. and et al. Accurate universal parameterization of absorption cross sections. *Nuclear Instruments and Methods in Physics Research*, B117:347–349, 1996.

[52] Triparthi R. and et al. Accurate universal parameterization of absorption cross sections ii - neutron absorption cross sections. *Nuclear Instruments and Methods in Physics Research*, B-129:11–15, 1997.

[53] Triparthi R. and et al. Accurate universal parameterization of absorption cross sections iii - neutron absorption cross sections. *Nuclear Instruments and Methods in Physics Research*, B55:349– 356, 1999.

[54] Glenn F. Knoll. *Radiation Detection and Measurement 3rd edition.* New York, 2000.

[55] C. Bemporad et al. A. Baldini, E. Baracchini. The design of the meg ii experiment. *Eur. Phys. J. C*, 78:230, 2018.

[56] S. Ritt. The drs chip: Cheap waveform digitizing in the ghz range. *Nucl. Instrum. Methods Phys. Res.*, A518:2470–471.

[57] Marco Francesconi. The meg II trigger and data acquisition system. *Univerisity of Pisa*, 2016.